Abstract

Title of dissertation: Motion of Elastic Capsules in Microfluidic Channels

Shugi Kuriakose
Doctor of Philosophy, 2010
Department of Chemical and Biomolecular Engineering

Dissertation directed by: Panagiotis Dimitrakopoulos, Ph.D.
Department of Chemical and Biomolecular Engineering

Capsule flow dynamics in microchannels plays a significant role in complex biological phenomena, such as the microcirculation, and in engineering applications, such as in microfluidic devices for drug delivery and cell sorting. In this thesis, we investigate the motion of elastic capsules in wall-bounded flows by extending the Membrane Spectral Boundary Element method developed by Dodson and Dimitrakopoulos [16] for free-suspended flows.

First, a validation study of the method is performed for the axisymmetric capsule motion in a cylindrical channel. For a capsule moving along the centerline of a cylindrical channel, our computational model successfully reproduced the parachute shape observed in earlier experimental and computational studies. Next, we investigate the flow dynamics of a strain-hardening Skalak capsule moving along the centerline in a square and a rectangular channel. We examine how the capillary number and capsule size influence the deformation and physical properties of the capsule. For large capsules in a square channel, our investigation reveals that the steady-state capsule shape is non-axisymmetric. The capsule assumes a shape similar to the channel's cross-section i.e. a square shape with rounded edges. Buckling

of the capsule's upstream end resulting in a negative edge curvature is observed at higher capillary numbers and for large capsule sizes. For the largest capsules studied, we also observe the development of dimples at the capsule's lateral surface. A comparative study of capsule motion and deformation in cylindrical and square channels shows that the capsule deformation in a cylindrical channel is similar to that in a square channel at a larger capillary number. In a rectangular channel, we observe a three-dimensional (i.e. non-axisymmetric) deformation of the capsule at high capillary numbers resulting in dimpling of the capsule's upstream end at steady state. We also consider the transient motion of a capsule in a converging square microchannel and investigate the influence of viscosity ratio, capillary number and capsule size on the evolution of capsule properties. As the capsule moves through the converging region a fluctuation in the geometric and physical properties of the capsule is observed.

In addition, we investigate the hemodynamic forces on endothelial cells and leukocytes in blood capillaries. Our study on hemodynamic forces demonstrates that the forces on endothelial cells increase in the presence of leukocytes in close vicinity. Both normal and shear forces show considerable increase. We also investigate the forces on moving leukocytes in the presence of adherent leukocytes. With increasing cell size, the magnitude of the force increases till a threshold value of the cell size and then decreases.

Motion of Elastic Capsules in Microfluidic Channels

by

Shugi Kuriakose

Dissertation submitted to the Faculty of the Graduate School of the
University of Maryland, College Park in partial fulfillment
of the requirements for the degree of
Doctor of Philosophy
2010

Advisory Committee:

Professor Panagiotis Dimitrakopoulos, Chair/Advisor
Professor Raymond A. Adomaitis
Professor Elias Balaras
Professor Richard V. Calabrese
Professor Srinivasa R. Raghavan

Acknowledgements

I would like to thank my advisor, Professor Panagiotis Dimitrakopoulos for his support and guidance throughout my graduate studies. His expertise and directions made this work successful. I must also thank former and current students in our research group, including Walter Dodson, Moon Soo Lee, Kishore Mamidi and Sun Young Park. Special acknowledgement is due to Dr. Walter Dodson for developing, in conjunction with Professor Dimitrakopoulos, the numerical method for capsule dynamics. I would also like to thank my examining committee members, including Professors Adomaitis, Balaras, Calabrese and Raghavan. Further, I must acknowledge the Department of Chemical and Biomolecular Engineering at the University of Maryland, College Park.

I would like to thank my husband for his love and support during my graduate studies. Special thanks are also due to my son and daughter for being well-behaved and letting me work. I would also like to acknowledge the help and support of my extended family including my parents and in-laws, brother, brother-in-law and sisters-in-law.

Last but not the least, I must acknowledge God Almighty, "for of Him, and through Him and to Him are all things: to whom be glory forever."

This research was supported in part by the National Science Foundation and the National Center for Supercomputing Applications in Illinois.

Table of Contents

List of Figures

List of Abbreviations

α_p	Prestress parameter [22]
$\Delta \boldsymbol{f}$	Surface stress vector [21]
Δt	Time step [27]
λ	Viscosity ratio [19]
λ_α	Stretch ratios [22]
μ	Ambient viscosity [16]
$\boldsymbol{\sigma}$	Stress tensor [16]
τ_α^P	Principal tensions [21]
$\boldsymbol{\tau}$	In-plane stress resultant [21]
a	Capsule radius [19]
C	Moduli ratio [22]
Ca	Elastic capillary number [25]
G_s	Shear modulus [25]
h	Minimum distance between capsule surface and walls [43]
K	Area dilitation modulus [22]
l_y	Half-length of channel cross-section [19]
L_x	Capsule length [23]
L_y	Capsule width [23]
L_z	Capsule height [23]
$\boldsymbol{n}$	Surface normal vector [16]
N_B	Number of basis points [31]
N_E	Number of spectral elements [31]
p	Pressure [15]
Re	Reynolds number [15]
$\boldsymbol{S}$	Stokeslet solution for velocity [16]
$\boldsymbol{T}$	Stokeslet solution for stress [16]
$\boldsymbol{u}$	Velocity [16]
$\boldsymbol{u}^\infty$	Undisturbed velocity [20]
U	Average undisturbed velocity [21]
$\boldsymbol{x}$	Geometry [16]

*[#]: Page number in which the quantity is defined or first encountered.

Chapter 1

Introduction

The current thesis investigates the motion and deformation of capsules in microchannels and microvessels which is representative of the flow in microfluidics and the microcirculation. To do this we use the spectral boundary element method for membranes [16]. Membrane-bound fluid volumes found naturally in biological systems as well as artificially created for industrial applications can be broadly categorized as "capsules". Examples include the red blood cells and various liquid globules encountered in food, cosmetics and other industrial products. Capsules differ from droplets in having a material interface which exhibit mechanical properties that are more complex than that described by a surface tension [45]. In this chapter, we present a brief review of capsules in microfluidics and microcirculation. We also review previous experimental and computational studies on capsule dynamics in wall-bounded flow. Lastly, the outline of the thesis is presented.

1.1 Capsules in Microfluidics and the Microcirculation

The study of capsules in microchannels is of great interest because of their applications in microfluidics and the microcirculation. Recent technological advances

in the field of microfluidics has resulted in the development of efficient fabrication techniques for microcapsules as well as novel analytical and industrial applications in diverse fields such as medicine, cosmetics, food design and coating of textiles. Capsules are used for encapsulation, release and protection of agents such as medicine, fragrances, dyes and flavor additives [45].

The capsule flow dynamics has a crucial role in the efficient functioning of capsule-based devices as well as the fabrication of capsules using microfluidic devices. Microfluidic technology enables the fabrication of large quantities of uniform-sized capsules with customizable morphologies and physicochemical properties [25]. Such capsules can be used as containers for the storage and controlled release of loaded molecules in drug delivery applications. The ultimate goal for drug delivery application is to develop intelligent capsule systems containing medical agents that recognize and adhere to the infected regions in the body and allow targeted localized release of medical agents, and thus limiting side effects [19]. Another application where microcapsules are being increasingly used is in microreactors. Droplet-based microreactors are being used for studying enzyme kinetics, enzyme assay and DNA analysis, protein crystallization, synthesis of molecules, nanoparticles, microparticles and colloidal assemblies [60]. Microreactors have many advantages over conventional reactors. They facilitate faster, less expensive reactions with parallelization capabilities because of the encapsulation. Mixing in microreactors is achieved by internal circulation caused by the channel geometry [59].

The predominant microfluidic systems used for microcapsule generation are T-junctions, cross-junctions and flow-focusing nozzles. These systems can be used

for generating microcapsules with many functionalities. Seiffert *et al.* [55] used a double-cross junction to fabricate functional microgel capsules that consist of two miscible, yet distinct layers. Lensen *et al.* [35] prepared biodegradable PLLA (Poly L-Lactic Acid) capsules using a flow-focusing nozzle. They prepared both hollow and solid capsules which are suitable for drug delivery of hydrophobic compounds. Hwang, Dendukuri and Doyle [25] synthesized magnetic hydrogel particles using a T-junction. They made use of the channel geometry to synthesize particles with diverse shapes. They created spherical, disk-shaped and plug-shaped particles by modifying the geometry of the confining microchannels. Thus the channel geometry plays an important role in the determination of the characteristics of the microcapsule.

The human red blood cell is a very common example of capsule in nature. It consists of a small mass of protoplasm bounded by the plasma membrane. In microcirculation the motion of red blood cells through vascular microvessels has long been recognized as a fundamental problem in physiology and biomechanics, since the main function of these cells, to exchange oxygen and carbon dioxide with the tissues, occurs in capillaries [82]. Numerous studies have focused on the flow and deformation behavior of the red blood cells (RBCs). An understanding of the deformation and flow characteristics of erythrocytes is important for better understanding of the blood circulation. The mechanical properties of red blood cells, which allow them to undergo large deformation and reversible aggregation, play a major role in blood flow. The erythrocyte membrane has a very low bending resistance but it shows resistance against shearing. The red blood cells attain several equilibrium shapes during microcirculation and these shapes are determined by the

dimensions of the blood capillaries. The parachute or umbrella shape is the most common shape attained by the cells in blood capillaries [56]. Various disease states like malaria and sickle cell anemia result in changes in the deformability of these cells [10]. The effect of such diseases can be elucidated by studying the flow characteristics of red blood cells.

The mutual interactions between red blood cells and other blood components such as leukocytes are important for many biological processes like the margination of white blood cells during the immune response. Margination is the process in which free flowing leukocytes move towards the walls of the blood vessels and undergo interactions with endothelial cells on the vessel wall. The role of hydrodynamic forces on such processes has been the subject of recent studies [21, 58, 63, 62]. In the past few years there has been a lot of interest in the development of lab-on-a-chip devices for diagnostic purposes owing to their many advantages, such as cost effectiveness and portability, over conventional devices. Hydrodynamics has been used as the basis of separation in cell-sorting devices (e.g. a cell sorting device based on lateral drift developed by Chabert *et al.* [7]). The study of capsule dynamics in microfluidic channels, which is the subject of this dissertation, is hence essential to understand various physiological processes in microcirculation and to design and operate new microfluidic devices for applications such as cell sorting, capsule fabrication and sorting, and microreactors.

1.2 Capsule Dynamics in Wall-Bounded Flow

The dynamics of both capsules and droplets has been studied rather extensively in the past decades for unbounded flow conditions [30, 32, 62, 16, 15]. Unbounded flow conditions are applicable only when the capsule size is much smaller than the channel dimensions. In microcirculation and microfluidics, this is not always true and hence study of wall bounded flow dynamics is essential to obtain a clear picture of the physical situation. There have been very few studies of wall-bounded flow of capsules and most of these were carried out in cylindrical tubes or parallel plate geometry where axisymmetry and two-dimensionality simplifies the problem.

1.2.1 Capsule Dynamics in Cylindrical Channels

Numerous studies have been conducted to investigate the motion and deformation of drops in cylindrical channels. Hodges, Jensen and Rallison [23] studied the motion of a viscous drop through a cylindrical tube and investigated the effect of viscosity on film thickness. Lac and Sherwood [31] studied the drop deformation in a capillary and considered the effects of size, viscosity and capillary number. They found that the droplet elongates with increasing capillary number and ultimately dimples in the rear. They also found that low viscosity droplet is less deformed than a high viscosity one and decreasing the viscosity results in the disappearance of the dimple. Martinez and Udell [39] considered the axisymmetric creeping motion through circular tubes and studied the effects of capillary number, drop size and

viscosity ratio. They found that droplets smaller than $a/R = 0.7$ are insensitive to changes in capillary number lesser than $Ca = 0.25$ and viscosity ratio.

The above-mentioned studies for droplets are valid for capsules only when the viscosity ratio $\lambda \ll 1$. Recent developments in the field of targeted drug delivery, microreactor-based technologies, etc. have generated interest in the study of capsule motion and deformation in microchannels. Capsule motion in cylindrical channels has been studied experimentally as well as numerically. Risso, Collè-Paillot and Zagzoule [51] studied experimentally the motion and deformation of a capsule in a tube. They used capsules designed for medical use consisting of calcium-alginate gel beads coated with human serum albumin (HSA) whose gel core was reliquified. They concluded that the steady-state attained by the capsule depends on the capillary number and the ratio of the capsule and tube radius. They found that the steady state reached by the capsule depends on capillary number and ratio of the size of capsule to that of the radius of the tube. At fixed a/R the capsule is stretched in the axial direction when Ca is increased. They also found that as Ca is increased the curvature of the rear decreases and at large Ca the rear buckles inward.

Ma and coworkers [38] combined a finite volume method with a front tracking method to study the initial motion of a two-dimensional capsule in a microchannel flow. They studied the lift velocity of circular, elliptical and biconcave capsules. Leyrat-Maurin, Drochon and Barthès-Biesel [36, 37] studied the motion of a capsule through a constriction smaller than its initial dimensions by employing an axisymmetric model. Queguiner and Barthès-Biesel [49] used a boundary integral method to study the flow of capsules into pores. The pore was modeled as a cylinder with hy-

perbolic entrance and exit regions and the capsule was modeled as having discoidal unstressed shape. They studied the effect of capsule size, geometry, and membrane properties on the flow and found that the tube length necessary to reach steady conditions depends strongly on capsule size and membrane behavior. Lefebvre and Barthès-Biesel [33] investigated the effect of membrane prestress and constitutive law on steady-state and found that for a given size ratio the critical flow rate at which the back curvature changes is strongly dependent on pre-inflation. The steady-state shapes obtained by the abovementioned study and experimental study conducted by Risso *et al.* [51] were found to be significantly different. They concluded that pre-inflation resulted in the difference between the experimental and numerical shapes.

Microfluidics is a useful tool for modeling microcirculation in order to obtain a better understanding of the various processes and also to investigate the effects of diseases. Also, devices based on microchannels are being developed for diagnostic purposes in order to sort and characterize blood cells. This has motivated many investigations of the flow of blood cells in microchannels. Skalak and Branemark's pioneering study [56] revealed the interesting shapes of red blood cells in capillaries. They found that the parachute or umbrella shape often observed is not an axisymmetric shape as formerly assumed but is the basic biconcave disc shape of the red cell with the upstream end flattened by the pressure gradient. Antia and coworkers [3] developed a microfluidic device to model the cell-cell interactions in malaria pathogenesis under physiological flow conditions. To mimic the blood flow, they used microfluidic channels of a variety of shapes and sizes, including straight 50 μm channel, channels with narrow 4 μm constrictions and bifurcating channel

that resembled a network of capillaries. Faivre and coworkers [18] used a microfluidic constriction for separation of red blood cell from the suspending plasma. They observed that the presence of an obstruction in a channel results in enhanced cell free layer downstream the obstruction. This principle was utilized to design a device for separation of blood from plasma. Korin, Bransky and Dinnar [27] studied the motion and deformation of red blood cells flowing in a microcrochannel using a theoretical model and a novel automated rheoscope. The model was utilized to evaluate the effect of different biophysical parameters, such as: inner cell viscosity, membrane shear modulus and surface to volume ratio on deformation measurements. They found that changes in inner cell viscosity and ambient fluid viscosity have a minor effect on the deformation. However, the shear modulus has a major effect on the asymptotic maximum cell deformation index.

There have been numerous studies of red blood cell flow dynamics in microvessels. Barber and coworkers [5] used a two-dimensional flexible particle model to study the movement, deformation and partitioning of red blood cells in diverging microvessel bifurcations. Chung, Johnson and Popel [8] developed a computational scheme which used a chimera grid method for simulation of three-dimensional motion and aggregation of red blood cells in a narrow tube. Zhang, Johnson and Popel [69] developed a two-dimensional numerical model for deformable capsules in flows. They used an immersed boundary lattice Boltzmann method. They investigated the flow of cells in small channels to mimic blood cells in capillaries. They observed parachute shape formation for cell to tube diameter ratios greater than 1. They also found that at steady state the cells exhibit similar shapes irrespective of the

initial orientation of the cell. Pivkin and Karniadakis [43] developed a coarse grain procedure for modeling red blood cells using arguments based on mean-field theory. They used this model in dissipative particle dynamics simulation of RBCs in capillary flows. They observed a transition to parachute shape from the biconcave shape. Noguchi and Gompper [41] studied the dynamics of fluid vesicles and cells in cylindrical capillary flow by using a three-dimensional mesoscopic simulation approach. As the flow velocity increases, a model RBC is found to transit from a non-axisymmetric parachute shape (coaxial with the flow axis), while a fluid vesicle is found to transit from a discocyte to a prolate ellipsoid. Pozrikidis [47] developed a theoretical model based on the boundary integral method for describing the motion of a deformable cell. He investigated cells with spherical, oblate ellipsoidal, and biconcave unstressed shapes enclosed by membranes that obey a neo-Hookean constitutive equation. He found that the spherical cells migrate toward the tube centerline while oblate and biconcave cells develop parachute and slipper-like shapes, respectively. Pozrikidis [46] also investigated the axisymmetric motion of a file of red blood cells through capillaries. These studies showed that the capillary radius and cell spacing are significant in determination of discharge hematocrit and apparent viscosity of the one-dimensional suspension. Zhao and coworkers [66] developed a spectral boundary integral method for simulating large number of blood cells flowing in complex geometries. They modeled the cells as finite deformation elastic membranes containing a higher viscosity fluid than the surrounding plasma. The surface integrals were evaluated using an O(NlogN) particle- mesh Ewald (PME) approach. They used this model to simulate axisymmetric flows and also flow of blood cells at

30% volume fractions in tubes.

1.2.2 Capsule Dynamics in Non-Cylindrical Channels

In the field of microfluidics, a number of diagnostic devices and devices for capsule fabrication applications, are based on square and rectangular microchannels. But very few numerical studies have been conducted in order to investigate the flow dynamics of capsules in non-cylindrical channels.

Cordeiro and coworkers [9] experimentally studied the deformation and adhesion of polyelectrolyte capsules in a parallel plate flow chamber. Prevot and coworkers [48] designed a microfluidic system to study the behavior of polyelectrolyte capsules flowing in microchannels. Plastic deformation was observed when the capsule passes through the constriction. Fiddes and coworkers [20] investigated the flow dynamics of microgel capsules in topographically patterned microchannel experimentally. They investigated the effects of confinement, interaction between microgels and the channel surface and the velocities of microgels. They found that the wall surface charges effect the capsule velocity.

The lattice Boltzmann method has been used to study capsules in microfluidics [67, 26, 57, 58]. Zhu and coworkers [68, 67] studied a two-dimensional capsule driven through a 2-D microchannel with constriction by a pressure gradient in the lateral direction. They used a hybrid method integrating lattice Boltzmann and lattice spring methods to investigate how the compliance of both the particles and the confining walls affect the ability of the particles to become trapped within a pore

or constriction. They found that non-adhesive capsules moving through confined region experience a greater speedup with decreasing stiffness.

Bagchi [4] used the immersed boundary method to study the motion of an isolated cell and multiple cells through a two-dimensional rectangular channel. He modeled the cells as biconcave discs and the membrane was modeled as neo-Hookean and the channel dimension was much larger than the cell dimension. He found that the deformation decreases with increasing viscosity ratio and elastic resistance of the membrane. Doddi and Bagchi [13] studied the lateral migration of capsule between parallel plates. They found that the deformation of capsule increases with increasing capillary number and capsule size but decreases with increasing viscosity ratio. Lefebvre and coworkers [34] used the results from simulation of capsule motion in cylindrical tube to predict the elastic properties of capsules in microfluidic channels. There approach is suitable only for smaller capsules. Also microfluidic channels are mostly rectangular and hence this method is not applicable.

The above-mentioned studies use two-dimensional models for investigating the capsule motion and deformation. Griggs, Zinchenko and Davis [22] studied the motion of three-dimensional drops between two parallel planes in a low-Reynolds-number Poiseuille flow. They used a boundary-integral algorithm that employs Green's functions. They focused primarily on cases where drop size is comparable to the channel height. They found that at smaller capillary numbers the drops tend to maintain a nearly spherical shape. But as the capillary number increases, they found that the drop shape becomes non-axisymmetric at steady state and have a posterior dimple. They also found a significant effect of viscosity ratio on the drop velocity

and deformation. So far, to our knowledge the only three-dimensional computational study on the motion of capsule in non-axisymmetric geometry was conducted by Doddi and Bagchi [14]. They studied the dynamics of capsule in Poiseuille flow between parallel plates using a three-dimensional model. They simulated a large number of deformable cells and studied the trajectory and velocity fluctuation of individual cells using the immersed boundary method. For an initially spherical cell with size ratio of 0.8 they found that the front and rear ends of the cell become convex and concave, respectively, and sharp cusps develop at the trailing edges. But their study was limited to cells smaller than the channel.

In this thesis, we study elastic membranes with shearing and area-dilatation resistance but negligible bending resistance. This class represents a wide range of artificial capsules. Experimental findings for biocompatible alginate capsules [6], synthetic polysiloxane [24] and aminomethacrylate capsules [42] compare very well with theoretical models that ignore bending resistance. Therefore, several earlier theoretical investigations have focused on this class of problems, e.g. [44, 50, 52, 28, 29]. To a great extent, this model also applies to the human red blood cells where the interior hemoglobin solution is enclosed by a multi-layer membrane whose reduced bending modulus (with respect to its shearing resistance) is $O(10^{-3})$ [40, 52]. In this thesis, we study in detail the motion and deformation of capsules in cylindrical, square and rectangular channels. Our motivation is to study the capsule shape and flow properties in confined geometries. The deformed shape of capsule is of much importance in various microfluidic device such as sorting devices, capsule fabrication etc. Also, the deformability of red blood cells is an important factor enabling the

cells to carry out its various physiological functions. Many diseases like malaria changes the deformability of red blood cells and this results in inefficiency of these cells. Hence in this thesis we investigate the steady state shapes for different channel geometries for both small capsules and larger capsules with radius larger than the radius of the channel. In order to capture non-axisymmetric deformation we employ a three-dimensional model of the capsule flow. Our study has revealed that in case of rectangular microchannels the deformation is non-axisymmetric with three-dimensional effects. Capsules of size larger than the channel dimension deforming in square channels assume the shape of the channel. The results of this study may be useful in the design and operation of microfluidic devices.

1.3 Thesis Outline

Chapter 2 discusses the mathematical formulation of the problem including the relevant boundary integral equations. A brief description of the numerical implementation using the spectral boundary element method for membranes is also provided. The definition of geometric and physical parameters of the problem is also given in this chapter.

In Chapter 3, we investigate in detail the flow dynamics of microcapsules in square microchannels. We validate our methodology for the wall bounded flow by studying the capsule motion in cylindrical channel. We study the flow dynamics in a square channel and determine the effect of various parameters on the motion and deformation. In Chapter 4, we study the capsule flow dynamics in a rectangular

microchannel. Our motive was to investigate the effect of highly non-axisymmetric geometry on capsule deformation. We also present a comparative study of the capsule dynamics in square and rectangular channel. We study in detail both the transient and steady-state properties and how the various parameters affect these properties. In Chapter 5, we examine the capsule dynamics in a converging square channel. We study the transient properties for a capsule in the converging channel and investigate the effect of viscosity ratio, capsule size and capillary number on these properties.

In Chapter 6, we investigate the effect of a bump in the microchannel on the hemodynamic forces on a solid sphere which is representative of a leukocyte and also the forces on the bump which is representative of the endothelial cell.

Chapter 2

Mathematical Formulation and Numerical Algorithm

In this thesis, we study the capsule flow dynamics in microfluidics and the hemodynamic forces on blood cells in microvessels. Both of these studies are characterized by small length scales resulting in low Reynolds number Re. For small values of Re, the Navier-Stokes equation reduces to Stokes equation and hence our problem consists of solving the Stokes equation. Thus we use the boundary integral method for solving the Stokes equation. In this chapter the mathematical formulation and numerical algorithm is described.

2.1 Mathematical Formulation

We consider a volume of fluid 1 bounded by a surface S_B as shown in figure 2.1. Assuming low-Reynolds-number flows, the governing equations are the Stokes equations and continuity,

$$\nabla \cdot \boldsymbol{\sigma} \equiv -\nabla p + \mu \nabla^2 \boldsymbol{u} = 0 \tag{1}$$

$$\nabla \cdot \boldsymbol{u} = 0 \tag{2}$$

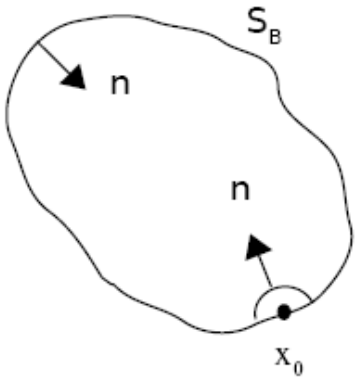

Figure 2.1: Illustration of the control volume.

where $\boldsymbol{\sigma}$ is the stress tensor, p the dynamic pressure, μ the viscosity of the fluid and $\boldsymbol{u}$ the fluid velocity. By introducing the fundamental solutions S_{ij} and T_{ijk} for the three-dimensional Stokes equation (1) and continuity (2), and then integrating over the fluid volume, the velocity at a point x_o on the surface is expressed by the following Boundary Integral Equation (BIE),

$$\boldsymbol{u}(\boldsymbol{x}_0) = -\frac{1}{4\pi\mu}\int_S \left[\boldsymbol{S}(\hat{\boldsymbol{x}})\cdot\boldsymbol{f}(\boldsymbol{x}) - \mu\,\boldsymbol{T}(\hat{\boldsymbol{x}})\cdot\boldsymbol{u}(\boldsymbol{x})\cdot\boldsymbol{n}(\boldsymbol{x})\right]\,dS \tag{3}$$

The fundamental solution for the velocity S_{ij} and the corresponding stress T_{ijk} are given by

$$S_{ij} = \frac{\delta_{ij}}{r} + \frac{\hat{x}_i\hat{x}_j}{r^3} \tag{4}$$

$$T_{ijk} = -6\frac{\hat{x}_i\hat{x}_j\hat{x}_k}{r^5} \tag{5}$$

where $\hat{\boldsymbol{x}} = \boldsymbol{x} - \boldsymbol{x_o}$ and $r = |\hat{\boldsymbol{x}}|$. Equation (3) relates the velocity $\boldsymbol{u}$ at each point $\boldsymbol{x}_0$ on the boundary S as a surface integral of the force vector $\boldsymbol{f} = \boldsymbol{n}\cdot\boldsymbol{\sigma}$ and the velocity $\boldsymbol{u}$ over all points $\boldsymbol{x}$ on the same boundary. The unit normal vector $\boldsymbol{n}$ points into the domain volume surrounded by the boundary S_B as shown in figure 2.1. A detailed derivation may be found in Pozrikidis [83]. The above equation solves for the fluid

flow inside a specific boundary S_B as shown in figure 2.1. Similarly the boundary integral equation for flow outside a volume V bounded by a surface boundary S_B can be obtained,

$$\boldsymbol{u}(\boldsymbol{x}_0) - 2\boldsymbol{u}^{\infty}(\boldsymbol{x}_0) = -\frac{1}{4\pi\mu}\int_{S_B} \left[\boldsymbol{S}(\hat{\boldsymbol{x}})\cdot\boldsymbol{f}(\boldsymbol{x}) - \mu\,\boldsymbol{T}(\hat{\boldsymbol{x}})\cdot\boldsymbol{u}(\boldsymbol{x})\cdot\boldsymbol{n}(\boldsymbol{x})\right]\, dS \quad (6)$$

where $\boldsymbol{n}$ points out of the boundary S_B and $\boldsymbol{u}^{\infty}$ is the undisturbed velocity in the absence of the volume V. Both the inner and the outer equations are used to solve the flow dynamics in complex geometries in this thesis.

2.2 Effect of Bump in a Microchannel

We consider a three-dimensional cell attached to the inner surface of a vessel as illustrated in figure 2.2 and a leukocyte above it at the center of the vessel. The center of the cell and the leukocyte are on the same vertical line. The vessel is modeled as a cylindrical tube with radius R and half length L. The leukocyte is modeled as a solid sphere of radius R_s. The attached cell is modeled as a spherical cap with radius a. The cell size is specified by its volume V or equivalently by the radius $\tilde{a}$ of a spherical cell with identical volume, i.e.

$$\tilde{a} = \left(\frac{3V}{4\pi}\right)^{1/3}. \quad (7)$$

Stokes flow of a Newtonian fluid around the bump is assumed. The leukocyte is enclosed by a closed boundary of fluid and cylinder wall and hence equation (3) applies to our study of the effect of bump in a microchannel on the hydrodynamic forces on the leukocyte. The undisturbed flow far from the cell is a Poiseuille flow

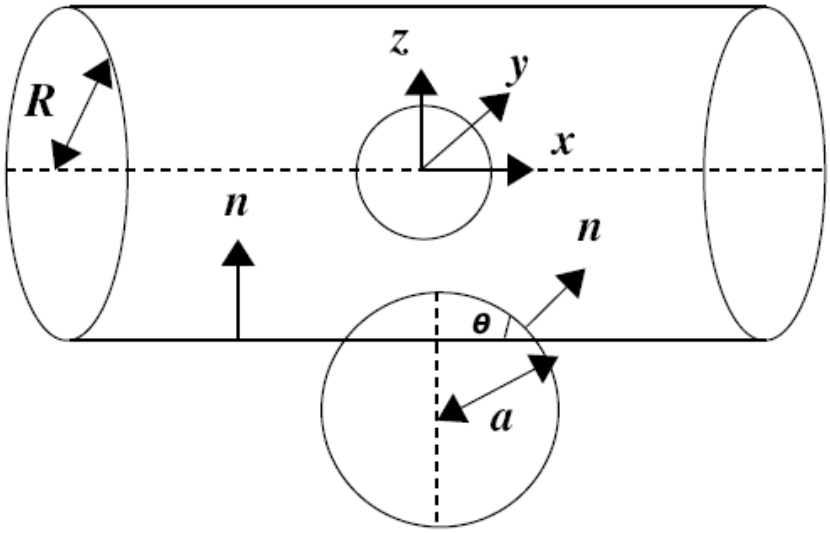

Figure 2.2: Illustration of a bump in a microvessel with a leukocyte moving along the centerline.

$\boldsymbol{u}^\infty = (u_x^\infty, 0, 0)$ with

$$u_x^\infty = U(1 - \frac{(y^2 + z^2)}{R^2}), u_y^\infty = 0, u_z^\infty = 0 \tag{8}$$

where U is the (maximum) velocity at the centerline. Hence the boundary condition at the cylinder ends is given by

$$\boldsymbol{u} = \boldsymbol{u}^\infty \quad \text{as } x \to \pm\infty \tag{9}$$

At the solid boundary the no-slip condition applies,

$$\boldsymbol{u} = 0 \quad \text{on the solid boundary} \tag{10}$$

2.3 A Capsule in a Microfluidic Channel

We consider a three-dimensional capsule with an elastic interface moving through a microchannel as shown in figure 2.3. The interior (fluid 1) and exte-

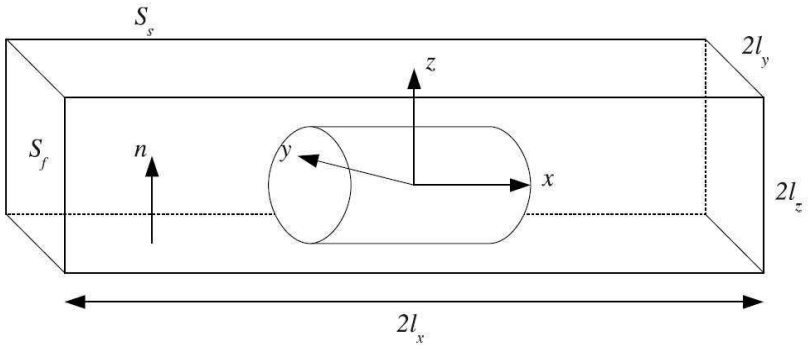

Figure 2.3: Illustration of a capsule moving along the centerline of a square microchannel.

rior (fluid 2) are Newtonian, with viscosity $\lambda\mu$ and λ. The capsule size is specified by its volume V or equivalently by the radius a of a sphere of volume $V = (4\pi/3)a^3$. The channel's half length is ℓ_x. For a cylindrical channel, the radius of cross-section is R while for square or rectangular channels, the half- lengths of the cross-section are ℓ_y and ℓ_z.

For a capsule with surface S_c moving through a microfluidic channel or vessel, bounded by the fluid domain S_f and the solid surface S_s as shown in figure 2.3, the velocity at any point $\boldsymbol{x}_0$ on the system surface can be obtained by combining equations (3) and (6). This results in the following boundary integral equation [76, 62]

$$\begin{aligned}\Omega \boldsymbol{u}(\boldsymbol{x}_0) = &\int_{S_c} \left(\boldsymbol{S}\cdot\Delta\boldsymbol{f} - \mu(1-\lambda)\,\boldsymbol{T}\cdot\boldsymbol{u}\cdot\boldsymbol{n}\right)\,dS \\ &- \int_{S_s} \left(\boldsymbol{S}\cdot\boldsymbol{f} - \mu\,\boldsymbol{T}\cdot\boldsymbol{u}\cdot\boldsymbol{n}\right)\,dS \\ &- \int_{S_f} \left(\boldsymbol{S}\cdot\boldsymbol{f} - \mu\,\boldsymbol{T}\cdot\boldsymbol{u}\cdot\boldsymbol{n}\right)\,dS \end{aligned} \tag{11}$$

where $\Omega = 4\pi\mu(1+\lambda)$ for $\boldsymbol{x_o}$ on the capsule interface S_c, while $\Omega = 4\pi\mu$ on the

fluid boundary S_f and the solid boundary S_s. This equation relates the velocity $\boldsymbol{u}$ at each point $\boldsymbol{x}_0$ on the boundary as a surface integral of the force $\boldsymbol{f} = \boldsymbol{n} \cdot \boldsymbol{\sigma}$ and the velocity $\boldsymbol{u}$ over all points $\boldsymbol{x}$ on the same boundary.

Owing to the no-slip condition at the interface, the time evolution of the material points of the membrane can be determined via the kinematic condition at the interface

$$\frac{\partial \boldsymbol{x}}{\partial t} = \boldsymbol{u} \tag{12}$$

The boundary conditions on the solid wall S_w and the fluid boundary S_f far away from the capsule are given by

$$\boldsymbol{u} = 0 \quad \text{on the solid surface } S_w \tag{13}$$

$$\boldsymbol{u} = \boldsymbol{u^\infty} \quad \text{on the fluid surface } S_f \tag{14}$$

where $\boldsymbol{u^\infty}$ is the undisturbed velocity in the tube or channel. For the case of a cylindrical channel, the velocity at the ends is the Poiseuille velocity given by the equation (8).

For a channel with rectangular cross-section, the undisturbed Poiseuille velocity $\boldsymbol{u}^\infty$ is

$$\frac{u_x^\infty}{C} = (\frac{(2\ell_z)^2}{4} - z^2) + \sum_{n=1}^{\infty} B_n \cosh(\frac{2\alpha_n y}{2\ell_z}) \cos(\frac{2\alpha_n z}{\ell_z}) \tag{15}$$

where

$$C = -\frac{1}{2\mu}\frac{\mathrm{d}p}{\mathrm{d}x} \tag{16}$$

$$B_n \cosh(\frac{\alpha_n \ell_y}{\ell_z}) = (-1)^n \frac{(2\ell_z)^2}{\alpha_n^3} \tag{17}$$

$$\alpha_n = \frac{(2n-1)\pi}{2} \tag{18}$$

(See pages 309-312 in Ref.[65]). The flow rate Q is found by integration to be

$$\frac{Q}{C} = \frac{(2\ell_y)(2\ell_z)^3}{6} + \sum_{n=1}^{\infty}(-1)^n \frac{(2\ell_z)^4}{\alpha_n^5}\sin(\alpha_n)\tanh(\frac{\alpha_n \ell_y}{\ell_z}) \tag{19}$$

where ℓ_y is the width and ℓ_z is the height of the channel. From equation (19) the average velocity is obtained as follows

$$\frac{U}{C} = \frac{(2\ell_y)^2}{6} + \sum_{n=1}^{\infty}(-1)^n \frac{(2\ell_z)^3}{2\alpha_n^5 \ell_y}\sin(\alpha_n)\tanh(\frac{\alpha_n \ell_y}{\ell_z}) \tag{20}$$

At the capsule interface S_c, the velocity is continuous and the surface stress vector $\Delta \boldsymbol{f}$ is defined using the stress tensor $\boldsymbol{\sigma}$ and the surface unit normal $\boldsymbol{n}$ pointing into fluid 2,

$$\boldsymbol{u} = \boldsymbol{u}_1 = \boldsymbol{u}_2 \tag{21}$$

$$\Delta \boldsymbol{f} \equiv \boldsymbol{n} \cdot (\boldsymbol{\sigma}_2 - \boldsymbol{\sigma}_1) \tag{22}$$

where the subscripts designate quantities evaluated in fluids 1 and 2.

To produce a closed system of equations, the surface stress $\Delta \boldsymbol{f}$ is determined from the membrane dynamics. The membrane description is based on the well-established continuum approach and the theory of thin shells [16]. The surface stress on the membrane is determined by the in-plane stresses, i.e. $\Delta \boldsymbol{f} = -\nabla_s \cdot \boldsymbol{\tau}$, where the in-plane stress tensor $\boldsymbol{\tau}$ is described using a constitutive law which relates $\boldsymbol{\tau}$'s eigenvalues (or principal elastic tensions $\tau_\beta^P, \beta = 1, 2$) with the principal stretch ratios λ_β. The constitutive law depends on the material composition of the membrane [45, 16].

The Skalak material law describing certain biological capsules (such as red

blood cells) as well as membranes obtained by interfacial polymerization is given by

$$\tau_1^P = \frac{G_s \lambda_1}{\lambda_2}(\lambda_1^2 - 1 + C\lambda_2^2[(\lambda_1\lambda_2)^2 - 1]) \tag{23}$$

(To calculate τ_2^P, reverse the λ_β subscripts.) In the equation above, G_s is the shearing modulus while C is a dimensionless area-dilatation modulus (scaled with the shearing modulus). Analysis in the limit of small deformations shows that the area-dilatation modulus is $K = G_s(1 + 2C)$ while the surface Young modulus is $E_s = 2G_s(1 + 2C)/(1 + C)$ [45].

In addition we assume that the capsule is subjected to a positive osmotic pressure difference $p^{(0)}$. For artificial capsules, a positive pressure difference may occur between inside and outside due to inflation or dilation of the internal medium or due to osmotic effects [29]. Risso, Colle-Paillot and Zagzoule [51] conducted experiments with artificial capsules and found that the deformed profiles do not agree with the numerical results. It was later found that the capsules studied experimentally were subjected to internal prestress due to osmotic phenomena and the application of prestress resulted in agreement between experimental and numerical results [33]. Following Lac and Barthès-Biesel [29], we define the prestress parameter α_p such that all lengths in the undeformed capsule would be scaled by $(1 + \alpha)$, relative to the reference shape. This is mathematically equivalent to scaling the stretch ratios by $(1 + \alpha_p)$[17]. For most of our studies, we have used a prestress $\alpha_p = 0.05$ which implies that the undeformed capsule would be 5% larger than the reference shape. In this case, the initial membrane tension owing to prestress is $\tau_0/G_s \approx 0.34$.

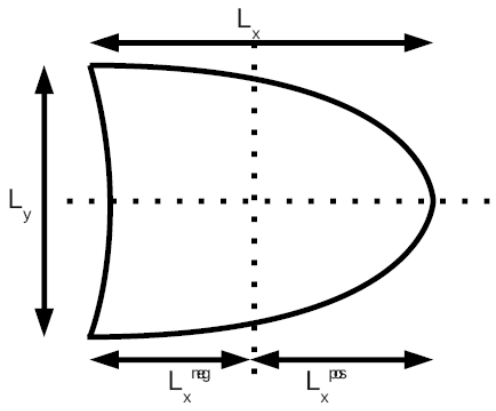

Figure 2.4: Definition of the geometric and physical parameters of a capsule moving along the centerline of a microchannel.

2.4 Definition of Physical Variables for Channel Flow

In order to quantify and compare the capsule deformation and dynamics in flow, we consider the transient evolution and steady-state values of several geometric and physical variables. To quantify the capsule deformation we monitor the capsule's longest and shortest semi-axes, L and S respectively. These semi-axes are determined as the maximum and minimum distance from the capsule centroid to the interface by employing a Newton method for the optimization problems. The actual capsule dimensions in the x, y, and z directions (L_x, L_y and L_z) are also calculated using a Newton method for the optimization. Because of the parachute shape formed during the capsule motion, we also monitor the length of the front L_x^{pos} and rear L_x^{neg} tip of the capsule from the capsule centroid.

During the capsule deformation, the interfacial curvature undergoes significant

changes and hence we monitor the curvature at the tips as well as the minimum and maximum curvature along the interfacial profile with the planes $y = 0$ and $z = 0$. We calculate the curvature at the downstream and upstream edges of the capsule (i.e. its intersections with the x-axis). The curvatures are determined along the capsule's $z = 0$ profile (i.e. the cross-section of the capsule surface with the $z = 0$ plane). In addition, we determine the maximum curvature along the capsule's $z = 0$ and $y = 0$ profile; to do this, from the actual spectral grid we interpolate spectrally to a dense grid with $N_B = 15$ basis points and find the higher value of the curvature among the spectral discretization points of the dense grid along the desired capsule's profile.

In this study, we assume that the flow rate Q (or average undisturbed velocity U) inside the channel is fixed. Thus we apply velocity boundary conditions at the channel's inlet and outlet and we solve for the fluid force at the channel ends. The fluid pressure at the channel's inlet and outlet, P_{in} and P_{out}, is determined as the surface-average of the normal force on these two surfaces, e.g.

$$P_{in} = \frac{-\int_{inlet} f_x \, \mathrm{d}S}{\int_{inlet} \mathrm{d}S} \tag{24}$$

(Note that although we have chosen this way to determine the pressure at the channel ends, our computational results show that the fluid normal force, or pressure, at each channel end is constant to at least 4 significant digits among the spectral discretization points.) The pressure difference at the channel ends is $\Delta P = P_{in} - P_{out}$ and we also calculate the additional pressure difference owing to the presence of the

capsule in the channel,

$$\Delta P^{+} = \Delta P - \Delta P^{nc} \tag{25}$$

where ΔP^{nc} is the pressure difference at the channel ends when no capsule is present in the channel. As the capsule moves in the channel, its volume-average velocity is determine from surface properties, i.e.

$$\boldsymbol{U} = \frac{1}{V}\int_{V} \boldsymbol{u}\,\mathrm{d}V = \frac{1}{V}\int_{S_c} (\boldsymbol{u}\cdot\boldsymbol{n})\,\boldsymbol{x}\,\mathrm{d}S \tag{26}$$

There are three dimensionless groups involved in the description of capsule flow dynamics in a channel: the viscosity ratio λ, area-dilatation modulus C and the capillary number Ca. Our membrane description involves two moduli, one for shearing and one for area-dilatation. The area-dilatation modulus C is dimensionless (scaled with the shearing modulus G_s). The shearing modulus G_s introduces the (elastic) capillary number (i.e. a ratio of viscous flow forces to resistive elastic forces on the membrane) defined as

$$Ca = \frac{\mu U}{G_s} \tag{27}$$

In this study, if no scale is present, the half-length ℓ_z of the channel cross-section is used as the length scale, the velocity is scaled with the average undisturbed velocity U, and thus time is scaled with ℓ_z/U. In addition, the pressure is scaled with $\mu U/\ell_z$ and the membrane tensions with G_s.

2.5 Numerical Implementation

We utilize the Interfacial Spectral Boundary Element algorithm for membranes developed by Dodson and Dimitrakopoulos [16] for free-suspended capsules to study

capsules in wall-bounded flows. This method has been used for studying the dynamics of strain-hardening and strain-softening capsules in strong planar extensional flows [16, 15] as well as the dynamics of erythrocytes in strong shear flows [17]. In this method, the numerical solution of the boundary integral equation (11) is achieved through the spectral boundary element method [76, 62, 12]. Briefly, each boundary is divided into a moderate number of surface elements which are parameterized by two variables ξ and η on the square interval $[-1, 1]^2$. The geometry and physical variables are discretized using Lagrangian interpolation in terms of these parametric variables. The base points (ξ_i, η_i) for the interpolation are chosen as the zeros of orthogonal polynomials of Gauss-type. This is equivalent to an orthogonal polynomial expansion and yields the spectral convergence associated with such expansions. The discretizations are substituted into the appropriate boundary integrals and the quadratures are evaluated using adaptive Gaussian quadrature.

The boundary integral equation (11) admits two different types of points. The collocation points $\boldsymbol{x}_0$ where the equation is required to hold and the basis points $\boldsymbol{x}$ where the physical variables $\boldsymbol{u}$ and $\boldsymbol{f}$ are specified or determined. The spectral boundary element method as implemented here employs collocation points $\boldsymbol{x}_0$ of Legendre–Gauss quadrature, i.e. in the interior of the elements. As a result the boundary integral equation holds even for singular elements, i.e. the elements which contain the corners of the channel geometry. In addition, we use basis points $\boldsymbol{x}$ of Legendre–Gauss–Lobatto quadrature, and thus the physical variables are determined in the interior and on the edges of the spectral elements [12, 62]. For the time integration, we employed the 2nd-order Runge-Kutta scheme with a typical

time step $\Delta t = 0.5 \times 10^{-3}$.

Chapter 3

Motion of an Elastic Capsule in a Square Microfluidic Channel

In this chapter, we study the wall-bounded motion of a capsule in a microfluidic channel with a square cross-section. To our knowledge there are no numerical studies for capsule flow in microchannels of square cross-section for three-dimensional flows. Square microchannels have been used in microfluidics as separation and sorting devices, for capsule formation and also for experimental investigations. Abkarian, Faivre and Stone [2] used a microfluidic constriction of square cross-section to study the deformation of red blood cells. They observed that the cell translates along the channel and eventually adopts the characteristic "parachute" shape. They also used a similar channel to design a differential manometer [1]. Hence, here we study in detail the flow dynamics of capsules in microchannels with square cross-section.

First, we present the validation of our methodology for capsule dynamics in wall-bounded flows by comparing our results with previous studies conducted in cylindrical channels. Next, we investigate the motion and deformation of a capsule in a square channel and study in detail how the various parameters affect the capsule flow dynamics in a square channel. We also present a comparison of capsule

deformation in cylindrical and square cross-section channel in order to see the effects of the channel's cross-section on capsule deformation.

3.1 Problem Description

We consider an initially spherical Skalak capsule with scaled area-dilation modulus $C = 1$, moving along the centerline of a straight microchannel. Three-dimensional views of the problem geometry are shown in figure 3.1. The capsule interior (fluid 1) and exterior (fluid 2) are Newtonian fluids, with viscosities $\lambda\mu$ and μ, and the same density. The capsule size is specified by its volume V or equivalently by the radius a of a sphere of volume $V = (4\pi/3)a^3$. For capsules with size $a > L_s$ where L_s is the half-length of the channel dimension, the initial droplet shape is defined as a prolate spheroid with two minor semi-axes and a major semi-axis. Far from the capsule, the flow approaches the undisturbed flow, which for a tube is given by the Poiseuille equation $\boldsymbol{u}^{\infty} = 2U\,(1 - (y^2 + z^2)/R^2, 0, 0)$ where U is the average velocity. For a square channel, the undisturbed flow far from the capsule is a steady unidirectional flow [65] given by equation (17).

Assuming low-Reynolds-number flows, the governing equations in both fluids are Stokes equations and continuity. The associated boundary integral equation (11) has been described in Chapter 2. The numerical solution of the boundary integral equation is achieved by employing the spectral boundary element method for membranes, which has been described in detail in Chapter 2.

The surface discretization of the geometry is illustrated in figure 3.1. For

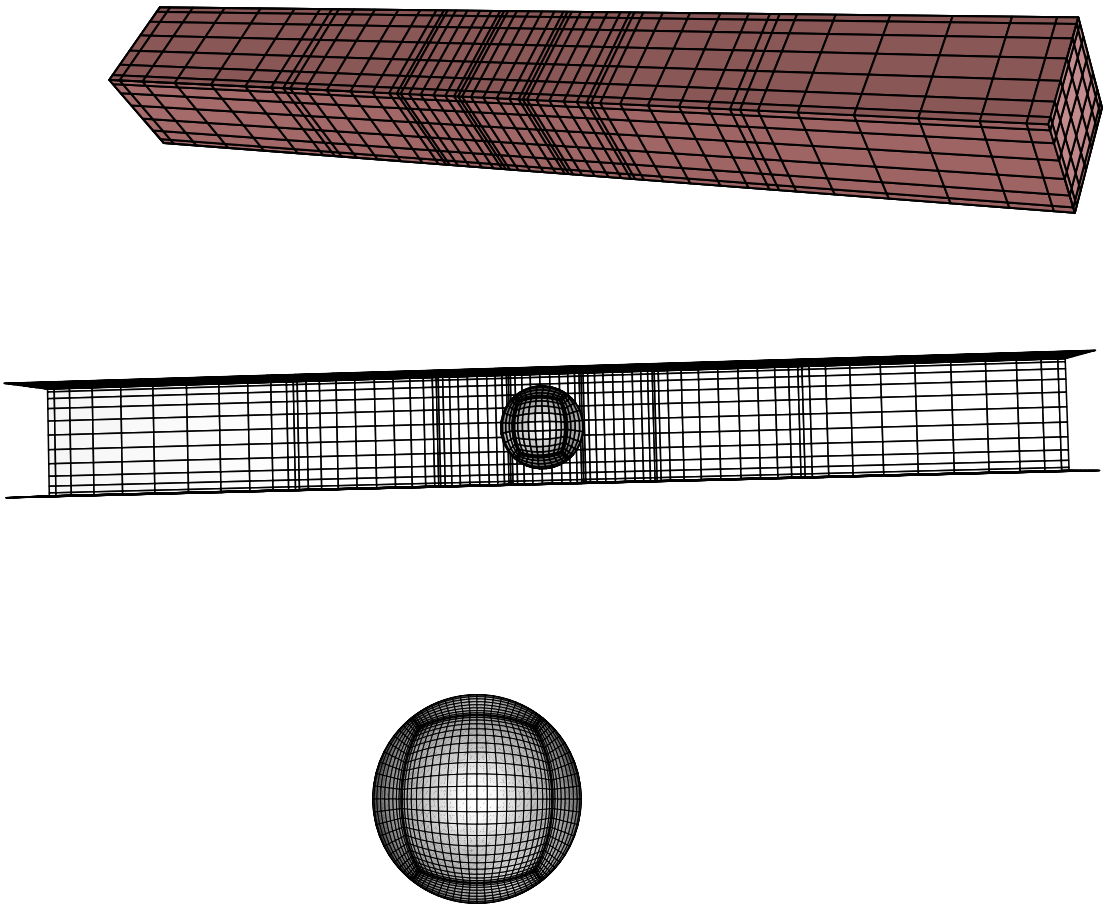

Figure 3.1: Spectral boundary element discretization of system surface:(a) solid surface of the channel along with the fluid surface at the channel end, (b) top view of the entire geometry after removing the channel's top side, and (c) capsule surface.

capsule in square channel, the computations were performed with a discretization employing $N_E = 36$ elements. The capsule surface, by being projected onto a cube, is divided into a total of 6 elements as shown in figure 3.1(c). The spectral element discretization of the channel surface follows the capsule's center of mass. The channel surface in the capsule vicinity is divided into a row of one spectral element per channel side (i.e. a total of four elements) with half-size equal to l_z. The channel surface is divided into four rows of four elements each; the length of each row progressively increases with the distance from the capsule surface as seen in figure 3.1(a). The channel surface (which formally should extend to infinity) has a half length l_x equal to 20 times the half-size of cross-sectional dimension l_z. Finally the channel's inlet and outlet are discretized into one element as shown in figure 3.1(a). In this study we mostly utilized $N_B = 12$ -14 basis points i.e. a total number of spectral points for the entire geometry N = $N_E N_B^2 = 5184$-7056.

For capsule in cylindrical channel, the computations were performed with a discretization employing $N_E = 30$ elements. The upstream and downstream channel surface is divided in the same manner as the square channel described above. The channel's inlet and outlet are discretized into five elements each.

The problem studied admits three symmetry planes, y=0, z=0 and y=z. Thus the memory requirements are reduced by a factor of 8^2, the computational time for the system matrices by a factor of 8 and the solution time via direct solvers of the linear systems by a factor of 8^3. There are two dimensionless groups involved in the description of capsule flow dynamics in a channel: the viscosity ratio λ and the capillary number Ca. Our membrane description involves two moduli, one

for shearing and one for area dilatation. The shearing modulus G_s introduces the (elastic) capillary number (i.e. a ratio of viscous flow forces to resistive elastic forces on the membrane) defined as

$$Ca = \frac{\mu U}{G_s} \tag{1}$$

where U is the average undisturbed velocity in the channel.

3.2 Validation

In this section we validate our method for capsule dynamics in wall-bounded flows by studying the capsule dynamics in a cylindrical tube and comparing with previous computational and experimental results. Axisymmetric flow of capsules in cylindrical tubes has been the subject of several numerical and experimental studies in the past. Capsule moving in a cylindrical channel being a representative of flowing cells in the microcirculation is one of the main motivating factor for such studies. Lefebvre and Barthès-Biesel [33] used the boundary integral method to study the motion of capsules in a cylindrical tube. Their model is valid for axisymmetric flows and they were able to reproduce the results from the experimental studies of Risso, Collè-Paillot and Zagzoule [51]. Risso *et al.* carried out an experimental investigation of bioartificial capsules flowing in tube. Secomb, Styp-Rekowska and Pries [53] investigated the flow of cells in microvessels experimentally using glass capillaries and numerically using a two-dimensional model for red blood cell deformation in microvessel.

To validate our method, we use our three-dimensional membrane algorithm,

determine the capsule motion along the centerline of a cylindrical tube and compare our results with published results for capsule motion in cylindrical tubes [33]. All comparisons have shown that our results are in very good agreement with earlier results from axisymmetric methodologies. For example, in tube flow and for a Skalak capsule with size $a = 0.8$, prestress $\alpha_p = 0.025$ and capillary number $Ca = 0.2$, we found $L_x = 1.68$ and $L_y = 1.52$, while for $a = 0.9$, $\alpha_p = 0.1$ and $Ca = 0.24$ we found $L_x = 2.03$ and $L_y = 1.60$; both results are in very good agreement with the results of Lefebvre and Barthès-Biesel [33] shown in their figures 4 and 7. The capsule profiles are also in very good agreement as we verified via figure superposition. Figure 3.2 shows the steady-state profile along the $z = 0$ plane of a Skalak capsule with size $a = 0.9$, capillary number $Ca = 0.24$ and viscosity ratio $\lambda = 1$, moving along the centerline of a cylindrical channel. The solid line is the result obtained using our method while the diamonds are the result from Lefebvre and Barthès-Biesel [33]. Lefebvre and Barthès-Biesel also reported in their table 1 that, for prestress $\alpha_p = 0.05$ and capsule size $a = 0.8$, the rear curvature changes sign when $Ca = 0.1$; we also found the same as shown in our figure 3.12.

3.3 Effects of the Capsule Size on the Steady-State Properties

In this section we collect our steady-state results on the geometric and physical variables of interest, described earlier in Chapter 2, as a function of the capsule size a for channel flow with capillary number $Ca = 0.1$. In particular, we consider Skalak

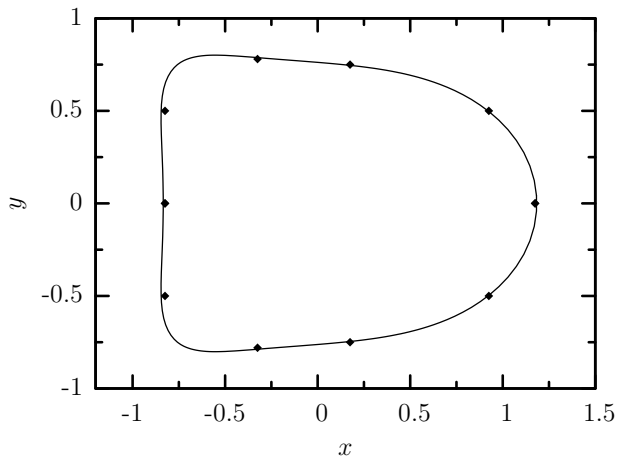

Figure 3.2: The steady-state profile along the $z = 0$ plane of a Skalak capsule with size $a = 0.9$, viscosity ratio $\lambda = 1$ and capillary number $Ca = 0.24$ moving along the centerline of a cylindrical channel. The prestress is α_p= 10. The diamonds represent the results from Lefebvre and Barthès-Biesel [33].

capsules with prestress $\alpha_p = 0.05$ and size $a = 0.1, 0.2, \ldots, 1.3$, i.e. both smaller and larger than the channel width ℓ_z. To obtain these steady-state results, for capsules with size $a < 1$ we initiated our computations from a spherical capsule at the channel centerline and computed the capsule dynamics for viscosity ratio $\lambda = 1$ until times $t = 10$–20, i.e. well-past steady-state. For capsules with size $a \geq 1$, we did the same but we initiated our computations from an ellipsoidal capsule with width near 0.95 and appropriate length (greater than unity) to account for the specific capsule volume.

To facilitate the comparison of the channel flow with that in a cylindrical tube, we include our results for tube motion in several figures in this section. However our discussion on these comparisons is presented at this end of this section. It is of interest to note that as the capsule size a increases, negative tensions appear near steady state and cause numerical instability, i.e. the specific prestress used in our study ($\alpha_p = 0.05$) is not adequate to enforce positive membrane tensions at sufficiently large capsules. Thus for this prestress we are unable to determine stable steady-state shapes for size $a \geq 1.4$ for channel flow and $a \geq 1.2$ for tube flow.

Figure 3.3 shows the effects of the capsule size a on the steady-state capsule dimensions. The capsule length L_x shows a monotonic increase with a while its width L_z, after an initial fast increase, slows down as it reaches the channel width. It is of interest to note that both dimensions increase identically until size $a \approx 0.9$ and then their behavior diverges. For higher capsule sizes, as the capsule width L_z is restricted by the channel width, the capsule length L_x increases faster to accommodate the capsule's larger volume. Considering the downstream and upstream parts of the

capsule length in figure 3.3(b), we see that after an initial common increase, the upstream length L_x^u increases slower for sizes $0.5 \lesssim a \lesssim 0.9$, and then shows a fast increase similar to that of the downstream length L_x^d.

To explain the behavior of the upstream length L_x^u, it is beneficial to see the steady-state $y = 0$ profiles of small and large capsules plotted in figure 3.4($a,\ c$). For small capsule sizes $a \lesssim 0.4$, the hydrodynamic forces associated with the flow rate $Ca = 0.1$ are weak and cause minimal deformation; thus the capsule is nearly spherical. For moderate capsule sizes $0.5 \lesssim a \lesssim 0.9$, the length L_x and the width L_z are practically equal to their undisturbed value $2a$; however the hydrodynamics forces are stronger and cause the capsule to deform into a shape which is rounded in front and blunted in the rear. Because of this interfacial deformation, the capsule centroid is shifted to the back, i.e. its upstream length L_x^u decreases with respect to its downstream length L_x^d. For size $a \approx 0.9$, the capsule width L_y has reached the channel's width and further increase is limited owing to the strong hydrodynamics forces in the gap between the capsule surface and the wall. The capsule obtains a bullet-like shape and further increase in its size results mainly in a length increase, and thus increases of both downstream and upstream parts of the capsule length.

Looking at the $x = 0$ profile of the different capsules included in figure 3.4($b,\ d$), we observe that the capsule remains axisymmetric until $a \approx 0.8$. At higher sizes, the capsule's $x = 0$ profile becomes a square with rounded corners, especially for the larger capsules, as seen in figure 3.4(d). Thus, the capsule interface becomes parallel to the channels walls and rounded at the channel's corners. This development clearly suggests that for capillary number $Ca = 0.1$, the capsule dynamics becomes non-

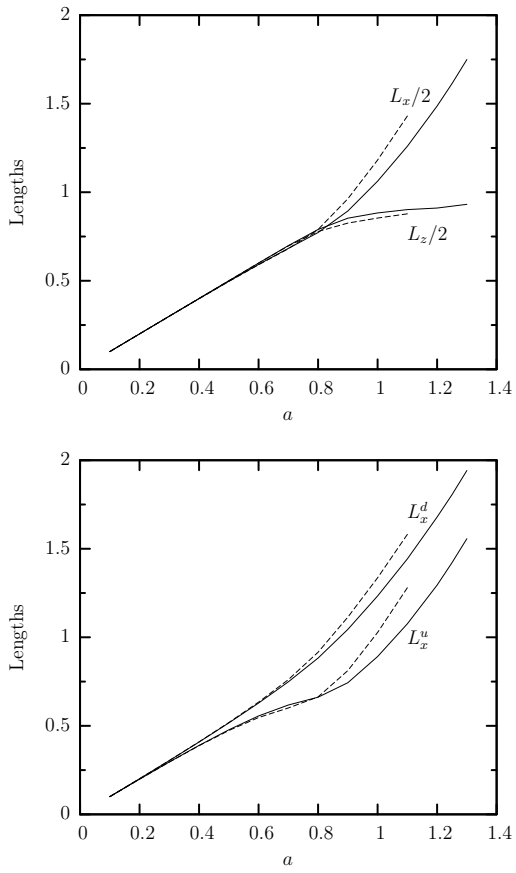

Figure 3.3: Steady-state capsule lengths as a function of the capsule's size a for a Skalak capsule with $C = 1$, $\alpha_p = 0.05$ and capillary number $Ca = 0.1$, in a square channel (——) and a cylindrical tube (– – –). (a) Capsule lengths $L_x/2$ and $L_z/2$. (b) Capsule lengths L_x^d and L_x^u.

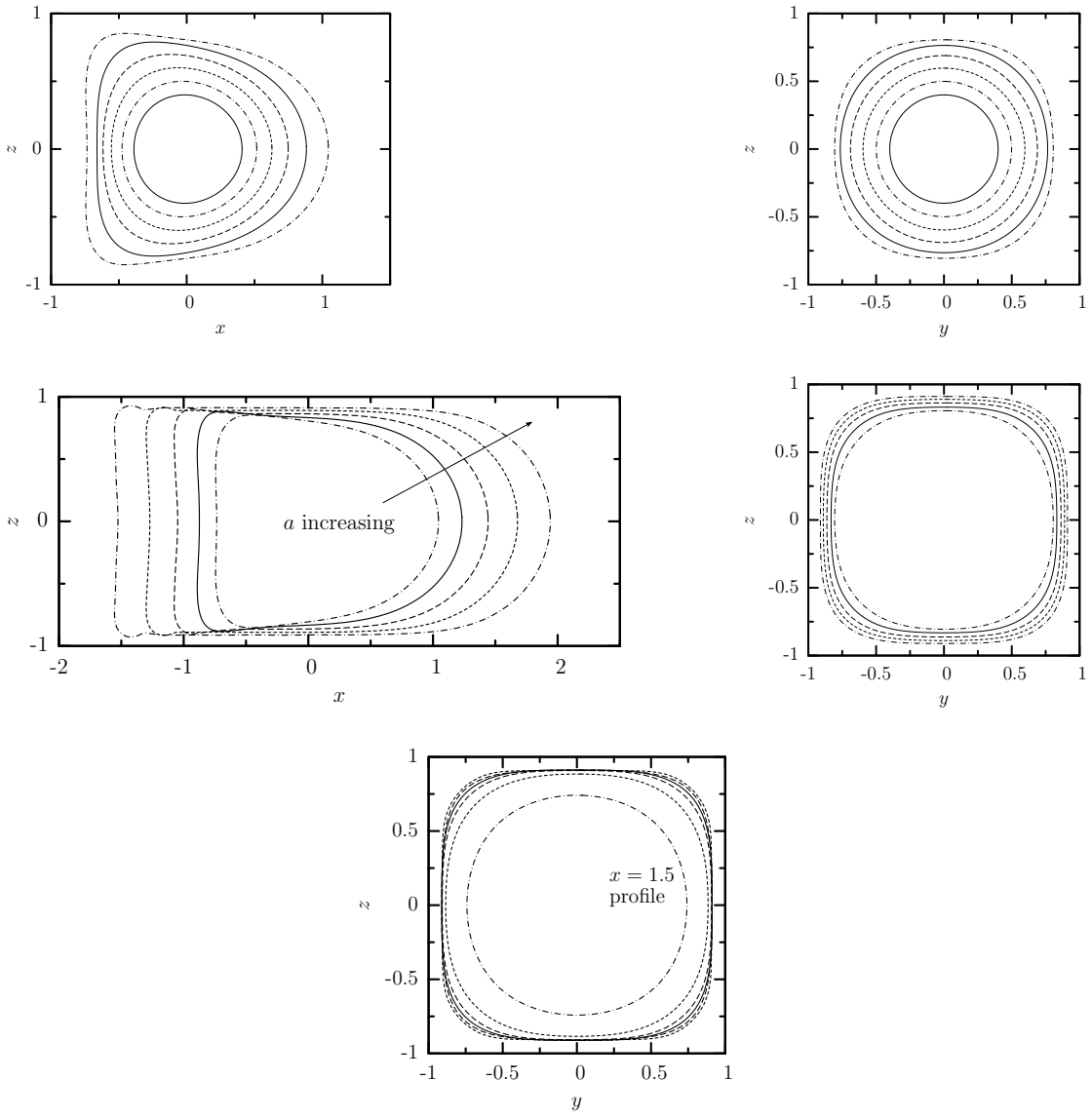

Figure 3.4: Steady-state profile of a Skalak capsule with $C = 1$, $\alpha_p = 0.05$ and capillary number $Ca = 0.1$ in a square channel. (a) Capsule $y = 0$ profile (i.e. interface intersection with the plane $x = 0$) for size $a = 0.4, 0.5, 0.6, 0.7, 0.8, 0.9$. (b) As in (a) but for $x = 0$ profile. (c) Capsule $y = 0$ profile for size $a = 0.9, 1, 1.1, 1.2, 1.3$. (d) As in (c) but for $x = 0$ profile. (e) Interface intersection with the planes $x = -1, -0.5, 0, 0.5, 1, 1.5$ for size $a = 1.3$. All profiles are shown with centroid $\boldsymbol{x}_c = \mathbf{0}$.

axisymmetric (i.e. fully three-dimensional) for capsule sizes $a \geq 0.9$, and therefore it is expected to deviate from its behavior in cylindrical tubes.

It is of interest to note that this non-axisymmetric interfacial deformation is associated mainly with the capsule's upstream portion (i.e. from its centroid to its real end), and not with its downstream portion which remains axisymmetric. To show this, in figure 3.4(e) we plot the capsule's interface intersection with different x-planes (with respect to the capsule centroid). The profiles at $x = 1, 1.5$ are circular and thus the downstream portion of the capsule is like a cylindrical cap.

The three-dimensional shapes of two large capsules with size $a = 1.1, 1.3$ are shown in figure 3.5. Beyond the dimple with negative curvature which occurs at the capsule's rear end, we also observe the development of dimples at the capsule lateral surface and near its rear, at each side of the channel. This lateral dimple is also shown in the capsule profiles in figure 3.4(d). Similar lateral dimples can be seen in the experimental photos (i.e. capsule profiles) of large capsules moving in square microfluidic channels in the recent work of Lefebvre *et al.* [34]. (See figures 10 and 11 in the earlier study.) In addition, lateral dimples have also been found on large capsules moving in cylindrical tubes, in experimental and computational studies, although in this case the dimple is, obviously, axisymmetric [49, 51].

Figure 3.6(a) shows the effects of the capsule size on the steady-state scaled curvature at the downstream and upstream edges of the capsule (i.e. its intersections with the x-axis). Note that the curvatures are scaled with the curvature of the undisturbed spherical shape, and thus this figure is more suited for the capsules with size smaller than the channel's width. This plot shows that even at small sizes $a \leq$

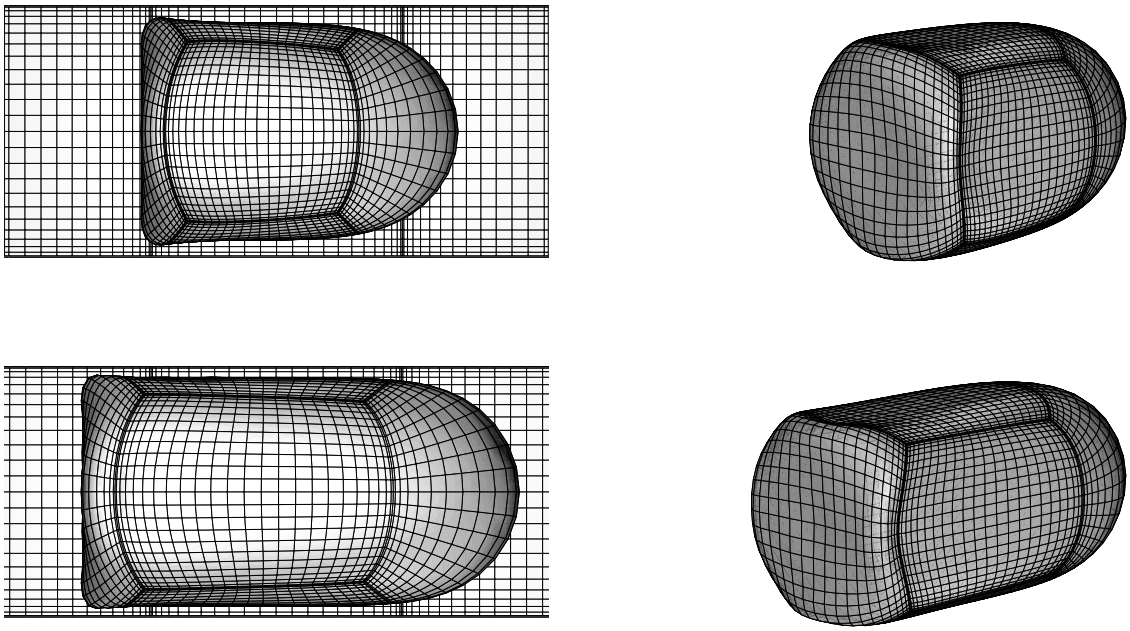

Figure 3.5: Steady-state shape of a Skalak capsule with $C = 1$, $\alpha_p = 0.05$ and capillary number $Ca = 0.1$ in a square channel. Capsule's size: (a) $a = 1.1$, and (b) $a = 1.3$.

0.4, the capsule downstream edge becomes more pointed while the opposite happens at its upstream edge. (Note that this small deformation cannot be observed in the capsule profiles shown in figure 3.4(a).) For moderate capsule sizes $0.4 \leq a \leq 0.9$, the significant capsule deformation shown earlier in figure 3.4(a) is associated with a faster increase of the curvature at the downstream edge and a faster decrease of the curvature at the upstream edge. Thus the downstream edge becomes more pointed (relatively to the undisturbed spherical shape) while the upstream edge flattens as seen in the profiles of figure 3.4(a). Note that a dimple with negative curvature has been developed at the rear end of the capsule with size $a = 0.9$.

In figure 3.6(b) we present the variation with the capsule size of the (unscaled) curvature at the downstream and upstream edges of the capsule. Thus this figure is more suited for the larger capsules where the capsule covers almost the entire channel width. This plot shows that for large capsules, e.g. $a \geq 0.9$, the curvature at the downstream edge decreases slightly only with the capsule size (i.e. it is practically independent of the size a). Similar is the variation of the curvature at the upstream edge which becomes slightly more negative with the capsule size.

Figure 3.6(c) shows the maximum curvature along the capsule's $z = 0$ profile (scaled with the curvature of the undisturbed spherical shape). This figure shows that the variation of the maximum profile curvature with the capsule size is divided into three distinct areas owing to the corresponding types of capsule profiles shown earlier in figure 3.4. In particular, for small sizes, $a \lesssim 0.4$, the maximum curvature occurs at the downstream edge of the nearly spherical capsules. For moderate sizes, $0.4 \lesssim a \lesssim 1$, the maximum curvature increases fast with the size owing to the

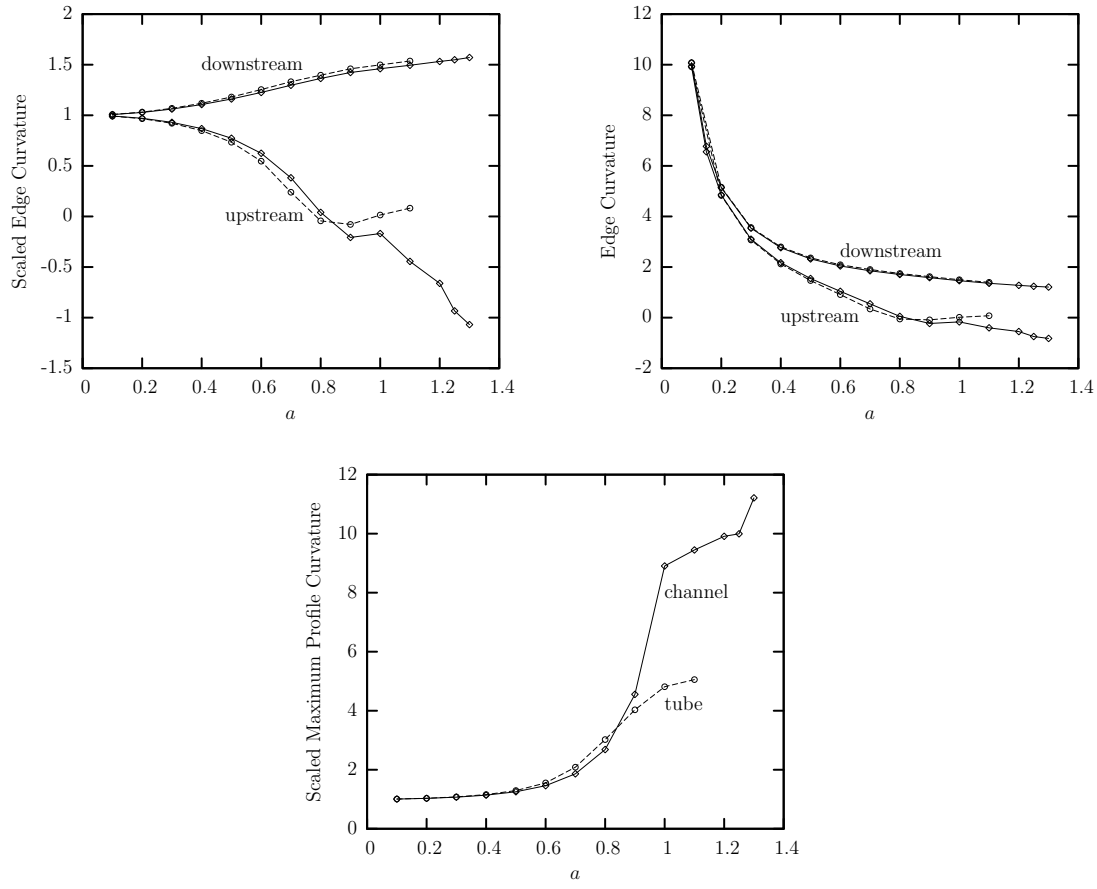

Figure 3.6: Steady-state capsule curvatures as a function of the capsule's size a for a Skalak capsule with $C = 1$, $\alpha_p = 0.05$ and capillary number $Ca = 0.1$, in a square channel (——) and a cylindrical tube (– – –). (a) Scaled curvature at the downstream and upstream edges of the capsule (i.e. its intersections with the x-axis). The curvatures are determined along capsule's $z = 0$ profile (i.e. the cross-section of the capsule surface with the $z = 0$ plane). (b) As in (a) but for unscaled curvatures. (c) Maximum scaled curvature along the capsule's $z = 0$ profile. In (a) and (c) the curvatures are scaled with the curvature of the undisturbed spherical shape.

development of the tail at the capsule rear and close to the walls. Finally, for large sizes, $a \gtrsim 1$, a further increase of the maximum curvature occurs owing to the development of the lateral dimple near the capsule rear. Thus, large capsules develop at their rear tail and close to the walls, pointed local areas characterized by a local length scale (or radius of curvature) which is of $O(10)$ higher than the capsule size, as we also found for moderate-size capsules at high flow rates in section 3.4.

We now turn our attention to properties associated with the entire capsule deformation, and in figure 3.7 we present the variation with the size a of the capsule's surface area S_c and the maximum principal tension τ^P_{max} on the membrane. After an initial slow increase at small capsule sizes, both properties increase fast with the capsule size for large capsules. Even for the large capsules studied in this section, the maximum tension τ^P_{max} at steady-state is always located at the downstream element of the capsule, along the $z = 0$ (or $y = 0$) profile and between the capsule downstream tip and the element end. Therefore this location is the most probable to rupture when a capsule flows in a microchannel.

Figure 3.8 shows the steady-state variation with the capsule size a of the volume-average capsule velocity U_x and the additional pressure difference ΔP^+ as well as the minimum distance h between the capsule surface and the channel's walls. In contrast to the insensitivity of these variables with the flow rate Ca found in section 3.4, now we observe that the capsule velocity U_x decreases and the pressure drop ΔP^+ increases significantly as the capsule size increases owing to the smaller gap h between the capsule surface and the walls. It is of interest to note that capsules, larger than the channel width, move with a velocity just higher than the

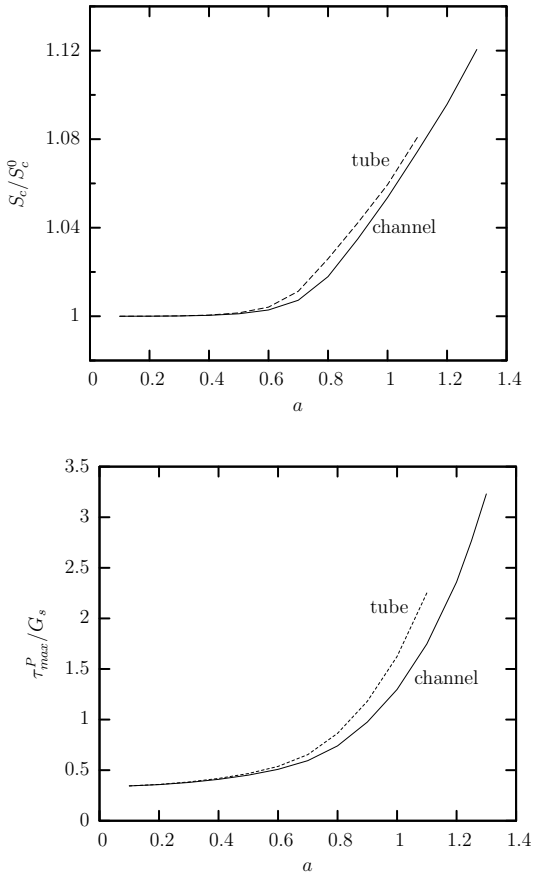

Figure 3.7: Steady-state capsule properties as a function of the capsule's size a for a Skalak capsule with $C = 1$, $\alpha_p = 0.05$ and capillary number $Ca = 0.1$, in a square channel (——) and a cylindrical tube (– – –). (a) Surface area of the capsule at steady state S_c (scaled with the surface area S_c^0 of the undisturbed spherical shape). (b) Maximum principal tension τ_{max}^P among the spectral discretization points on the membrane.

channel's undisturbed average velocity U and cause a very significant pressure drop in the channel.

3.3.1 Comparison with Flow in a Cylindrical Tube

As shown in figure 3.3, the behavior of the capsule lengths in tube flow for increasing capsule size is similar to that in the channel. In the latter geometry, large capsules are less deformed, and thus less extended in the flow direction and more extended laterally, owing to the existence of the corners' area which permits flow of the surrounding flow and thus causes less deformation on the capsule.

Figure 3.6(a, b) shows that the curvature at the downstream edge is practically the same for both solid systems. The same is true for the curvature at the upstream edge until sizes near $a = 0.8$; for higher capsule sizes, the upstream curvature is practically constant in tube flow but decreases into higher negative values in channel flow. This behavior in the tube is consistent with the results of Lefebvre and Barthès-Biesel [33] who showed at their table 1 that for capsule sizes $a = 0.8, 0.9, 1$ the upstream curvature is practically zero for a fixed capillary number and not very small prestress. (In particular for $Ca = 0.1$ when $\alpha_p = 0.05$ and $Ca = 0.2$ when $\alpha_p = 0.1$.)

The identical curvature evolution at the downstream edge in both solid systems can be understood since in both systems the downstream portion of the capsule remains axisymmetric as we show for the channel flow in figure 3.4(e). On the other hand, the different upstream curvature in the tube and channel at high enough cap-

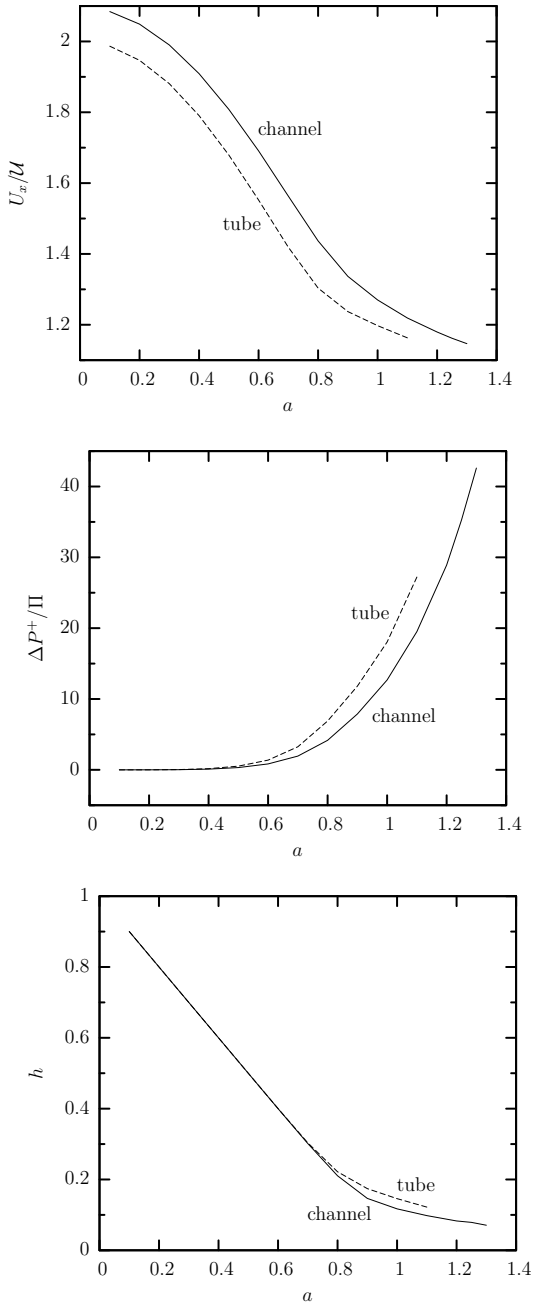

Figure 3.8: Steady-state capsule properties as a function of the capsule's size a for a Skalak capsule with $C = 1$, $\alpha_p = 0.05$ and capillary number $Ca = 0.1$, in a square channel (——) and a cylindrical tube (– – –). (a) Capsule velocity U_x. (b) Additional pressure drop ΔP^+. (c) Minimum distance h between the capsule surface and the channel's walls.

sule sizes can be attributed to the development of the (non-axisymmetric) rounded square shape of the upstream portion of the capsule for sizes $a \geq 0.9$ as shown in figure 3.4(d). For the same reason, a large capsule in a tube flow does not show as high maximum profile curvature as in a channel (figure 3.6(c)).

The higher interfacial deformation in the tube flow for large capsules results in a higher surface-area increase and higher membrane tensions as seen in figure 3.7. Figure 3.8(a) shows that a capsule in a tube has always lower velocity than in a channel while this difference decreases at large capsule sizes. We note that in this figure the velocity is scaled with the average fluid velocity U which is an appropriate scale mainly for large capsules. (As shown in this figure, small-size capsules travel with the maximum fluid velocity while large capsules travel with a velocity closer to the average fluid velocity.) Even when we scale our velocity findings with the maximum fluid velocity in each solid system (not shown), we observe that small- and moderate-size capsules travel slower in the tube. Owing to the existence of the corners' area, a capsule in a channel causes less fluid blocking, and thus a smaller pressure drop compared to that in a tube, as shown in figure 3.8(b).

3.4 Effects of the Capillary Number on the Steady-State Properties of Moderate-Size Capsules

In this section we collect our steady-state results on the geometric and physical variables of interest, described earlier in Chapter 2, as a function of flow rate for moderate-size capsules. In particular, we consider Skalak capsules with prestress

$\alpha_p = 0.05$ and size $a = 0.6, 0.7, 0.8$ (i.e. smaller than the channel size ℓ_z) and capillary number Ca in the range $[0, 0.5]$ (i.e. small and moderate flow rates). To obtain these steady-state results we initiate our computations from a spherical capsule at the channel centerline using viscosity ratio $\lambda = 1$ and compute the capsule dynamics until times $t = 10$–20, i.e. well-past steady-state which usually is achieved around time $t = 2$–4. Although the transient evolution is affected by the viscosity ratio, at steady-state there is no flow inside the capsule and thus the steady-state capsule properties are independent of the inner viscosity. For the same reason, the membrane viscosity (if any), which is not accounted in our computations, does not affect the capsule's steady-state properties.

Figure 3.9 shows the effects of the capillary number on the steady-state capsule dimensions for the three capsule sizes studied in this section. The capsule length $L_x/(2a)$ first decreases with the flow rate and then increases. For the three capsules studied here, only the largest capsule with $a = 0.8$ achieves eventually a length greater than its undisturbed size. On the other hand, the behavior of the capsule width L_z depends on the capsule size. The two smaller capsules with $a = 0.6, 0.7$ increase slightly their width $L_z/(2a)$ as the flow rate increases, however for $a = 0.8$ the capsule width $L_z/(2a)$ is decreased with the flow rate. This behavior can be attributed to the non-monotonic behavior of the capsule length L_x owing to the preservation of the capsule volume.

Dividing the capsule length L_x into its downstream and upstream parts (based on the capsule centroid), figure 3.9(b) shows that the capsule's downstream length L_x^d/a shows a monotonic increase with the flow rate and the capsule size, similar to

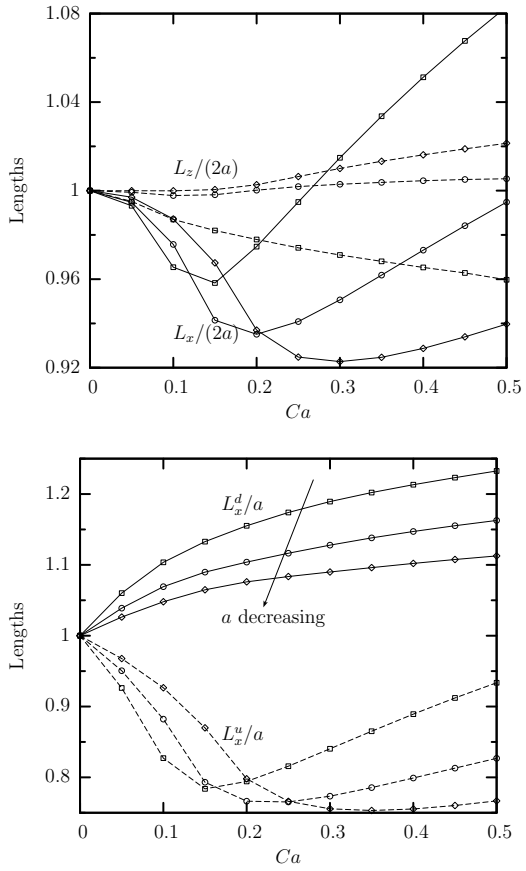

Figure 3.9: Steady-state capsule lengths as a function of the capillary number Ca for a Skalak capsule with $C = 1$ and $\alpha_p = 0.05$. (a) Capsule lengths $L_x/(2a)$ and $L_z/(2a)$. (b) Capsule lengths L_x^d/a and L_x^u/a. Capsules sizes a: $\diamond, 0.6; \circ, 0.7; \square, 0.8$.

that for the maximum capsule length L/a. In addition, the capsule upstream length L_x^u/a first decreases with the flow rate and then increases. Therefore, figure 3.9(b) suggests that the capsule's flow dynamics can be divided into two parts: the downstream dynamics where a monotonic dependence (e.g. length increase) is found with the flow rate, and the upstream part which is characterized by a more complicated flow dynamics and which may affect the capsule entire geometry.

The effects of the capillary number on the downstream and upstream lengths of the capsule, L_x^d and L_x^u, can also be seen in the $y = 0$ profiles of a capsule with size $a = 0.8$ presented in figure 3.10(a) since all these profiles have the same centroid $\boldsymbol{x}_c = \mathbf{0}$. The monotonic increase of L_x^d/a with the flow rate results from the relatively extension of the downstream tip of the capsule. On the other hand, the late flow-rate increase of the upstream length L_x^u/a results from the development of a pointed tail at the capsule rear close to the solid walls. Looking at the capsule $x = 0$ profiles (i.e. perpendicular to the flow direction) presented in figure 3.10(b), we observe that even for the largest capsule (size $a = 0.8$) and at the highest flow rate ($Ca = 0.5$) studied in this section, the capsule remains almost axisymmetric. This clearly suggests that the channel dynamics of capsules with sizes less than the channel size and in small and moderate flow rates should be similar to their dynamics in cylindrical tubes studied in earlier papers, e.g. [49, 51, 33].

For a better view of the three-dimensional capsule shape, in figure 3.11 we present the steady-state capsule shape for size $a = 0.8$ and for capillary number $Ca = 0.1, 0.5$. For each case, we plot the shape perpendicular to the flow direction inside the channel and askew from the flow direction. Note that the three-

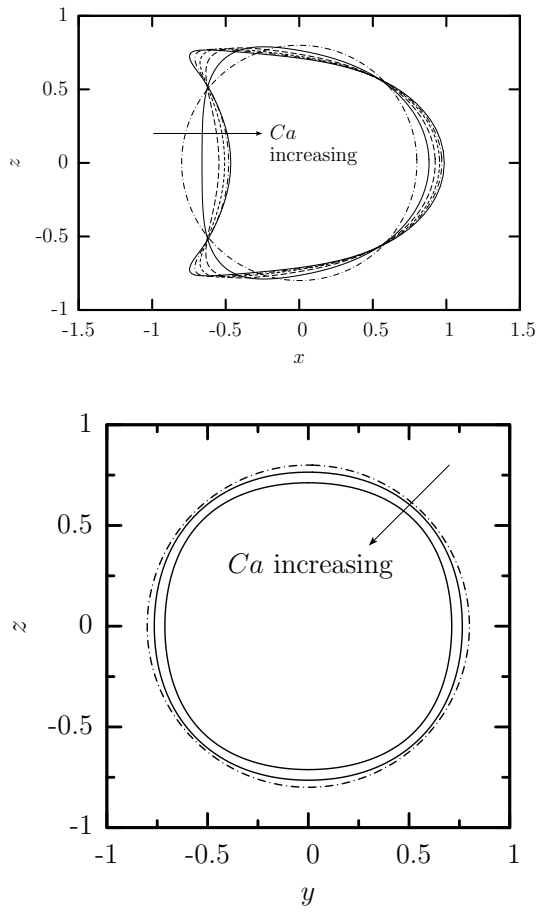

Figure 3.10: Steady-state capsule profile as a function of the capillary number Ca for a Skalak capsule with $C = 1$, $\alpha_p = 0.05$ and size $a = 0.8$. (a) Capsule $y = 0$ profile (i.e. interface intersection with the plane $x = 0$) for $Ca = 0, 0.1, 0.2, 0.3, 0.4, 0.5$ (b) Capsule $x = 0$ profile for $Ca = 0, 0.1, 0.5$. All profiles are shown with centroid $\boldsymbol{x}_c = \mathbf{0}$.

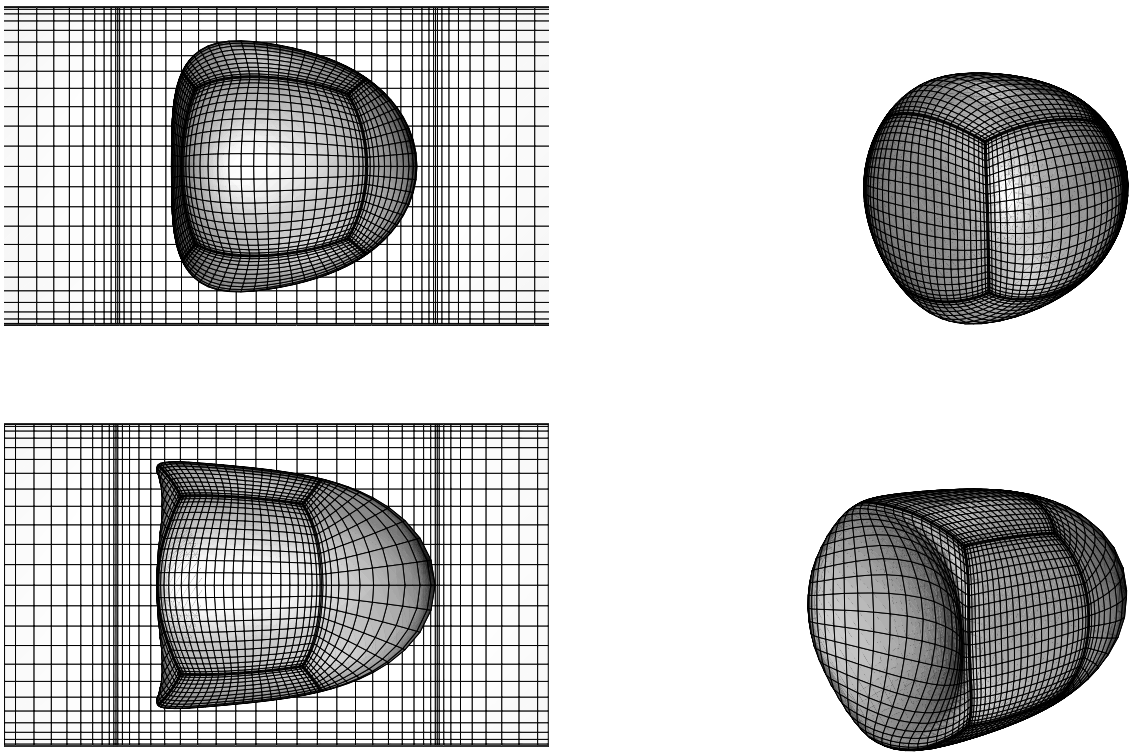

Figure 3.11: Steady-state shape of a Skalak capsule with $C = 1$, $\alpha_p = 0.05$ and size $a = 0.8$. Capillary number: (a) $Ca = 0.1$, and (b) $Ca = 0.5$.

dimensional views of the capsule shape presented in this paper were derived from the actual spectral grid by spectrally interpolating to $N_B = 25$ and using orthographic projection in plotting.

Figure 3.12 shows the effects of the flow rate Ca on the steady-state capsule curvatures along the capsule's $z = 0$ profile. As the flow rate increases, the capsule downstream edge becomes more pointed while the scaled curvature there increases slightly with the capsule size. At the same time, the capsule tends to decrease the curvature at its upstream edge from a concave shape at small Ca towards a flat edge and then a convex edge (with negative curvature) as the flow rate increases.

(Both effects are also shown in the capsule $y = 0$ profiles presented in figure 3.10.) For the three capsule sizes studied here, the transition to a convex edge occurs around $0.1 \leq Ca \leq 0.2$ and happens at a smaller flow rate as the capsule size increases. After a slow increase at very small flow rates, the maximum curvature along the capsule's $z = 0$ profile increases linearly with the capillary number as seen in figure 3.12(b). The scaled maximum curvature also increases with the capsule size. Thus the capsule develops very pointed tails at its upstream section characterized by a local length scale (or radius of curvature) which is of $O(10)$ (or more) higher than the capsule size for the maximum flow rate, $Ca = 0.5$, studied here.

Considering the variation of the capsule surface area S_c with the flow rate (which can be regarded as an index of the entire capsule deformation), figure 3.13(a) shows that after an initial slow increase at small flow rates, the steady-state surface area S_c increases linearly with the capillary number while capsules with larger size show a higher surface area increase. The same pattern is valid for the maximum principal tension τ^P_{max} on the membrane as seen in figure 3.13(b). It is interesting to note that the maximum tension τ^P_{max} at steady-state is always located at the downstream element of the capsule, along the $z = 0$ (or $y = 0$) profile and between the capsule downstream tip and the element end. Therefore this location is the most probable to rupture when a capsule flows in a microchannel.

Figure 3.14 shows the steady-state variation with the flow rate of the volume-average capsule velocity U_x and the additional pressure difference ΔP^+ as well as the minimum distance h between the capsule surface and the channel's walls. Note that the gap is $h = (2 - L_y)/2$ for the cases studied in this paper since no anomaly,

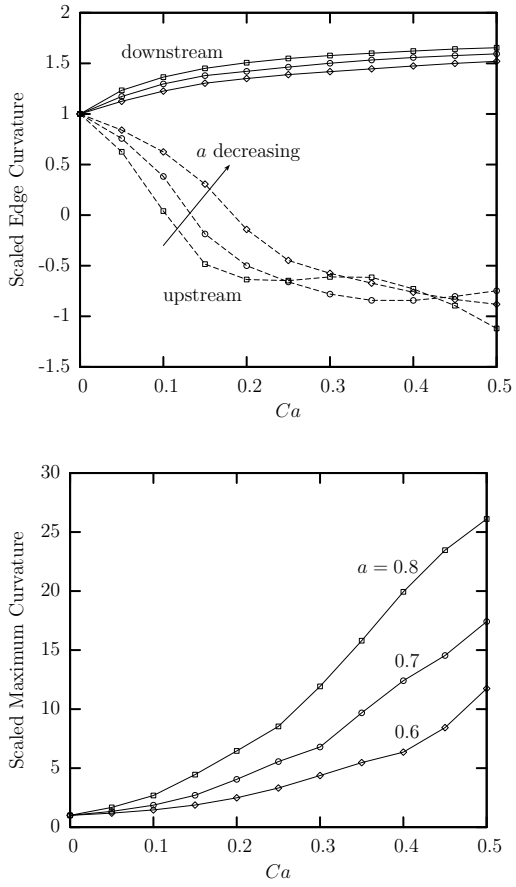

Figure 3.12: Steady-state capsule curvatures as a function of the capillary number Ca for a Skalak capsule with $C = 1$ and $\alpha_p = 0.05$. (a) Curvature at the downstream and upstream edges of the capsule (i.e. its intersections with the x-axis). The curvatures are determined along capsule's $z = 0$ profile (i.e. the cross-section of the capsule surface with the $z = 0$ plane). (b) Maximum curvature along the capsule's $z = 0$ profile. All curvatures are scaled with the curvature of the undisturbed spherical shape. Capsules sizes a: $\diamond, 0.6; \circ, 0.7; \square, 0.8$.

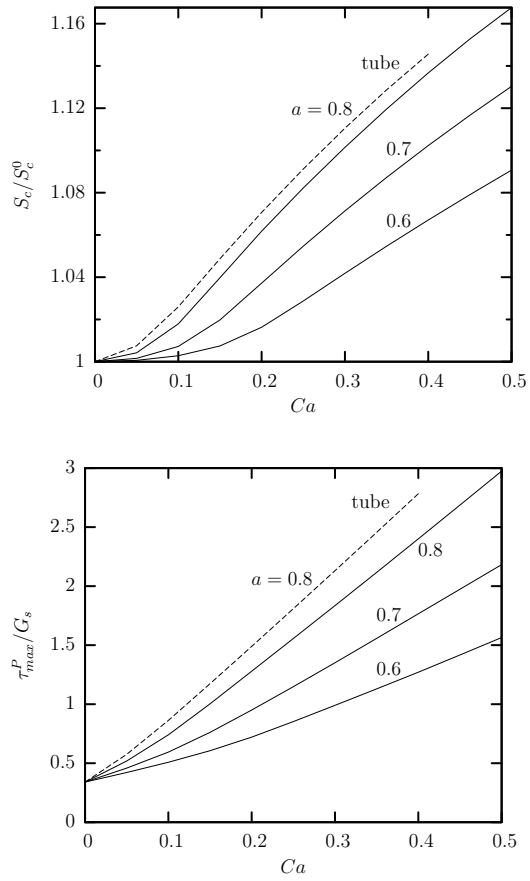

Figure 3.13: Steady-state capsule properties as a function of the capillary number Ca for a Skalak capsule with $C = 1$, $\alpha_p = 0.05$ and size $a = 0.6, 0.7, 0.8$. (a) Surface area of the capsule S_c at steady state (scaled with the surface area S_c^0 of the undisturbed spherical shape). (b) Maximum principal tension τ_{max}^P among the spectral discretization points on the membrane.

e.g. dimple, is developed in the capsule's lateral surface (i.e. between its upstream and downstream section). All these variables are not affected much by the capillary number for each of the three capsule sizes included in this figure. As the capsule size a increases, the smaller distance h between the capsule surface and the walls results in a slower capsule motion and in higher pressure drop.

3.4.1 Comparison with Flow in a Cylindrical Tube

As discuss previously in this section, owing to the nearly axisymmetric cross-section in the flow direction, small and moderate capsules in square channels should show dynamics similar to that in cylindrical tubes. In particular, similar (qualitative) behavior for the capsule's length L_x, width L_x, and downstream and upstream curvatures were found in earlier experimental and computational studies, e.g. [49, 51, 33]. For example, see figure 4 in the work by Lefebvre and Barthès-Biesel [33] who considered the steady-state properties of capsules with prestress $\alpha_p = 0, 0.025, 0.1$ and size $a/R = 0.8$ (where R is the tube radius). We note that figure 11 of the earlier study shows that in cylindrical tubes the pressure drop increases (almost) linearly with the capillary number Ca; this appears to contrast with our results presented in figure 3.14(b). This difference results from the different scales used for the pressure; in particular, the earlier study scaled the pressure based on membrane properties (i.e. G_s/R) while we scale the pressure based on flow properties (i.e. $\mu U/\ell_z$). Scaling the pressure as in our study, the results of Lefebvre and Barthès-Biesel [33] presented in their figure 11 show that the pressure drop is

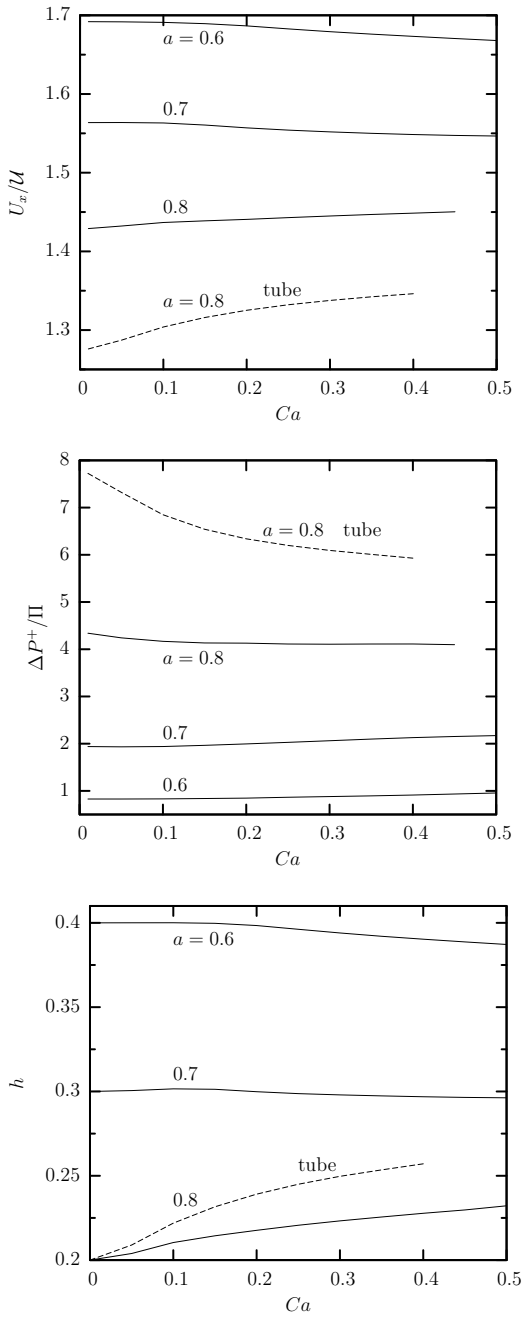

Figure 3.14: Steady-state capsule properties as a function of the capillary number Ca for a Skalak capsule with $C = 1$, $\alpha_p = 0.05$ and size $a = 0.6, 0.7, 0.8$. (a) Capsule velocity U_x. (b) Additional pressure difference ΔP^+. (c) Minimum distance h between the capsule surface and the channel's walls.

rather insensitive to the capillary number for moderate-size capsules as also found in our study.

The similarity of the channel and tube dynamics at moderate capsule sizes motivated us to make detailed comparisons of the two cases to identify clearly their similarities and possible differences. Since the earlier computational studies which considered capsule dynamics in cylindrical tubes [49, 33] did not report results for the prestress level used in this paper, we studied this problem for prestress $\alpha_p = 0.05$, capsule size $a = 0.8$ and several flow rates using our (three-dimensional) membrane algorithm. The spectral boundary element discretization of the tube wall was identical to that for the channel (i.e. we defined rows of four elements) while the tube's inlet and outlet were discretized into five elements each. For this system, the tube radius R is used as the length scale while all rest parameters are defined as for the channel problem reported in Chapter 2. Wherever possible, we have already included our results for tube dynamics in figures discussed earlier in this section (to reduce the number of additional figures).

Figure 3.15 shows the variation of the capsule lengths in channel and tube flow. In the channel, the capsule is less deformed (i.e. it is less extended along the flow direction and more extended laterally), for the same capillary number Ca, than in the tube. The smaller interfacial deformation in the channel results from the existence of the corners' area which permits flow of the surrounding flow and thus causes less deformation on the capsule. In a similar manner, the capsule in the tube shows larger downstream and upstream lengths, L_x^d and L_x^u, than in the channel. Excluding small capillary numbers (e.g. $Ca \leq 0.1$), figure 3.15 shows that a capsule

in a channel at a given capillary number has the same dimensions as in a tube flow but at a significantly lower capillary number. For example, the capsule lengths in the flow direction, L_x, L_x^d and L_x^u, are very similar for channel flow with $Ca = 0.35$ and tube flow with $Ca = 0.2$. The capsule width L_z in a channel with $Ca = 0.35$ corresponds to near $Ca = 0.13$ in a tube.

In contrast to the different interfacial deformation in channels and tubes, the capsule curvatures are very similar in these two system, as seen in figure 3.16. Thus, for capsules flowing in (straight) solid geometries, the interfacial curvatures are mostly determined by the capsule size and the capillary number, and not by the details of the cross-section of the solid geometry. It is of interest to note that, excluding small capillary numbers, our results show that the curvature at the downstream and upstream edges are rather insensitive to the capillary number for both solid systems (i.e. they are practically constant at moderate flow rates). On the other hand, the maximum profile curvature which occurs at the capsule rear end and close to the walls, increases fast with the capillary number as seen in figure 3.16(b).

The higher interfacial deformation in the tube flow results in a higher surface-area increase for the capsule and higher membrane tensions as seen in figure 3.13. However, now the correspondence in the flow rates for the two solid geometries are not as different as for the capsule lengths; for instance, very similar maximum principal tensions are obtained for $Ca = 0.35$ in the channel and $Ca = 0.3$ in the tube. The higher interfacial deformation in the tube flow also results in a higher gap between the capsule and the walls as shown in figure 3.14(c). However, the existence of the corners' area in the channel means that in this system the capsule blocks less

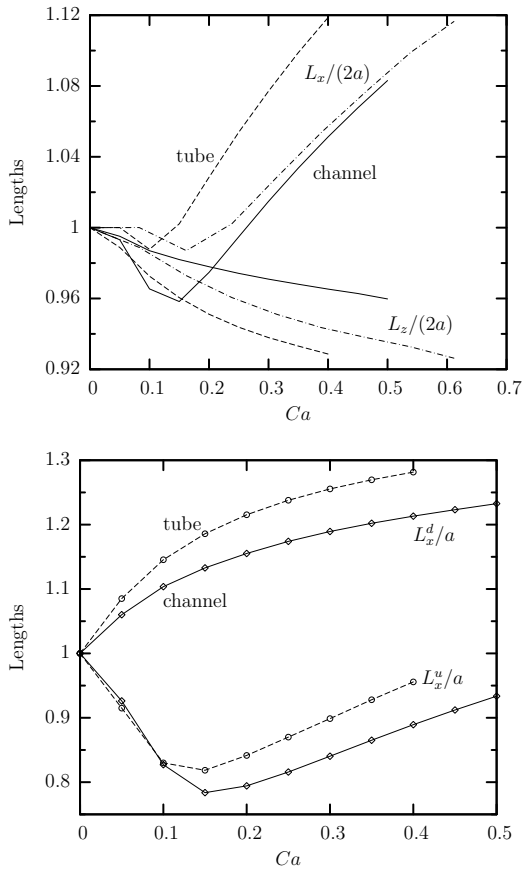

Figure 3.15: Steady-state capsule lengths as a function of the capillary number Ca for a Skalak capsule with $C = 1$, $\alpha_p = 0.05$ and size $a = 0.8$, in a square channel (——) and a cylindrical tube (– – –). (a) Capsule lengths $L_x/(2a)$ and $L_z/(2a)$. Also included are the predictions (– · –) of Eq.(2). (b) Capsule lengths L_x^d/a and L_x^u/a.

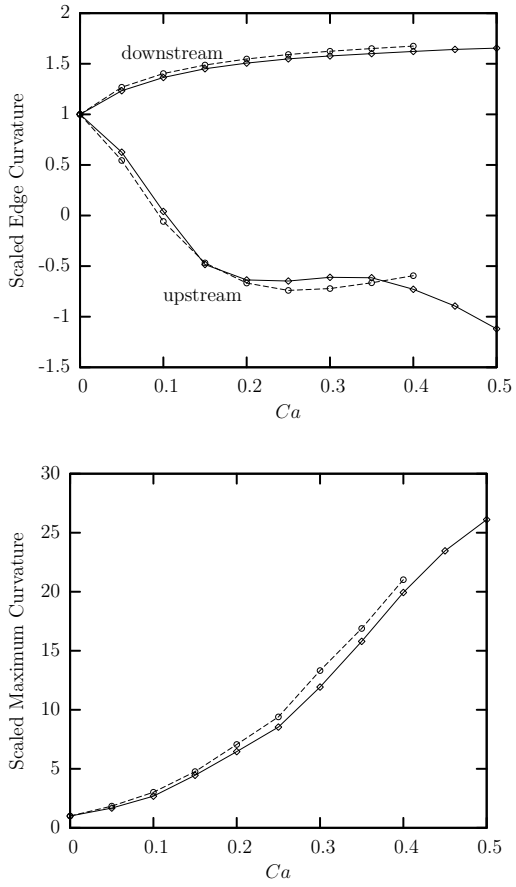

Figure 3.16: Steady-state capsule curvatures as a function of the capillary number Ca for a Skalak capsule with $C = 1$, $\alpha_p = 0.05$ and size $a = 0.8$, in a square channel (——) and a cylindrical tube (– – –). (a) Curvature at the downstream and upstream edges of the capsule (i.e. its intersections with the x-axis). (b) Maximum curvature along the capsule's $z = 0$ profile. All curvatures are scaled with the curvature of the undisturbed spherical shape.

the flow of the surrounding fluid. Thus in a tube, the same capsule causes a much higher pressure drop and travels with a smaller velocity than that in a channel as seen in figure 3.14(*a, b*).

Recently, Lefebvre *et al.* [34] proposed to let microcapsules flow in microfluidic cylindrical tubes and square channels as a method to determine the elastic properties of the membrane, including the shearing modulus, by comparing the capsule profiles from photos in these systems with computational results. Owing to unavailability of computational results in square channels, the authors utilized the results from their axisymmetric methodology (valid for cylindrical tubes) and proposed an approximate equation to relate the flow rates in tubes and square channels producing the same interfacial deformation,

$$Ca_{sq} \approx Ca_{cyl} \left(\frac{4 - \pi}{2\pi \bar{h}_{cyl}/R} + 1 \right) \tag{2}$$

where $\bar{h}_{cyl}$ is the mean thickness of the gap between the capsule interface and the tube wall. As the authors reported in the conclusion of their study, the approximate analysis is valid inasmuch as there is a clear lubrication film around the capsule, and thus it is restricted to a fairly narrow range of values of capsule sizes, probably between 0.9 and 1.1. It is of interest to note that owing to experimental difficulties, Lefebvre *et al.* [34] managed to test only sizes in the range $[1, 1.1]$ and for small capillary numbers. In particular, they used the neo-Hookean law (since the membrane tested showed strain-softening behavior) and capillary numbers $Ca \leq 0.02$. Under these conditions, the authors found that the approximate Eq.(2) can successfully predict the correspondence between channel and tube flow.

As shown in figure 3.15, the approximate analysis of Lefebvre *et al.* [34] predicts reasonably well the capsule length L_x in a square channel, and with higher error the capsule width L_z. (For this, we used our data for the capsule lengths as a function of the capillary number in a tube flow and determined the corresponding channel capillary number Ca_{sq} via Eq.(2) using the minimum gap h as the mean thickness of the gap $\bar{h}_{cyl}$.) Recall that, as seen in figure 3.16, the capsule curvatures are very similar in the two solid systems for the same capsule size and flow rate, and also practically independent of the capillary number for moderate flow rates. Therefore, we conclude that the approximate analysis of Lefebvre *et al.* can be used to relate capsule deformation in cylindrical tubes and square channels even for smaller capsule sizes (like $a = 0.8$) and for moderate capillary numbers, if one matches only the length L_x and the curvatures of the capsule in these two solid geometries.

Chapter 4

Motion of an Elastic Capsule in a Rectangular Microfluidic Channel

Rectangular microchannels are one of the most common type of channels encountered in microfluidic devices. Rectangular channels are the basis of many microfluidic devices with wide uses such as analytical and diagnostic devices, droplet generators and microreactors. Shelby *et al.* [54] used PDMS channels with rectangular constrictions of varying widths and 2 μm height to characterize the behavior of single cell under flow, in multicellular capillary blockages due to malaria infected cells. Antia, Herricks and Rathod [3] used rectangular microchannels of various dimensions to study cytoadherence of malaria infected erythrocytes. Dendukuri, Hatton and Doyle [11] used a microfluidic device based on a rectangular channel to synthesize amphiphilic, spherical and non-spherical polymeric micro-particles. For the synthesis of spherical micro-particles, a stepped height PDMS channel was used with dimensions of height = 16 μm and width = 40 μm in the T-junction and height = 75 μm and width = 200 μm downstream where the drop relaxes to a spherical shape. For plug shaped particles, the dimensions were height = 16 μm and width = 40 μm for both the T-junction and downstream region. Wedge-shaped particles

bearing segregated hydrophilic and hydrophobic sections were synthesized in a microfluidic channel using continuous flow lithography. Tice *et al.* [60] used a PDMS microchannel of rectangular cross-section for formation of droplets with multiple reagents. They also studied the mixing within the droplets as they travel through the channel with the aim of utilization as microreactors.

The above-mentioned studies are experimental studies and hence have limitations because of the small length scales involved. The very small magnitude of microfluidic systems makes the measurement of various parameters like pressure drop, capsule velocity, etc. very difficult [61]. Hence a good numerical model with the ability to predict such parameters can facilitate the design and use of such devices. In this chapter we study in detail the flow dynamics of capsules in rectangular microfluidic channels using our interfacial spectral boundary element algorithm for membranes. Because of the non-axisymmetric nature of the channel, capsule behavior in rectangular channel is much different than that in cylindrical and square channels. We study in detail the effects of parameters such as capsule size and capillary number on the capsule deformation and flow properties during capsule motion in a rectangular channel.

4.1 Problem Description

We consider an initially spherical Skalak capsule with scaled area-dilation modulus $C = 1$, flowing along the centerline of a straight rectangular microchannel with cross-sectional aspect ratio 2. The z-dimension ($2l_z$) of the channel is the shortest

dimension and the cross-sectional aspect ratio is 2. Three-dimensional views of the problem geometry are shown in figure 4.1. The capsule interior (fluid 1) and exterior (fluid 2) are Newtonian fluids, with viscosities $\lambda\mu$ and μ, and the same density. The capsule size is specified by its volume V or equivalently by the radius a of a sphere of volume $V = (4\pi/3)a^3$. Far from the capsule, the flow approaches the undisturbed flow, which for a rectangular channel is a steady unidirectional flow [65] given by equation (17). Assuming low-Reynolds-number flows, the governing equations in fluid 2 are Stokes equations and continuity. The associated boundary integral equation (11) has been described in Chapter 2. The numerical solution of the boundary integral equation is achieved by employing the spectral boundary element method for membranes, which has been described in detail in the Chapter 2. The surface discretization of the geometry is illustrated in figure 4.1. The surface discretization for the capsule is described in detail in Chapter 3. The spectral element discretization of the channel surface follows the capsules' center of mass. The channel surface in the capsule vicinity is divided into a row of one spectral element per channel side (i.e. a total of four elements) with half-size equal to l_z. The channel's inlet and outlet are discretized into one element each as shown in figure 4.1(a). The channel surface is divided into 4 rows of four elements each; the length of each row progressively increases with the distance from the capsule surface as seen in the figure 4.1(a). The channel surface (which formally should extend to infinity) has a half length l_x equal to 20 times the cross-sectional dimension l_z. For rectangular channels, the computations were performed with a discretization employing $N_E =$ 36 elements. In this study we mostly utilized $N_B = 12$ -14 basis points i.e. a total

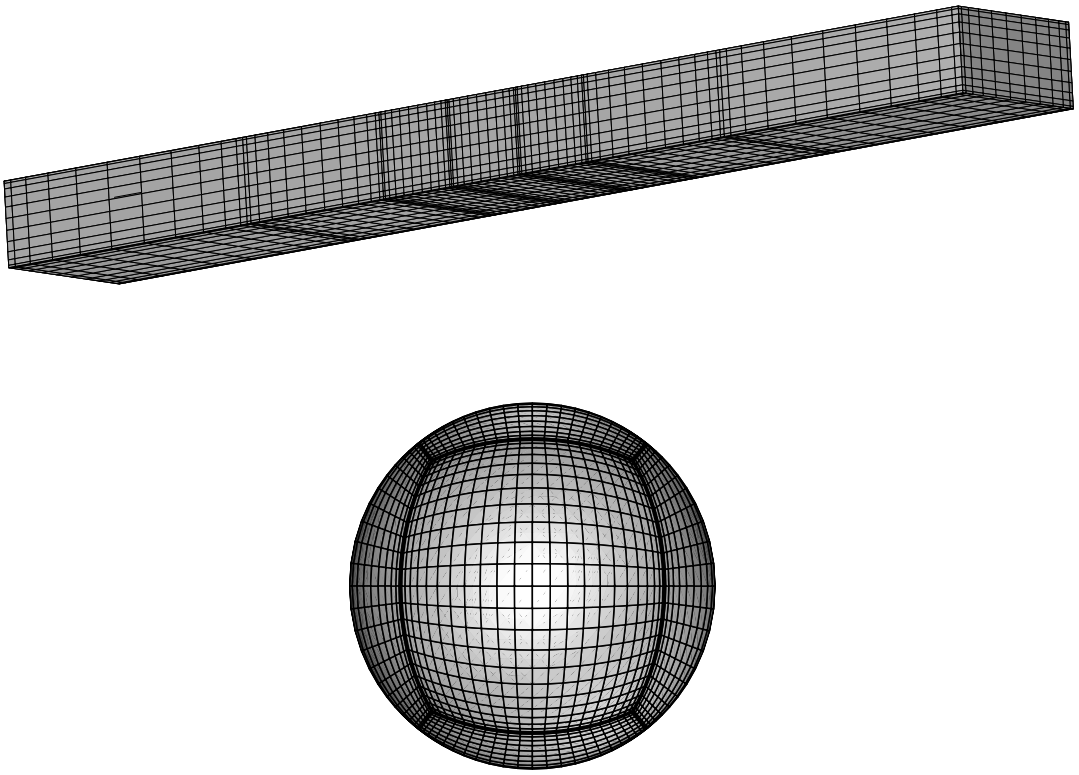

Figure 4.1: Spectral boundary element discretization of system surface:(a) solid surface of the channel along with the fluid surface at the channel end. (b) capsule surface.

number of spectral points for the entire geometry N = $N_E N_B^2$ = 5184-7056. The problem studied admits two symmetry planes, $y = 0$ and $z = 0$. Thus the memory requirements are reduced by a factor of 4^2, the computational time for the system matrices by a factor of 4 and the solution time via direct solvers of the linear systems by a factor of 4^3.

4.2 A Comparative Study of Capsule Motion in Square and Rectangular Channels

In this section, we conduct a comparative study of capsule deformation in a square and a rectangular channel in order to investigate how the non-axisymmetric geometry effects the capsule deformation and flow dynamics. This study is conducted for a Skalak capsule with $C = 1$, capsule size $a = 1.1$ and viscosity ratio $\lambda = 1$. The capillary number is $Ca = 0.1$ while the capsule is always over-inflated due to positive osmotic pressure by 5% (i.e. prestress $\alpha_p = 0.05$).

Figure 4.2 shows the steady-state shapes for a capsule moving along the centerline of a square and a rectangular channel. We observe that the capsule in the square channel is elongated compared to that in a rectangular channel in the axial direction. But along the lateral z-direction the capsule in the rectangular channel shows larger elongation. Figure 4.3 shows the steady-state profiles of the capsule along the $x = 0$, $y = 0$ and $z = 0$ planes for both square and rectangular channels. We see that the capsule in the square channel undergoes a large deformation in the $z = 0$ plane and shows a curvature change at the upstream end. But the capsule in

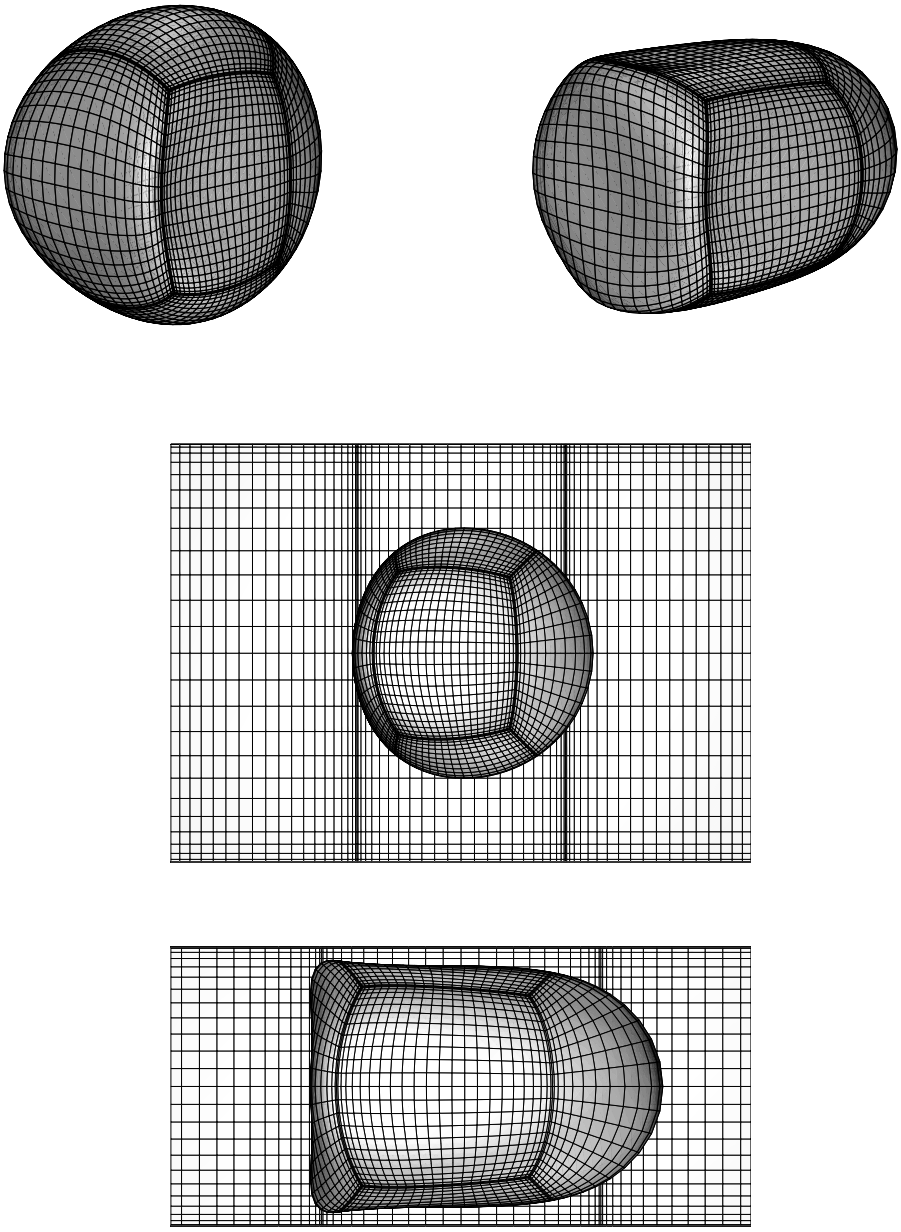

Figure 4.2: Steady-state capsule shape for a Skalak capsule with $C = 1$ moving along the centerline of a channel. The viscosity ratio $\lambda = 1$ and the capillary number $Ca = 0.1$. The capsule size $a = 1.1$. (a) Rectangular cross-section with aspect ratio 2. (b) Square cross-section.

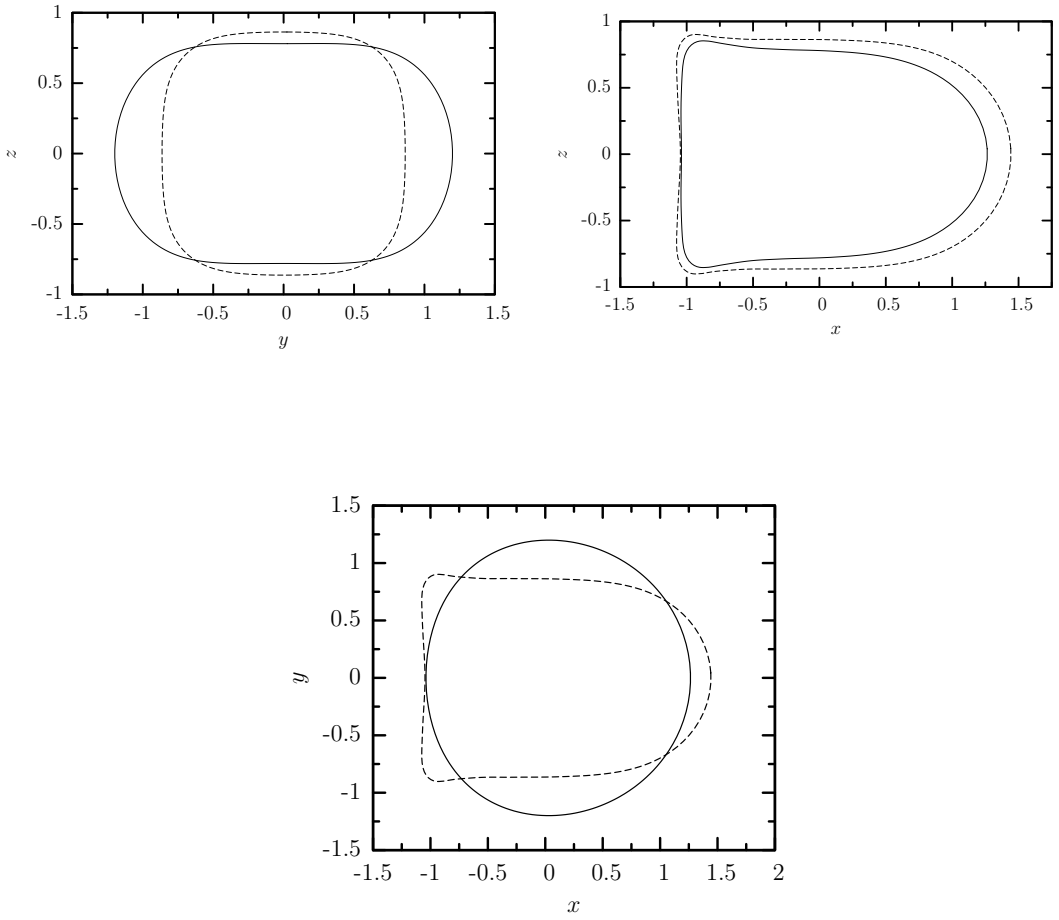

Figure 4.3: The steady-state profile of a capsule with size $a = 1.1$ moving along the centerline of a square and rectangular channel. The viscosity ratio is $\lambda = 1$ and the capillary number is $Ca = 0.1$. The capsule size is $a = 1.1$. (a) Capsule $x = 0$ profile. (b) Capsule $y = 0$ profile. (c) Capsule $z = 0$ profile. All profiles shown have centroid $\boldsymbol{x}_c = \mathbf{0}$. Rectangular channel: solid line; square channel: dashed line.

the rectangular channel shows only slight deformation in this plane. The upstream curvature deviates slightly from the spherical shape but remains convex unlike in the square channel where it becomes concave. In the $y = 0$ plane the deformation in both channels are of similar nature as seen in figure 4.3(b). For both cases the back curvature changes from convex and becomes concave. But here we observe that the capsule in the square channel undergoes a larger deformation and it is more elongated than the capsule in the rectangular channel. For the capsule flow in square channel the $z = 0$ and $y = 0$ profiles are identical but for the rectangular channel this is not true. The $x = 0$ profile is plotted in figure 4.3(c). In this plane the rectangular channel shows more elongation in the y-direction, which is expected since the channel dimension is greater in this direction. For the square channel the profile takes the shape of the channel and is a square with rounded edges.

In figure 4.4 we plot the transient evolution of the upstream and downstream edge curvature for a capsule moving along the centerline of a square and a rectangular channel. We see in figure 4.4(a) that the downstream curvature along capsule's $z = 0$ profile is greater for the rectangular channel but for both square and rectangular the edge curvature remains positive. But the upstream curvature for the square channel shows a change from positive to negative and assumes a negative curvature at the steady-state. The curvature along the $y = 0$ profile remains positive for both cases. In figure 4.5 we plot the transient evolution of the maximum and minimum profile curvature along the $z = 0$ and $y = 0$ profiles. We observe that for capsule in square channel both the profiles have similar curvature but for rectangular channel this is not true. The magnitude of the maximum and minimum curvature of the

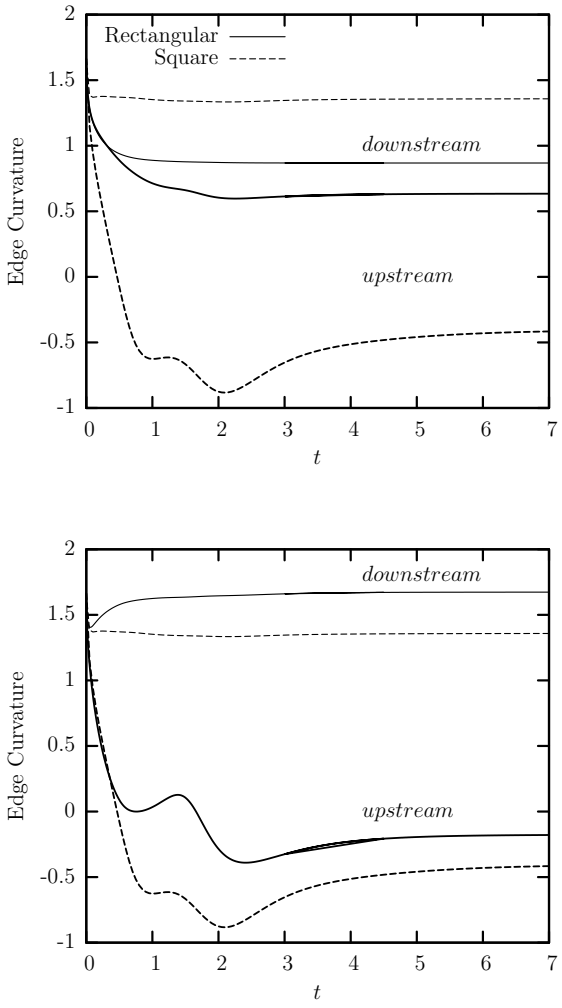

Figure 4.4: Time evolution of the capsule curvature at the upstream and downstream edges of the capsule (i.e. its intersection with the x-axis). The capsule size is $a = 1.1$ and capillary number is $Ca = 0.1$. (a) Curvature determined along capsule's $z = 0$ profile. (b) Curvature determined along capsule's $y = 0$ profile.

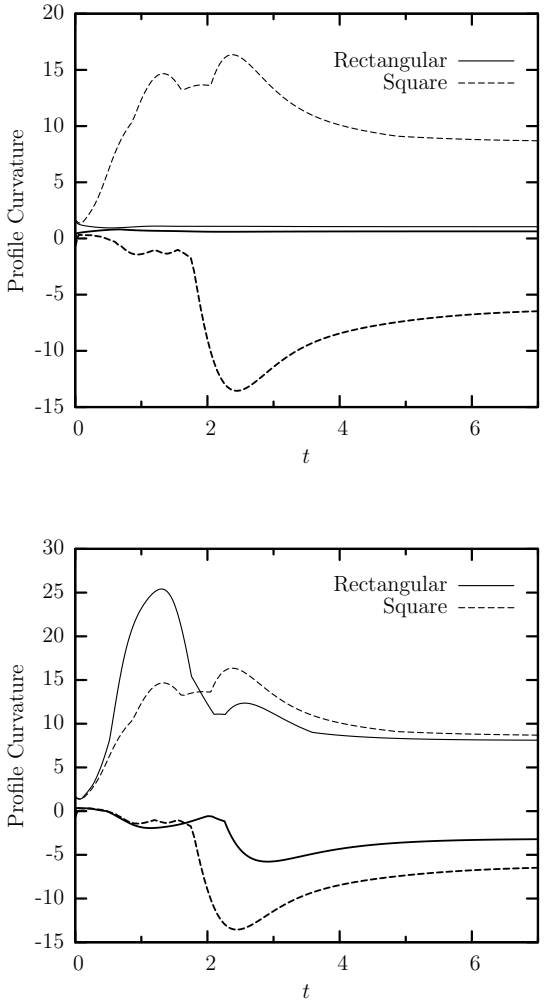

Figure 4.5: Time evolution of the maximum and minimum profile curvature for a Skalak capsule with $C = 1$, size $a = 1.1$, and $\lambda = 1$ moving along the centerline of a rectangular channel with cross-sectional aspect ratio 2 and a square channel. The capillary number is $Ca = 0.1$. (a) Curvature determined along capsule's $z = 0$ profile. (b) Curvature determined along capsule's $y = 0$ profile.

capsule along the $y = 0$ profile for a rectangular channel is similar to that in square channel. However, the maximum and minimum curvature along the $z = 0$ profile is nearly the same for the rectangular channel which is much different from the square channel. This is due to the larger l_y in the case of the rectangular channel.

Figure 4.6(a) shows the time evolution of the capsule dimensions for a capsule moving along the centerline of a square and a rectangular channel. We see in figure 4.6(a) that in the x-direction, the capsule in the square channel undergoes greater elongation. For a capsule in the square channel, the lengths in the y and z (L_y and L_z) directions are the same. But for a capsule in a rectangular channel, L_z decreases with time to attain steady- state while L_y increases. Figure 4.6(b) shows the length of the upstream (L_x^{neg}) and downstream (L_x^{pos}) edge from the capsule centroid. We see that both L_x^{pos} and L_x^{neg} are greater for a capsule in the square channel. Also, L_x^{pos} shows a larger difference between square and rectangular channel.

In figure 4.7(a) we see the effects of channel geometry on the minimum distance between the capsule surface and channel's walls h_{min}. As expected, h_{min} is greater for a rectangular channel than the square channel. This is because of the greater deformation along the z-direction of the capsule in a rectangular channel resulting in lower capsule height. The gap h_{min} for the rectangular channel is 50 % greater than that for the square channel. This also results in a significant decrease in the excess pressure drop which drops from a steady-state value of around 20 units for a square channel to 5 units for the rectangular channel as seen in the figure 4.7(b). The capsule velocity is also higher in the rectangular channel as seen in figure 4.7(c).

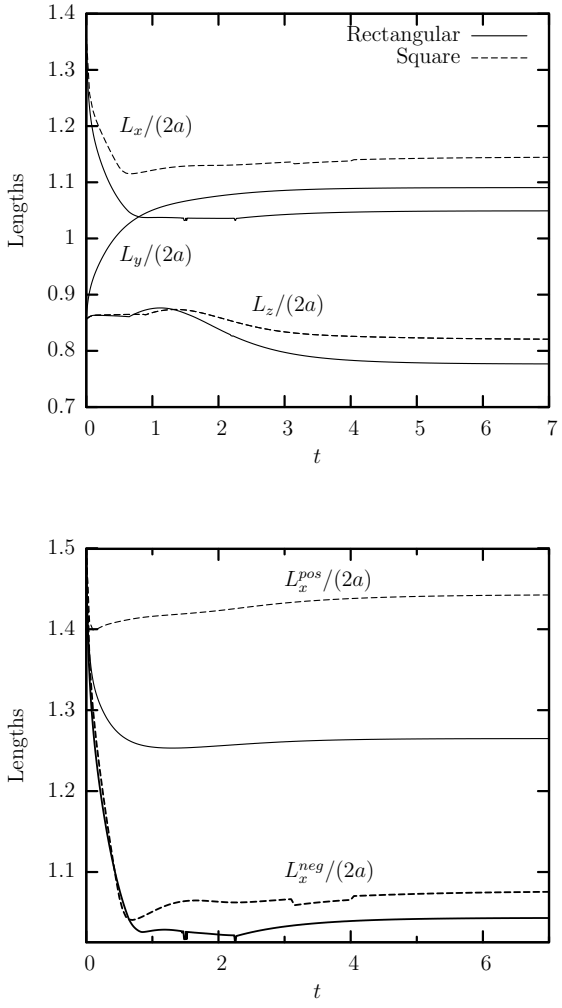

Figure 4.6: Time evolution of the capsule dimensions for a capsule moving along the centerline of a rectangular channel with cross-sectional aspect ratio 2 and a square channel. The capsule size is $a = 1.1$ while the viscosity ratio is $\lambda = 1$ and the capillary number is $Ca = 0.1$. (a) Capsule lengths $L_x/(2a)$, $L_y/(2a)$, and $L_z/(2a)$. (b) Capsule lengths $L_x^{pos}/(2a)$ and $L_x^{neg}/(2a)$.

The velocity in a rectangular channel is almost 15 % higher than that in the square channel.

4.3 Effects of Capsule Size

In this section we investigate how the capsule deformation and flow dynamics is affected by the capsule size by studying capsules of sizes $a = 0.2$ to $a = 1.1$. The viscosity ratio is always $\lambda = 1$ and capillary number is $Ca = 0.2$. We apply a prestress $\alpha_p = 5$ %.

In figure 4.8 we see the steady-state profiles of capsules of varying sizes along the $x = 0$, $y = 0$ and $z = 0$ planes. We see that the smaller capsules do not deform significantly and retain a profile close to the initially spherical one. But the larger capsules deform significantly undergoing significant elongation in the x and y directions. In the $x = 0$ plane, as seen in figure 4.8(a), we notice that the larger capsules elongates in the y-direction and attain a shape close to the cross-sectional rectangular shape. In figure 4.8(b) we plot the steady-state profile in the $y = 0$ plane. Here we see a significant effect of the increasing capsule size and for the larger capsules studied, the upstream tip shows a curvature change and buckles to become concave. The profile in the $z = 0$ plane is plotted in figure 4.8(c). In the figure 4.9 we plot the steady-state capsule curvatures along $y = 0$ and $z = 0$ profiles at the upstream and downstream tips as a function of the capsule size. We see that the value of curvature decreases with increasing size for all cases except the upstream curvature along the $y = 0$ profile. The negative upstream curvature along

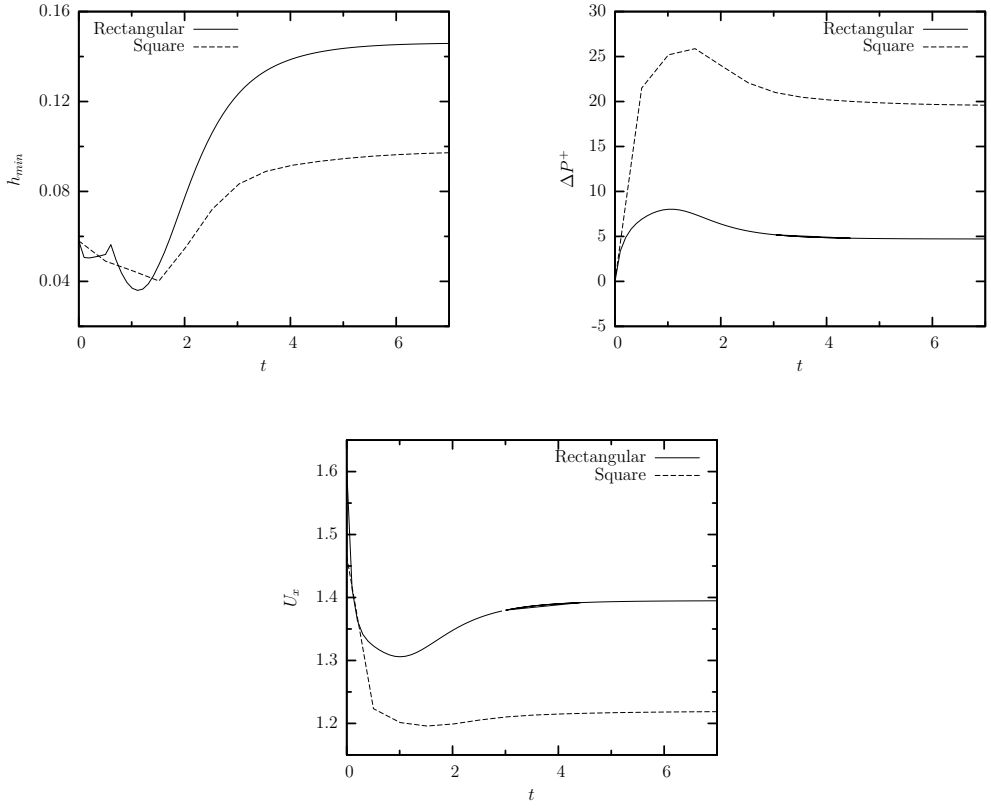

Figure 4.7: Time evolution of capsule properties for a Skalak capsule with $C = 1$ and capsule size $a = 1.1$ moving along the centerline of a rectangular channel with cross-sectional aspect ratio 2 and a square channel. The viscosity ratio is $\lambda = 1$ and the capillary number is $Ca = 0.1$. (a) Minimum distance h_{min} between the capsule surface and the channel's walls. (b) Additional pressure difference ΔP^+ owing to the capsule presence. (c) Capsule velocity U_x.

the $y = 0$ profile increases with increasing capsule size and becomes positive for the larger capsules. This is because of the dimpling at the upstream tip which is seen in figure 4.8(b).

The time evolution of the scaled capsule lengths in the axial and lateral directions are plotted in figure 4.10. We see that for smaller capsules, the variation in axial and lateral lengths is monotonous. The capsule length L_x and its depth L_z decreases while the capsule width L_y increases. But for larger capsules the transient evolution is non- monotonous. The axial length L_x first decreases and then increases to attain steady state. For the largest capsule with size $a = 0.9$, L_x is greater than the initial length. L_y also shows a non-monotonous behavior and first increases and then decreases to attain steady state. The steady-state dimensions of the capsule as a function of capsule size are plotted in figure 4.11. We see that L_x decreases with increasing capsule size for smaller capsules but for capsules larger than $a = 0.9$ we observe an increase in L_x. Both L_y and L_z change monotonically with increasing capsule size. L_y increases while L_z decreases as the capsule size increases. The smaller channel dimension along the z-direction restricts the capsule deformation in this direction resulting in smaller L_z.

In figure 4.12(a), we see the transient evolution of the capsule velocity in the axial direction for capsules of different sizes. The capsule velocity decreases with increasing capsule size. Figure 4.12(b) shows the time evolution of the additional pressure drop due to the presence of the capsule for capsules of varying sizes. For the smaller capsule the pressure drop increases and attains steady state but for the larger capsule it first increases and then decreases. As the capsule size increases, the

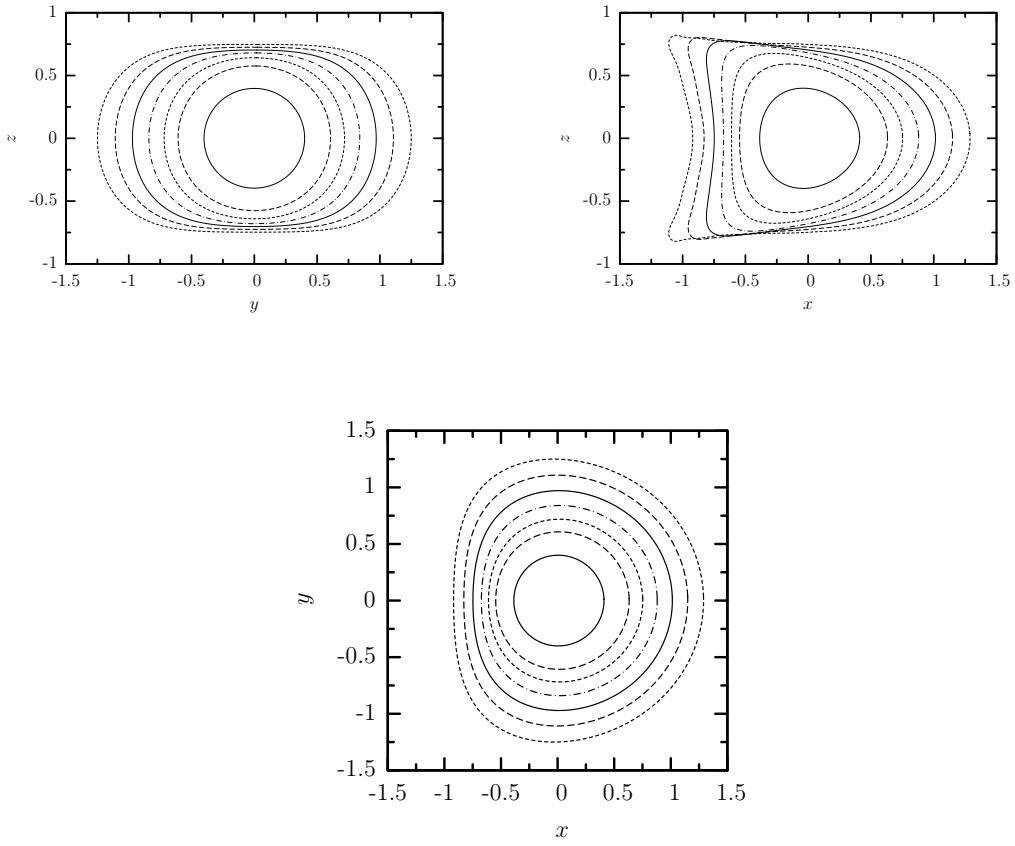

Figure 4.8: The steady-state profile of a capsule moving along the centerline of a rectangular channel for capsule size $a = 0.4, 0.5, \ldots, 0.9$. The viscosity ratio is $\lambda = 1$ and the capillary number is $Ca = 0.2$. (a) Capsule $y = 0$ profile. (b) Capsule $y = 0$ profile. (c) Capsule $z = 0$ profile. All profiles shown have centroid $\boldsymbol{x_c} = \mathbf{0}$.

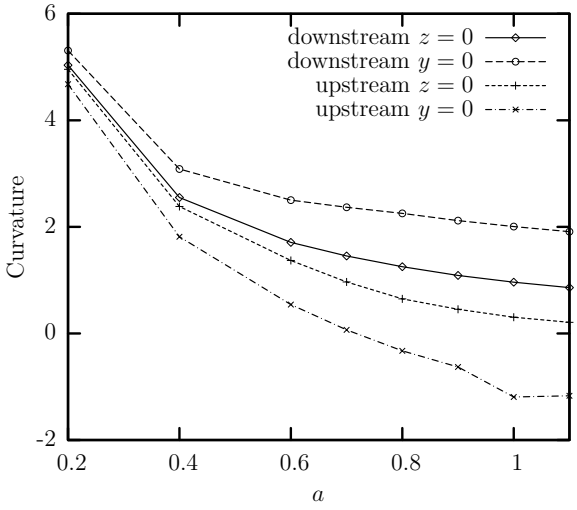

Figure 4.9: Steady-state capsule curvature at the downstream and upstream edges (i.e. capsule intersection with the x-axis) as a function of the capsule's size a for a Skalak capsule with $C = 1$, $\alpha_p = 0.05$ and capillary number Ca= 0.2, moving along the centerline of a rectangular channel. The curvature is determined along the capsule's $z = 0$ profile and $y = 0$ profile.

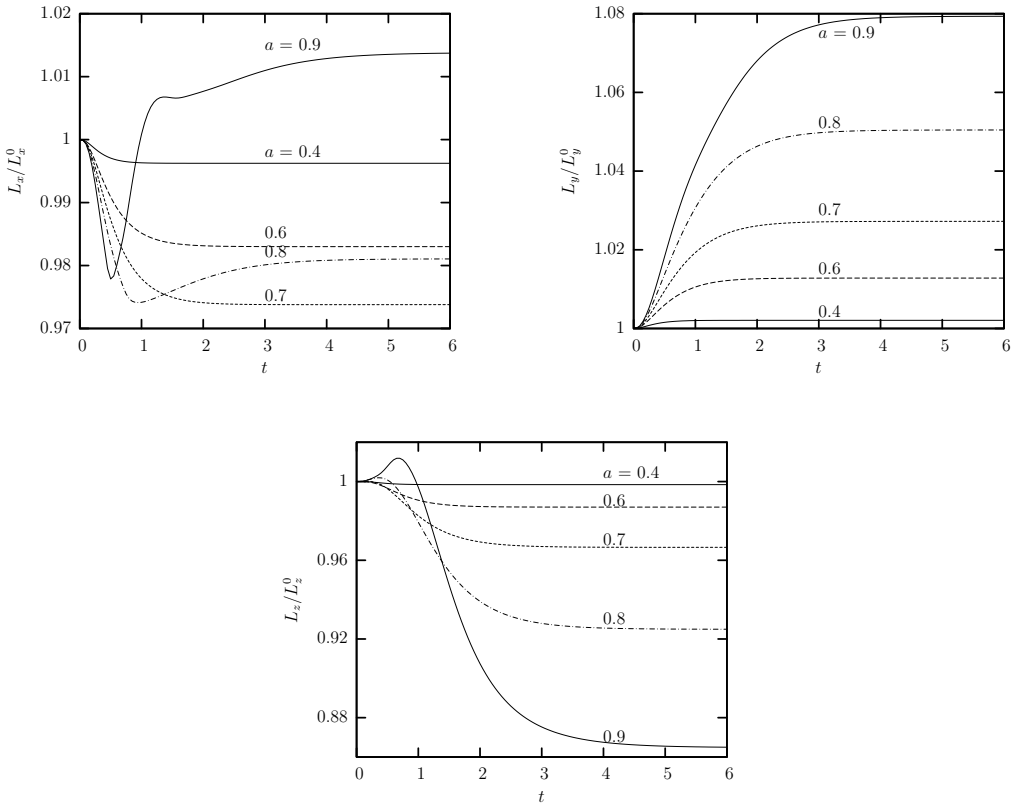

Figure 4.10: Time evolution of the actual capsule dimensions in x, y and z directions for a capsule moving along the centerline of a rectangular channel with aspect ratio 2 for capsule sizes $a = 0.4, 0.5, \ldots, 0.9$. The viscosity ratio is $\lambda = 1$ and the capillary number is $Ca = 0.2$. (a) Capsule length along x-axis $L_x/(2a)$. (b) Capsule length along y-axis $L_y/(2a)$. (c) Capsule length along z-axis $L_z/(2a)$.

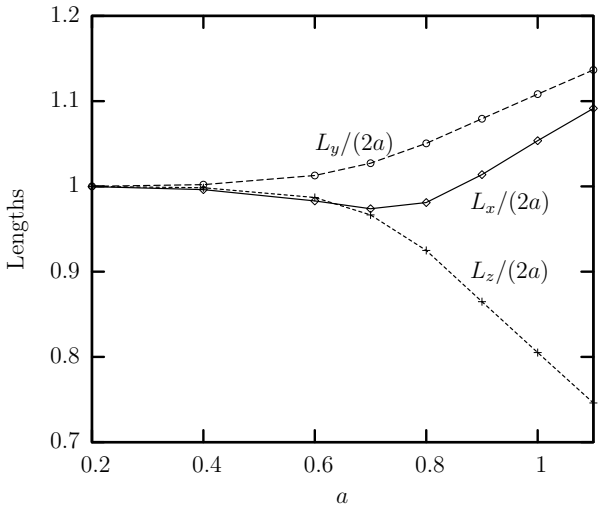

Figure 4.11: Steady-state capsule lengths $L_x/(2a)$, $L_y/(2a)$, and $L_z/(2a)$ as a function of capsule size for a capsule moving along the centerline of a rectangular channel with aspect ratio 2. The viscosity ratio is $\lambda = 1$ and the capillary number is $Ca = 0.2$.

excess pressure drop increases as expected due to greater blockage by the capsule. Figure 4.12(c) shows the effect of increasing capsule size on the minimum distance h_{min} between the capsule surface and the channel's walls. The gap h_{min} decreases with increasing capsule size. The transient evolution is again monotonous for smaller capsules. But for larger capsules, we see that h_{min} first decreases and then increases to attain steady state. Another effect of increasing capsule size is on the time taken to reach steady state. We see in figure 4.12 that as the capsule size increases the time required for capsule to reach steady state also increases. Figure 4.14 shows the steady-state capsule properties as a function of capsule size.

The transient evolution of maximum and minimum principal tensions for capsules of different sizes is plotted in figure 4.13. The larger capsules show non-monotonous behavior and the maximum principal tension first increases and then decreases to attain steady state while the minimum tension first decreases and then increases to reach steady state. For smaller capsules, the maximum tension increases and minimum tension decreases to attain steady state. Figure 4.15 shows the steady-state principal tensions as a function of capsule size. We observe that the steady-state value of maximum principal tension increases with increasing capsule size while the minimum principal tension decreases with increasing capsule size.

In figure 4.16 we plot the transient and steady-state scaled capsule surface area for capsules of varying sizes. We notice that the scaled surface area increases with increasing capsule size owing to larger deformation.

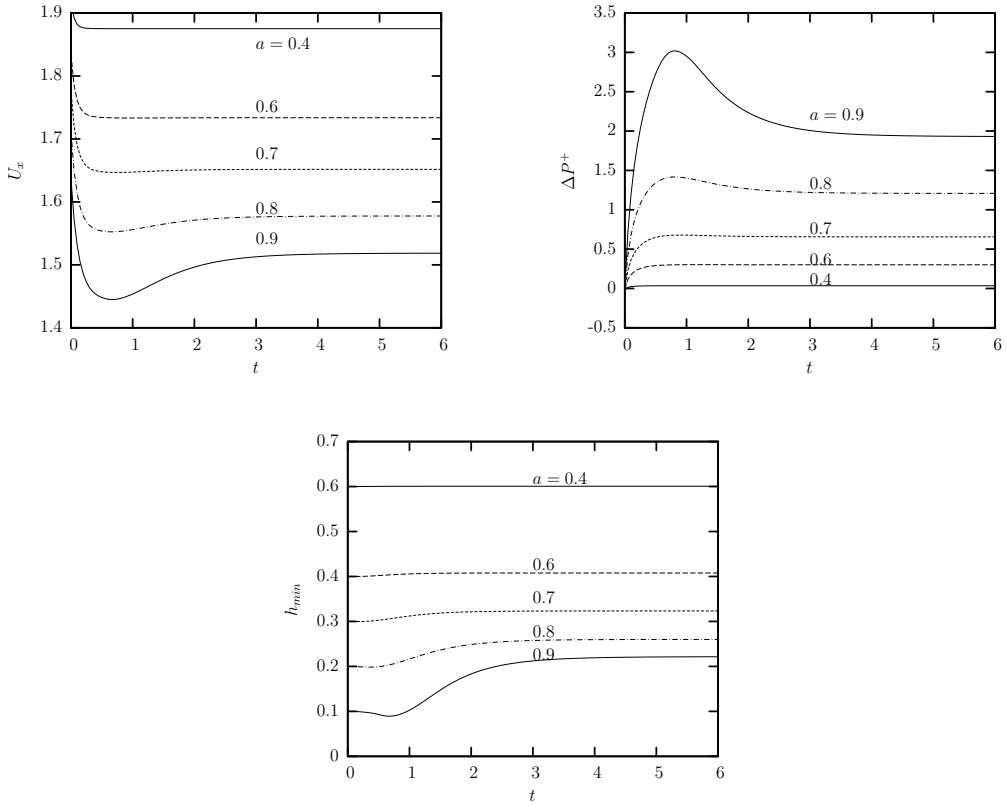

Figure 4.12: Time evolution of capsule properties for a Skalak capsule with $C = 1$, capillary number $Ca = 0.2$ and $\lambda = 1$ moving along the centerline of a rectangular channel with aspect ratio 2 for capsule size $a = 0.4, 0.5, \ldots, 0.9$.(a) Capsule velocity U_x. (b) Additional pressure drop ΔP^+ owing to the capsule presence. (c) Minimum distance h_{min} between the capsule surface and the channel's walls.

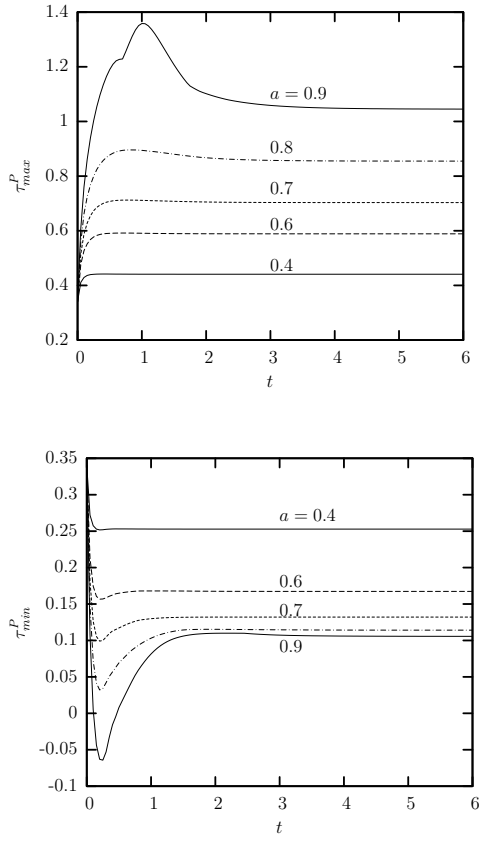

Figure 4.13: Time evolution of the principal tensions among the spectral discretization points on the membrane for a Skalak capsule with $C = 1$ and $\lambda = 1$ for varying capsule size $a = 0.4, 0.5, \ldots, 0.9$. The capillary number is $Ca = 0.2$. (a) Maximum principal tension τ^P_{max}. (b) Minimum principal tension τ^P_{min}.

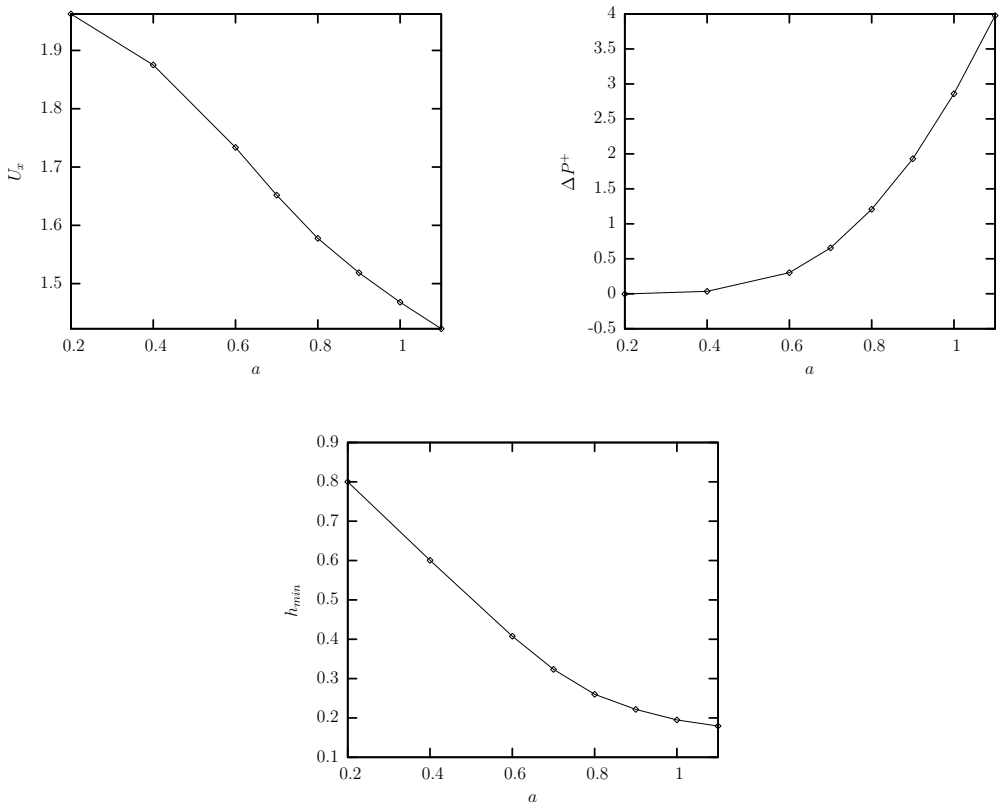

Figure 4.14: Steady-state capsule properties for a Skalak capsule with $C = 1$, capillary number $Ca = 0.2$ and $\lambda = 1$ moving along the centerline of a rectangular channel with aspect ratio 2 for varying capsule size $a = 0.2, 0.4, \ldots, 1.1$. (a) Capsule velocity U_x. (b) Additional pressure drop ΔP^+ owing to the capsule presence. (c) Minimum distance h_{min} between the capsule surface and the channel's walls.

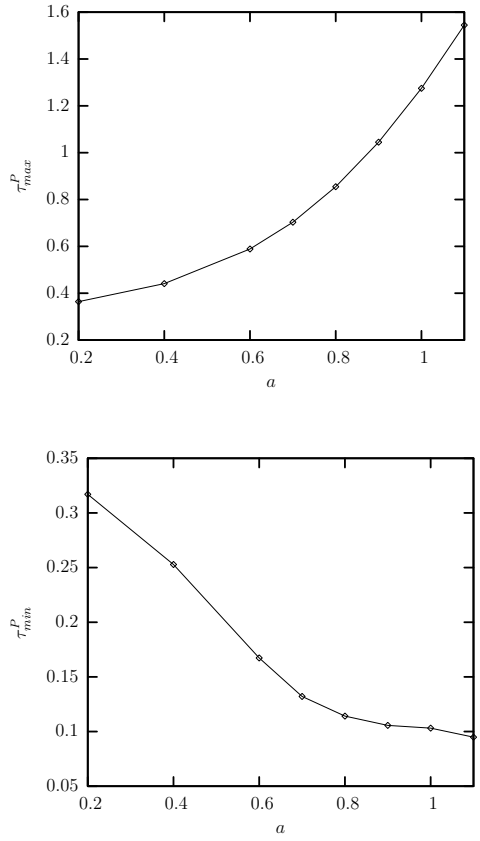

Figure 4.15: Steady-state principal tensions among the spectral discretization points on the membrane as a function of the capillary number Ca for a Skalak capsule with $C = 1$ and capsule size $a = 0.2, 0.4, \ldots, 1.1$.The capillary number is $Ca = 0.2$. (a) Minimum principal tension τ^P_{min}. (b) Maximum principal tension τ^P_{max}.

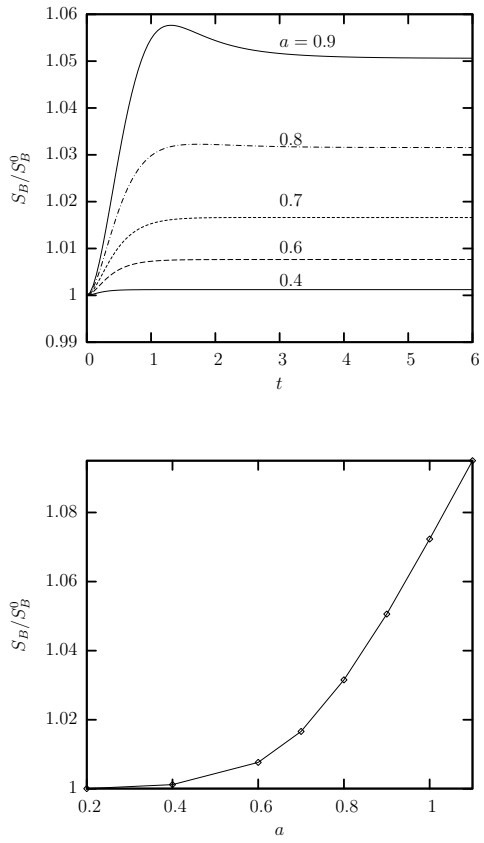

Figure 4.16: Surface area of a capsule moving along the centerline of a rectangular channel with aspect ratio 2. for viscosity ratio $\lambda = 1$ and capillary number $Ca = 0.2$. The capsule size varies from is $a = 0.4, 0.5, \ldots, 0.9$. (a) Time evolution of the scaled surface area of the capsule. (b) Steady-state scaled surface area of the capsule as a function of the capsule's size a.

4.4 Effects of Capillary Number

In this section we investigate the effects of capillary number on the capsule deformation and flow dynamics. For this study, we use a Skalak capsule with $C = 1$, prestress $\alpha_p = 5\%$ and size $a = 0.9$. The viscosity ratio s $\lambda = 1$. The range of capillary number studied is from $Ca = 0.05$ to $Ca = 0.3$.

In figure 4.17, we see the steady-state capsule profile along the $x = 0$, $y = 0$ and $z = 0$ planes. Figure 4.17(a) shows the capsule profile along the $x = 0$ plane. We notice that the capsule assumes a shape close to the cross-sectional rectangular shape in this plane. In figure 4.17(c) we observe that the profiles along the $z = 0$ plane show very slight variation with increasing Ca. The noticeable change in the profile for this plane is at the upstream edge, which becomes flatter with increasing capillary number. In the $y = 0$ plane, seen in figure 4.17(b), there is a significant elongation of the capsule and the profile shows significant changes with increasing capillary number. The upstream curvature deviates from the initial spherical shape as Ca is increased and for $Ca = 0.2$ the upstream edge buckles and becomes concave. Figure 4.18 shows the steady-state shapes for varying capillary number. Here we see that as the capillary number increases the upstream edge buckles and the curvature change increases. The dimple at the upstream edge has been noticed previously for droplet deformation between parallel plates [22]. Griggs, Zinchenko and Davis [22] found that droplets moving along the centerline between parallel plates attain a steady-state profile with a dimpled upstream edge. For a droplet of size $a = 0.8$, this buckling was observed for capillary number $Ca > 0.7$. The upstream and

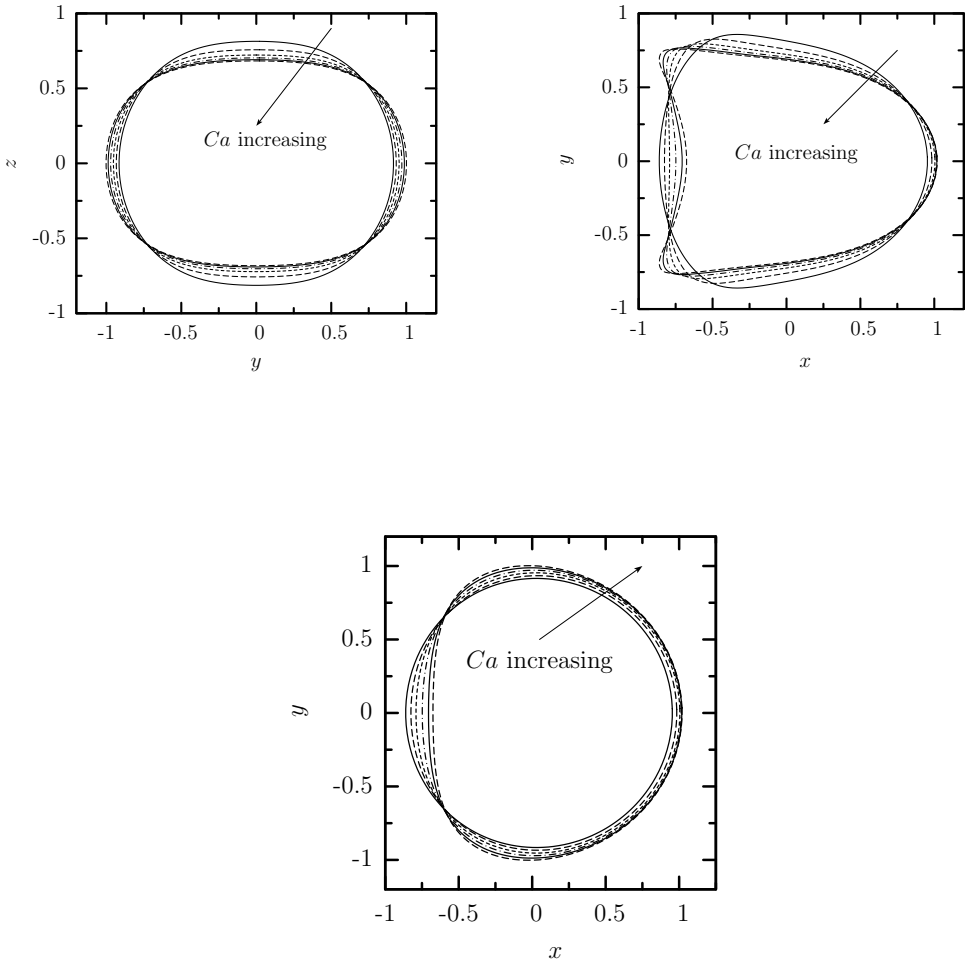

Figure 4.17: The steady-state profile of a Skalak capsule with $C = 1$ moving along the centerline of a rectangular channel for capillary number $Ca = 0.05$, 0.1, 0.15, 0.2, 0.25, 0.3. The viscosity ratio is $\lambda = 1$ and the capsule size is a= 0.9. (a) Capsule $z = 0$ profile. (b) Capsule $y = 0$ profile. (c) Capsule $x = 0$ profile. All profiles shown have centroid $\boldsymbol{x_c} = \mathbf{0}$.

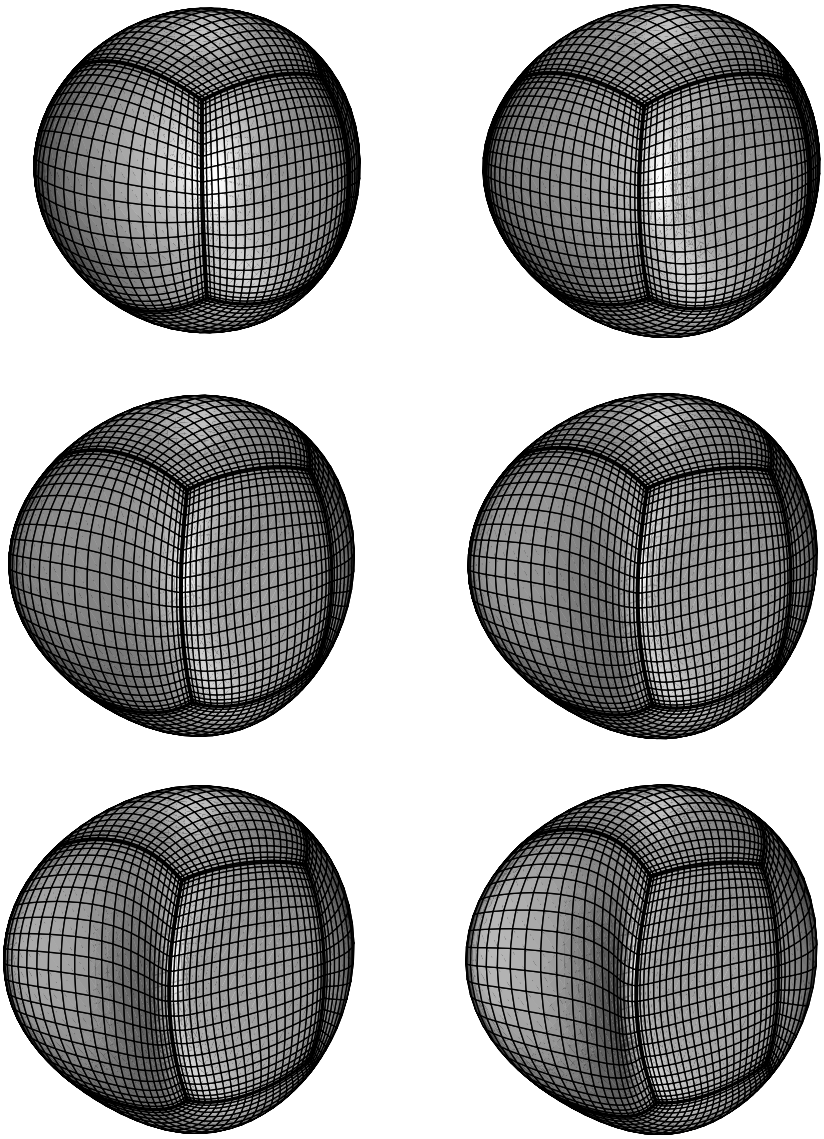

Figure 4.18: Steady-state capsule shape for a Skalak capsule with $C = 1$, capsule size $a = 0.9$, and viscosity ratio $\lambda = 1$ moving along the centerline of a channel for capillary number $Ca =$ (a) 0.05 (b) 0.1 (c) 0.15 (d) 0.2 (e) 0.25 (f) 0.3.

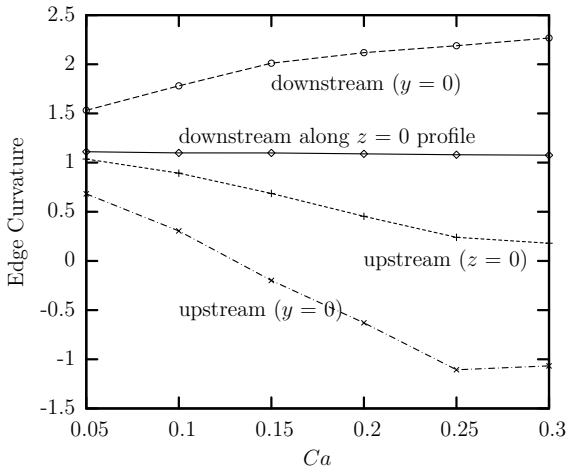

Figure 4.19: Steady-state capsule curvature at the downstream and upstream edges (i.e. capsule intersection with the x-axis) as a function of the capillary number Ca for a Skalak capsule with $C = 1$, $\alpha_p = 0.05$ and capsule size a= 0.9 moving along the centerline of a rectangular channel. The curvatures are determined along the capsule's $z = 0$ profile and $y = 0$ profile.

downstream steady-state edge curvatures are plotted in figure 4.19 as a function of capillary number. We see that the curvature along the $y = 0$ profile increases with capillary number for both upstream and downstream edges. The upstream edge curvature changes from positive to negative with increasing capillary number due to the buckling at the upstream edge. The curvature along the $z = 0$ profile decreases with increasing capillary number for the upstream edge. For the downstream edge, the $z = 0$ curvature does not show significant variation with capillary number and is almost constant.

Figure 4.20 shows the time evolution of the scaled capsule lengths in the axial

and lateral directions for varying capillary numbers. L_x initially decreases and then increases to attain steady state. L_y increases monotonically to attain a steady state value greater than the initial dimension. For lower capillary numbers, L_z decreases monotonically to attain steady state but for larger capillary numbers we observe a slight increase initially before decreasing to attain steady state. Figure 4.21 shows the variation in steady-state capsule dimensions as a function of the capillary number. We see in figure 4.21(a) that L_y increases and L_z decreases with increasing capillary number. L_x decreases slightly with increasing capillary number at lower capillary number but for $Ca > 0.15$, L_x increases with increasing capillary number. Figure 4.21(b) shows the steady-state axial length of the upstream and downstream capsule tips from the capsule centroid as a function of capillary number. We see that L_x^{pos} increases with increasing capillary number but L_x^{neg} initially decreases and then increases with increasing capillary number.

Next, we plot the transient and steady-state capsule properties for varying capillary number. Figure 4.22(a) shows the time evolution of the capsule velocity for several flow-rates. The capsule velocity decreases initially and then increases to attain steady state. The capsule velocity increases with increasing capillary number. The higher deformation at larger Ca results in greater capsule-wall gap shown in figure 4.22(c) resulting in an increase in the capsule velocity. Figure 4.22(b) shows the transient evolution of the additional pressure drop due to the presence of the capsule. The pressure drop initially increases and then decreases to attain steady state. The pressure drop also decreases with increasing capillary number. This is due to the greater deformation which results in smaller blockage by the capsule. The time

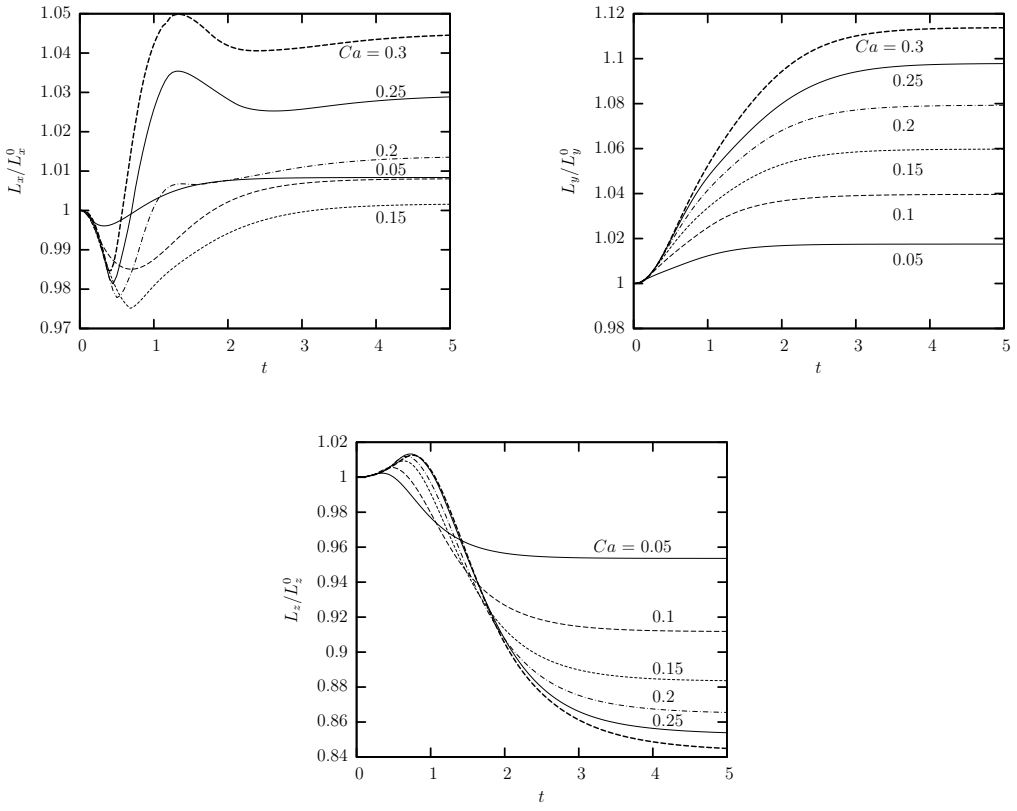

Figure 4.20: Time evolution of capsule dimensions in x, y and z directions for a capsule moving along the centerline of a rectangular channel with aspect ratio 2 for varying capillary number $Ca = 0.05$, 0.1, 0.15, 0.2, 0.25, 0.3. The viscosity ratio is $\lambda = 1$ and the capsule size is $a = 0.9$. (a) Capsule length along x-axis $L_x/(2a)$. (b) Capsule length along y-axis $L_y/(2a)$. (c) Capsule length along z-axis $L_z/(2a)$.

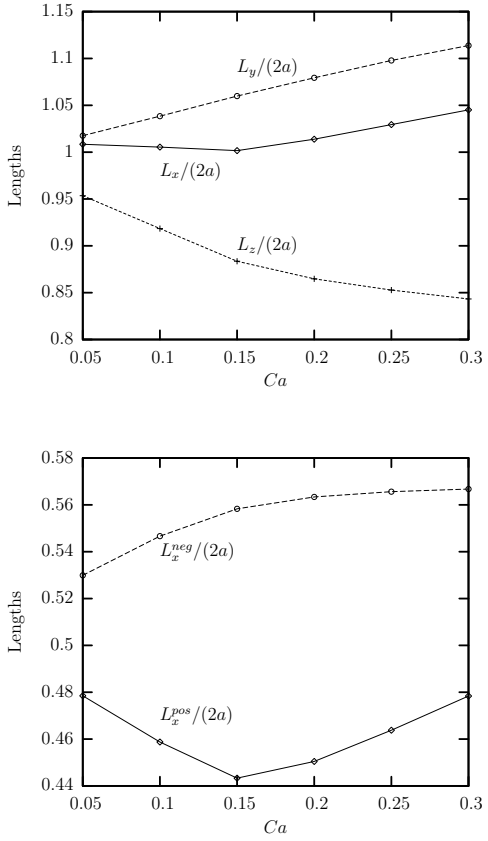

Figure 4.21: Steady-state capsule dimensions for a Skalak capsule with $C = 1$ moving along the centerline of a rectangular channel with aspect ratio 2 as a function of capillary number Ca. The capsule size is $a = 0.9$. (a) Capsule lengths $L_x/(2a)$, $L_y/(2a)$, and $L_z/(2a)$. (b) Capsule lengths $L_x^{pos}/(2a)$ and $L_x^{neg}/(2a)$.

evolution of the minimum distance between the capsule surface and the channel's walls h_{min} is shown in figure 4.22(c). We see that h_{min} increases significantly as Ca increases. As the Ca increases, the larger deformation results in a greater h_{min}. The steady-state capsule properties are plotted in figure 4.23.

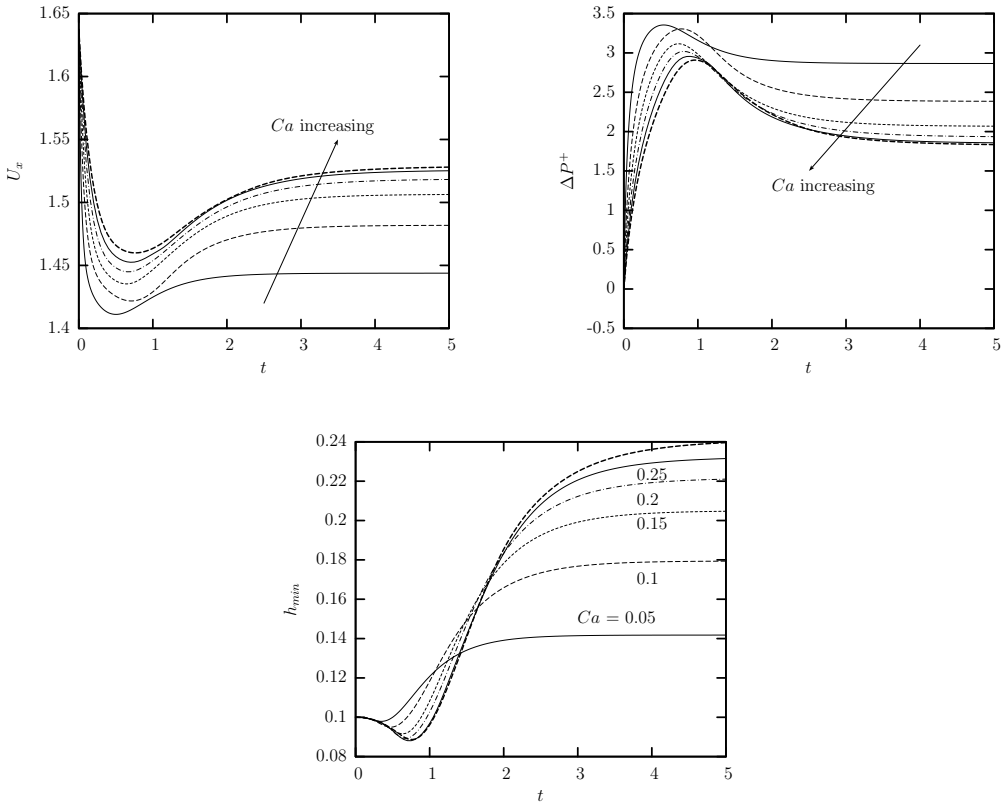

Figure 4.22: Time evolution of capsule properties for a Skalak capsule with $C = 1$, capsule size $a = 0.9$ and $\lambda = 1$ moving along the centerline of a rectangular channel with aspect ratio 2 for varying capillary number $Ca = 0.05$, 0.1, 0.15, 0.2, 0.25, 0.3. (a) Capsule velocity U_x. (b) Additional pressure drop ΔP^+ owing to the capsule presence. (c) Minimum distance h_{min} between the capsule surface and the channel's walls.

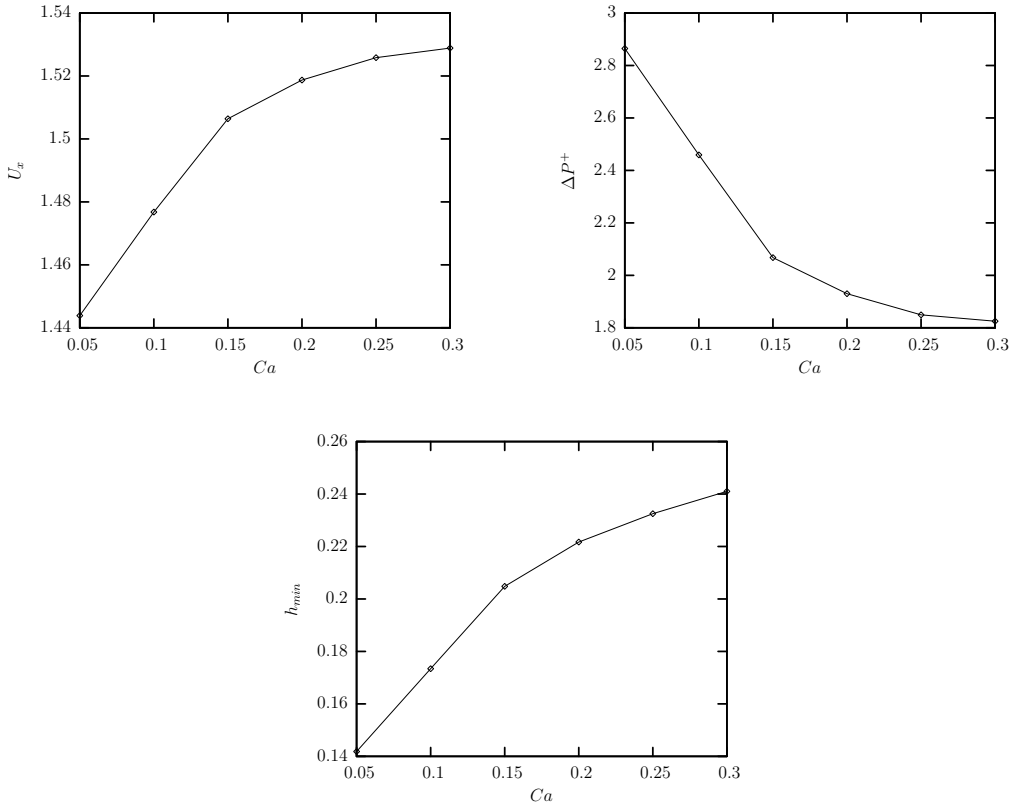

Figure 4.23: Steady-state capsule properties for a Skalak capsule with $C = 1$, size $a = 0.9$ and $\lambda = 1$ moving along the centerline of a rectangular channel with aspect ratio 2 for varying capillary number $Ca = 0.05$, 0.1, 0.15, 0.2, 0.25, 0.3. (a) Capsule velocity U_x. (b) Additional pressure drop ΔP^+ owing to the capsule presence. (c) Minimum distance h_{min} between the capsule surface and the channel's walls.

Chapter 5

Motion of an Elastic Capsule in a Converging Square Microchannel

Channels with varying cross-sectional area are seen in both microfluidics and microcirculation. In microcirculation, blood vessels bifurcate into daughter branches with smaller dimensions [5]. In microfluidics, flow through converging and diverging channels is being used for sorting cells and for diagnostic purposes [2, 7]. In this chapter, we investigate the dynamics of a capsule in a converging microchannel. We examine the effects of the capsule size, capillary number and viscosity ratio on the flow dynamics.

5.1 Problem Description

We consider an initially spherical Skalak capsule with scaled area-dilation modulus $C = 1$, flowing along the centerline of a straight microchannel with converging cross-sectional area. Three-dimensional views of the problem geometry are shown in figure 5.1. The capsule interior (fluid 1) and exterior (fluid 2) are Newtonian fluids, with viscosities $\lambda\mu$ and μ, and the same density. The capsule size is specified by its volume V or equivalently by the radius a of a sphere of volume $V = (4\pi/3)a^3$. The

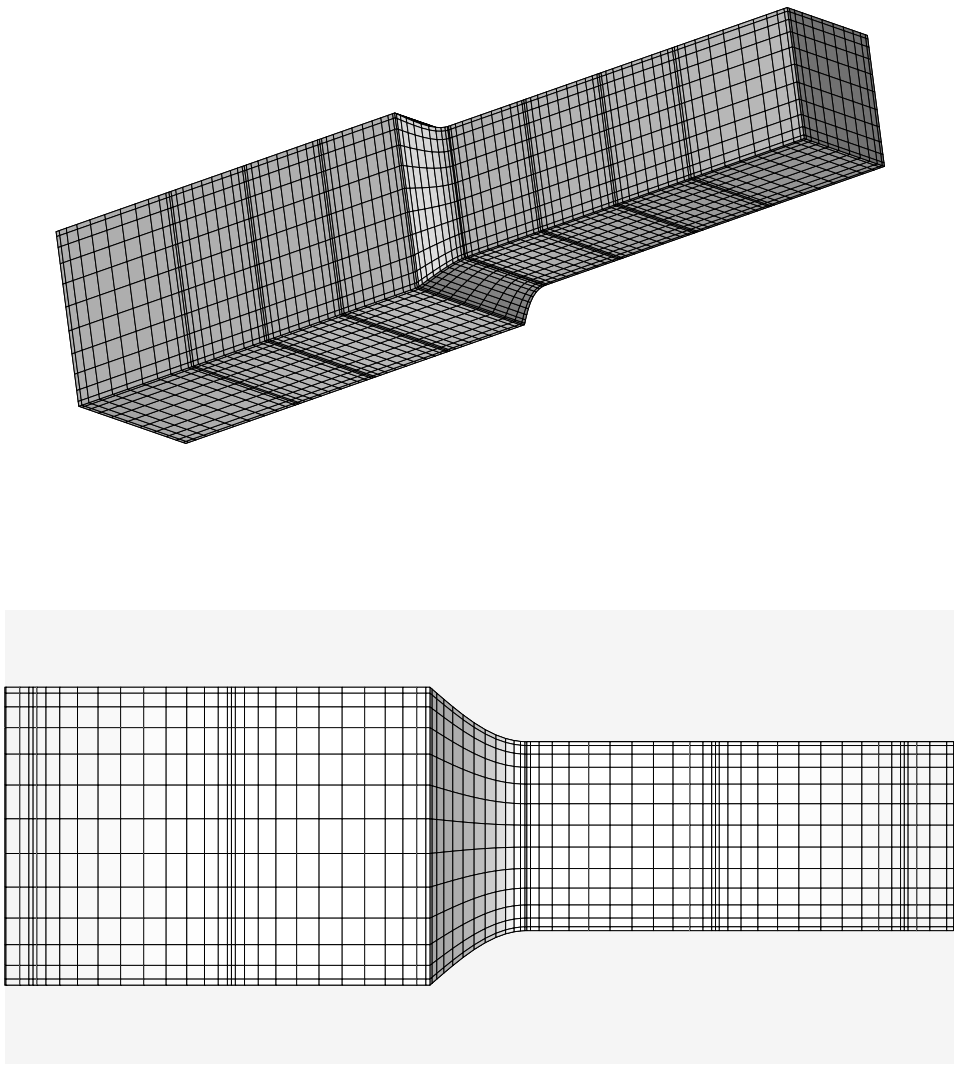

Figure 5.1: Spectral boundary element discretization of system surface:(a) solid surface of the channel, and (b) close view of constriction.

capillary number is defined as

$$Ca = \frac{\mu U_{right}}{G_s} \tag{1}$$

where U_{right} is the average undisturbed velocity in the smaller channel. The surface discretization of the geometry is illustrated in figure 5.1. The surface discretization for the capsule is described in detail in Chapter 3. The channel is divided into three regions i.e. the large channel at the left, the converging region and the small channel at the right. The ratio of the dimension of large to small channel is 1.5. The converging region begins at the origin and the channel surface in the converging region is divided into a row of one spectral element per channel side (i.e. a total of four elements) with half-size equal to l_z. The channel's inlet and outlet are discretized into one element each as shown in figure 5.1. The surface of each channel is divided into 4 rows of four elements each; as seen in the figure 5.1(a). The channel surface (which formally should extend to infinity) has a half length l_x equal to 13 times the cross-sectional dimension l_z. The computations were performed with a discretization employing $N_E = 44$ elements. In this study we mostly utilized $N_B =$ 12 -14 basis points i.e. a total number of spectral points for the entire geometry N $= N_E N_B^2 =$ 6336-8624. The problem studied admits three symmetry planes, y=0, z=0 and y=z. Thus the memory requirements are reduced by a factor of 8^2, the computational time for the system matrices by a factor of 8 and the solution time via direct solvers of the linear systems by a factor of 8^3.

5.2 Effects of Capsule Size

In this section we investigate the effects of capsule size on the motion and deformation of the capsule as it moves along the centreline of a converging channel with ratio of larger to smaller channel 1.5. We examine capsules in the size range $a = 0.6$ to $a = 1.3$. The viscosity ratio is always $\lambda = 1$ and the capillary number is $Ca = 0.05$. We apply a prestress $\alpha_p = 5$ %.

The three-dimensional shape of a capsule with size $a = 1.2$ and capillary number $Ca = 0.2$ at different positions along the converging channel is shown in figure 5.2. The variation in the capsule dimensions and edge curvature as it moves along the curvature is clearly seen in this figure.

Figure 5.3 shows the evolution of the capsule length $L_x/(2a)$ and width $L_y/(2a)$ as the capsule moves along the converging channel. The length and width are scaled with the initial capsule dimensions while X_c is the capsule centroid along the flow direction. We notice that as the capsule size increases the time required to reach steady state increases i.e. the smaller capsules reach steady state faster than the larger capsules. The larger capsule undergoes greater elongation in the converging region. For capsules with size smaller than the channel dimensions, the steady state dimensions before and after passing through the converging region are practically same. For capsules larger than the channel, the steady-state length increases as the capsule size increases while the steady-state width decreases. Figure 5.3(d) shows the evolution of the capsule length L_x^{neg} measured from the capsule centroid to the upstream edge. We see that L_x^{neg} increases steeply in the vicinity of the

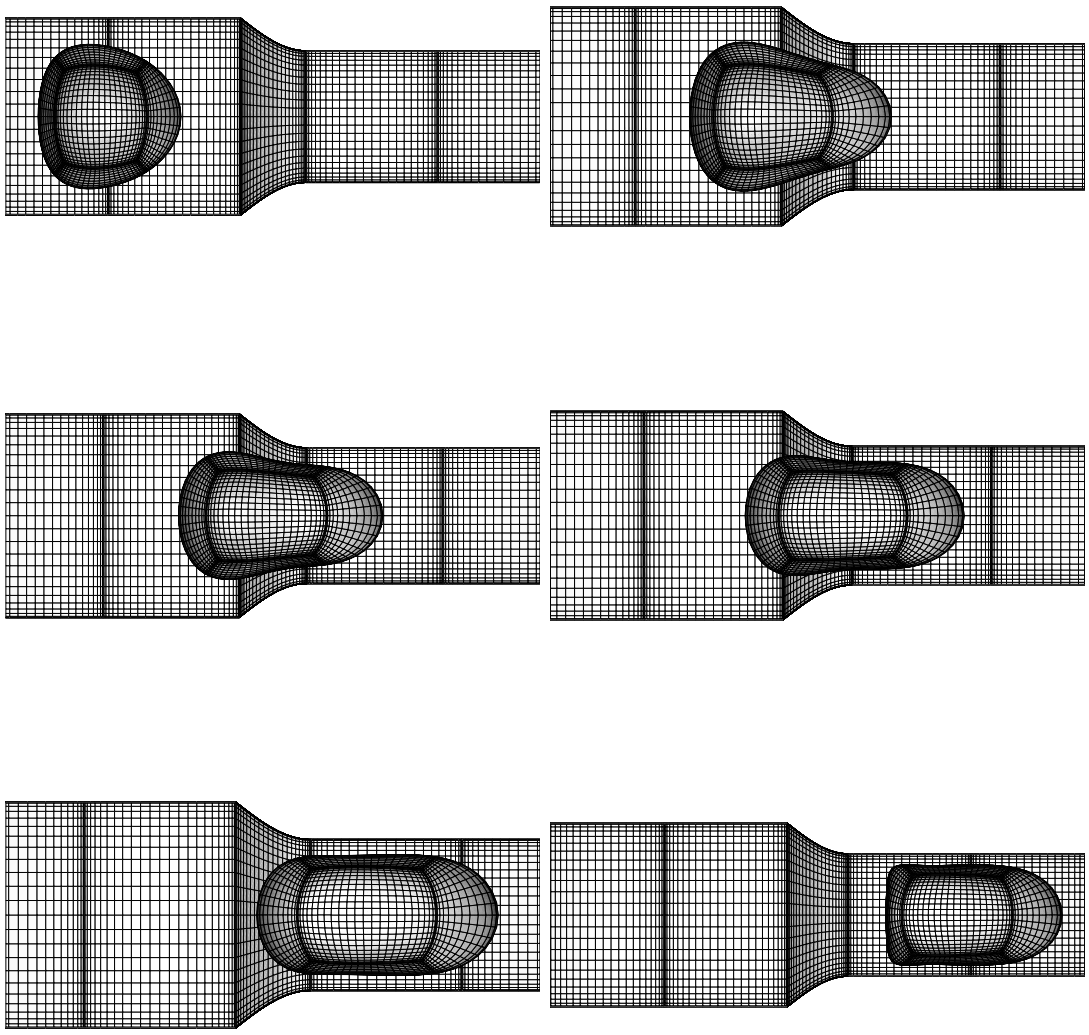

Figure 5.2: Steady-state capsule shape for a Skalak capsule with $C = 1$, capsule size $a = 1.1$, capillary number $Ca = 0.2$, and viscosity ratio $\lambda = 1$ in a converging channel with capsule centroid positioned at X_c = (a) -3 (b) -1 (c) -0.5 (d) 0 (e) 1 (f) 2.

converging region and then decreases to reach steady state in the smaller channel. The elongation of L_x^{neg} in the converging region increases with increasing capsule size.

Next, we examine the evolution of the capsule physical properties as it moves along the converging channel. Figure 5.4(a) shows the evolution of capsule velocity. We observe that the capsule velocity increases on entering into the converging region and reaches a higher steady state value than the previous steady state in the inlet channel. The velocity decreases with increasing capsule size. In figure 5.4(b) we see the evolution of excess pressure drop due to the capsule presence in a converging channel. We see that as the capsule size increases the excess pressure drop also increases. Similar trend is seen for the capsule scaled surface area shown in figure 5.4(c) i.e. the scaled surface area increases with increasing capsule size. In figure 5.5 we present the evolution of the maximum and minimum principal tensions over the capsule surface for several capsule sizes. As shown in figure 5.5(a), the maximum principal tension increases as the capsule moves along the converging channel. The increase is much more pronounced for larger capsules than for smaller capsules. On the other hand, the minimum principal tension decreases as the capsule moves into the converging region. The evolution of the minimum tension is non-monotonic. In the converging region, the minimum tension decreases and then as the capsule moves along the smaller channel, the minimum tension increases and reaches steady state.

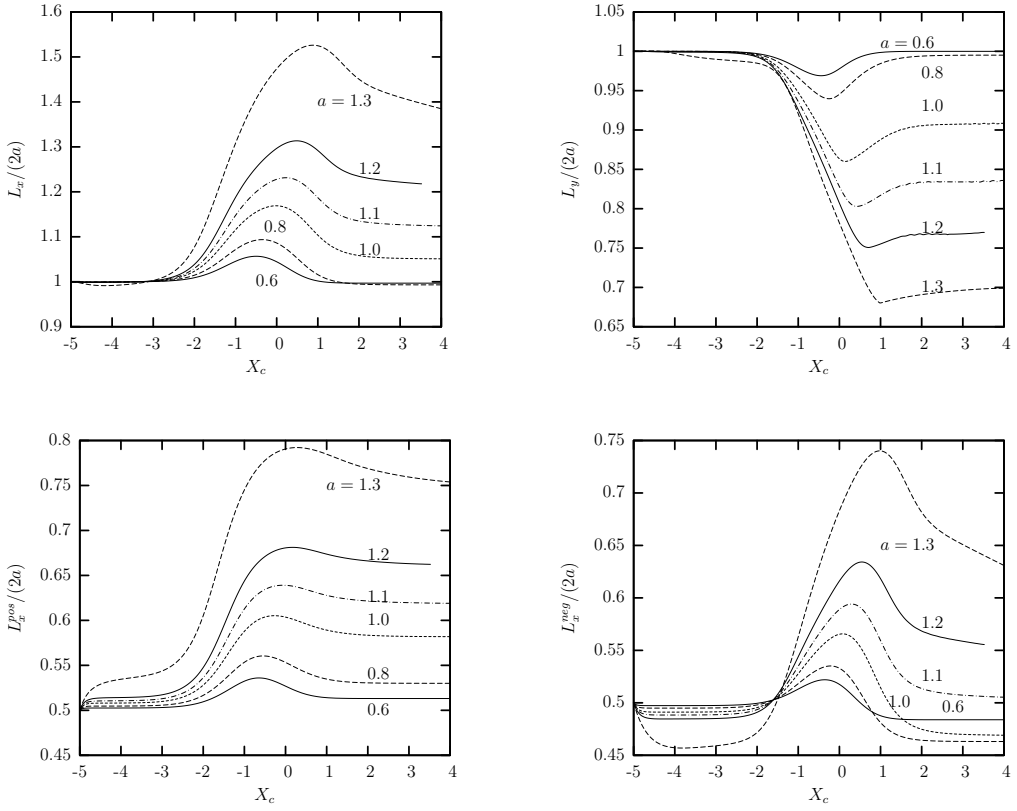

Figure 5.3: Capsule dimensions as a function of capsule centroid X_c for a Skalak capsule with $C = 1$, capillary number $Ca = 0.05$ and $\lambda = 1$ moving along the centerline of a converging channel for capsule size $a = 0.6$, 0.8, 1.0, 1.1, 1.2 and 1.3. (a) Capsule length $L_x/(2a)$. (b) Capsule width $L_y/(2a)$. (c) Capsule length $L_x^{pos}/(2a)$. (d) Capsule length $L_x^{neg}/(2a)$.

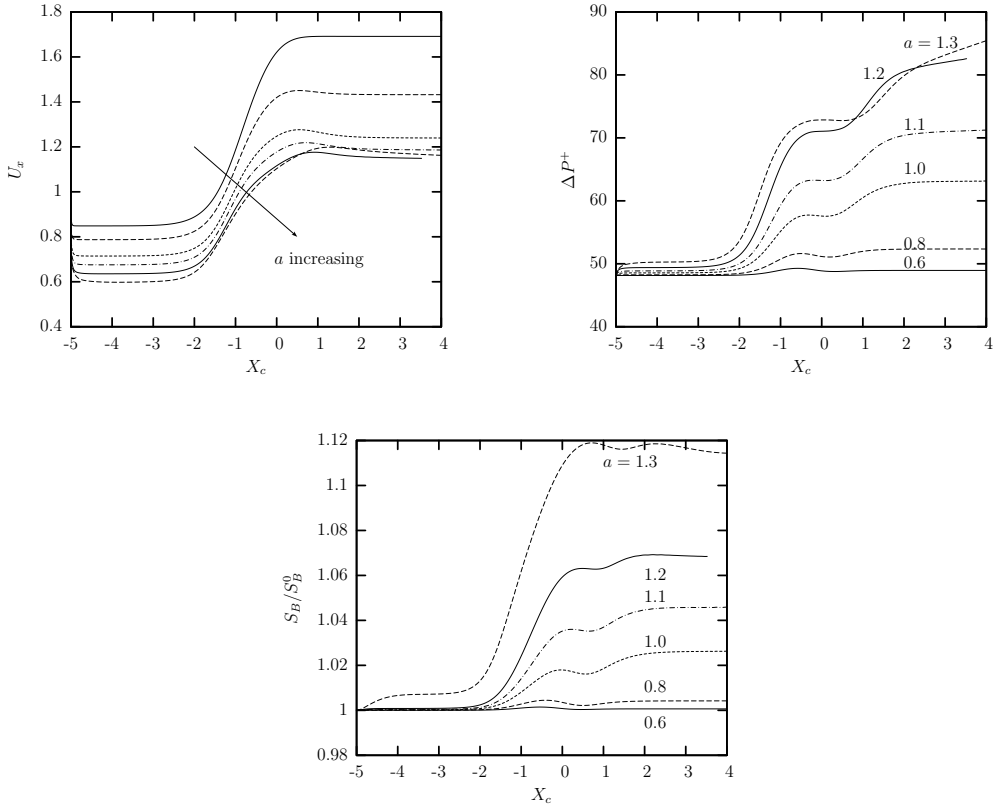

Figure 5.4: Capsule properties as a function of capsule centroid X_c for a Skalak capsule with $C = 1$, capillary number $Ca = 0.05$ and $\lambda = 1$ moving along the centerline of a converging channel for capsule size $a = 0.6$, 0.8, 1.0, 1.1, 1.2 and 1.3.(a) Capsule velocity U_x. (b) Additional pressure drop ΔP^+ owing to the capsule presence. (c) Scaled surface area.

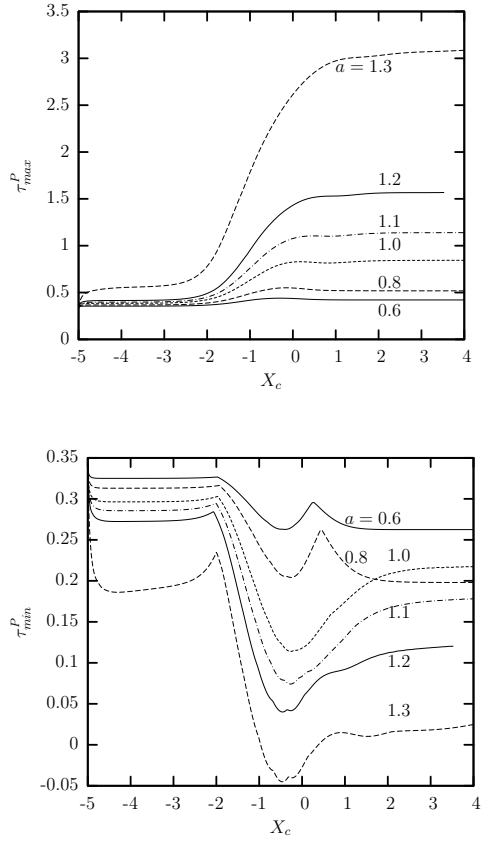

Figure 5.5: Principal tensions among the spectral discretization points on the membrane as a function of capsule centroid X_c for a Skalak capsule with $C = 1$, capillary number $Ca = 0.05$ and $\lambda = 1$ moving along the centreline of a converging channel for capsule size $a = 0.6$, 0.8, 1.0, 1.1, 1.2 and 1.3.(a) Maximum principal tension τ^P_{max}. (b) Minimum principal tension τ^P_{min}.

5.3 Effects of Capillary Number

In this section we investigate the effects of capillary number Ca on the capsule deformation and flow dynamics in a converging microchannel. We consider a Skalak capsule with $C = 1$, prestress $\alpha_p = 5\%$ and size $a = 1.0$. The viscosity ratio is $\lambda = 1$. The range of capillary number studied is from $Ca = 0.05$ to $Ca = 0.2$.

Figure 5.6 shows the capsule profile of a Skalak capsule with size $a = 1.0$ and centroid positioned at $X_c = 0$ for capillary number $Ca = 0.05$, 0.1, 0.15 and 0.2. We observe that as the flow rate increases, the capsule elongation in the axial direction increases and elongation in the lateral direction decreases. Figure 5.7 shows the evolution of the downstream and upstream edge curvature. The downstream curvature remains positive as the capsule moves along the converging region as seen in figure 5.7(a). But the upstream curvature changes from positive to negative as the capsule moves along the converging region. At the entrance of the constriction, we notice that the curvature first increases and then decreases. The magnitude of the increase in curvature in this region increases with increasing capillary number. On moving into the smaller channel, the drop in curvature also increases with increasing capillary number.

Figure 5.8 shows the evolution of the capsule dimensions for a capsule moving along a converging channel for varying capillary numbers. As seen in the figure 5.8(a) the capsule length increases with increasing capillary number. We see that, as the capsule moves into the converging region, its length shows a steep increase and then as the capsule moves into the smaller channel the length reduces and reaches a steady

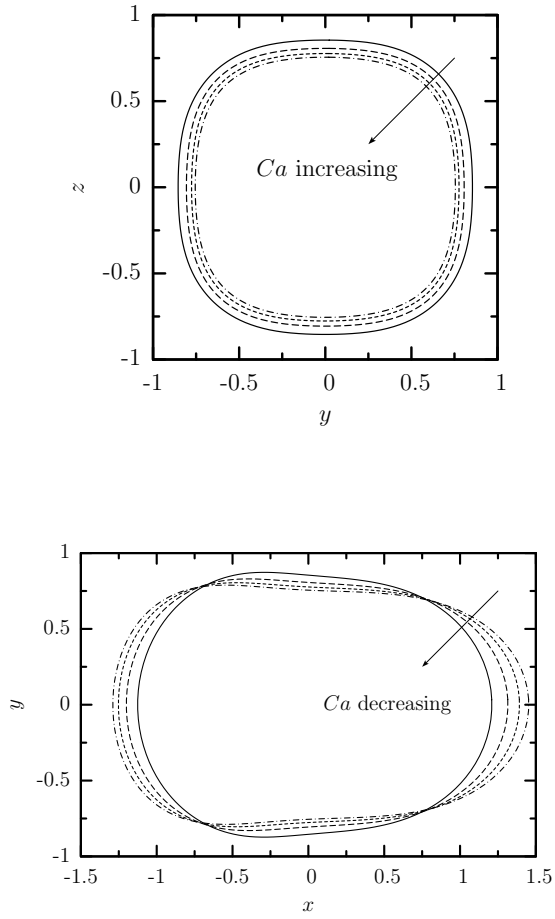

Figure 5.6: Capsule profile as a function of the capillary number Ca for a Skalak capsule with $C = 1$, $\alpha_p = 0.05$ and size $a = 1.0$ in a converging channel with capsule centroid $X_c = 0$ for $Ca = 0.05, 0.1, 0.15, 0.2$. (a) Capsule $y = 0$ profile (i.e. interface intersection with the plane $x = 0$). (b) Capsule $x = 0$ profile. All profiles are shown with centroid $\boldsymbol{x}_c = \mathbf{0}$.

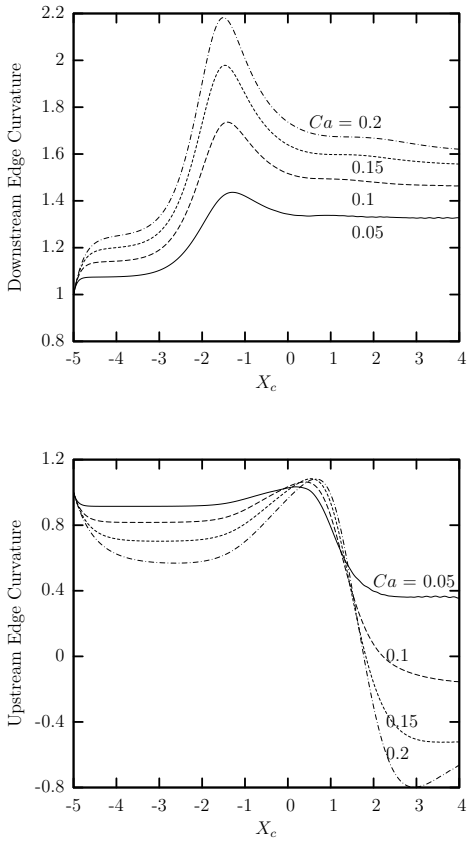

Figure 5.7: Capsule edge curvature (i.e. its intersection with the x-axis) as a function of capsule centroid X_c for a Skalak capsule with $C = 1$, capsule size $a = 1.0$ and $\lambda = 1$ moving along the centerline of a converging channel for capillary number $Ca = 0.05$, 0.1, 0.15, and 0.2. (a) Downstream edge curvature. (b) Upstream edge curvature.

state. The elongation in the converging region is a function of capillary number and increases with increasing flow rate. The capsule width shows the opposite behavior. As seen in the figure 5.8(b) the capsule width decreases sharply in the converging region and then increases before reaching the steady state value. The greater the capillary number, the larger is the decrease in capsule width as it moves into the converging channel.

The evolution of the capsule velocity as it moves along the converging channel is shown in the figure 5.9(a). We notice that as the capillary number increases, the velocity in the converging channel increases. Similar behavior is observed for the scaled surface area of the capsule in figure 5.9(c). The excess pressure drop due to the presence of the capsule decreases with increasing capillary number as shown in figure 5.9(b). This is because of the larger capsule deformation at higher capillary numbers resulting in lower blockage of the channel. In figure 5.10 we present the evolution of the maximum and minimum principal tensions over the capsule surface for several capillary numbers. As shown in figure 5.10(a), the maximum principal tension increases as the capsule moves along the converging channel. The principal tension is greater for higher capillary numbers. We also see in figure 5.10(a) that the maximum tension shows non-monotonic behavior for larger capillary numbers in the vicinity of the converging region. The minimum principal tension decreases as the capsule moves into the converging region. The evolution of the minimum tension is non-monotonic in the range of capillary numbers studied. In the converging region, the minimum tension decreases and then as the capsule moves into the smaller channel, the minimum tension increases and reaches steady state.

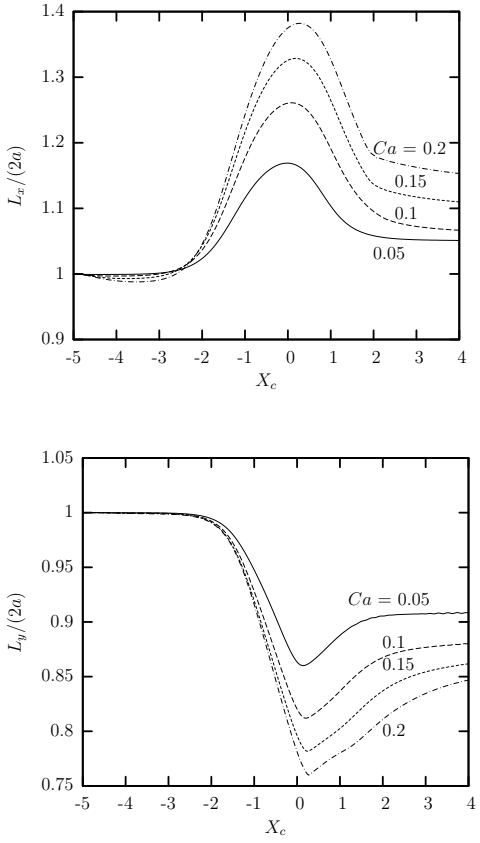

Figure 5.8: Capsule dimensions as a function of capsule centroid X_c for a Skalak capsule with $C = 1$, capsule size $a = 1.0$ and $\lambda = 1$ moving along the centerline of a converging channel for capillary number $Ca = 0.05$, 0.1, 0.15, and 0.2. (a) Capsule length $L_x/(2a)$. (b) Capsule width $L_y/(2a)$.

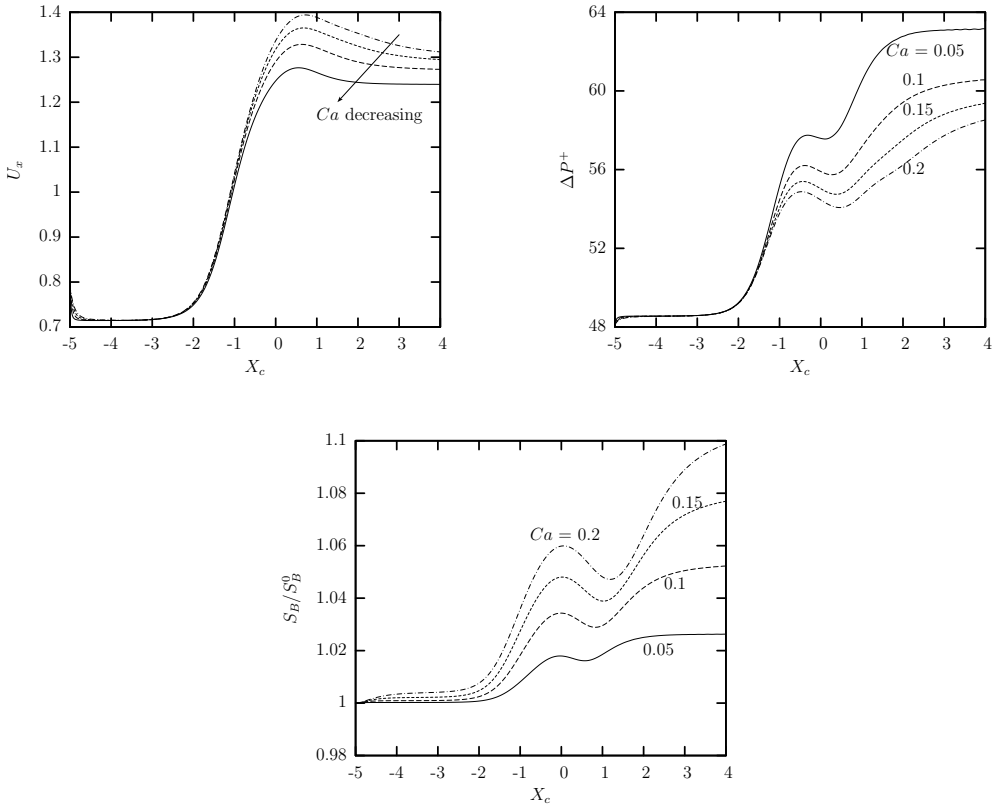

Figure 5.9: Capsule properties as a function of capsule centroid X_c for a Skalak capsule with $C = 1$, capsule size $a = 1.0$ and $\lambda = 1$ moving along the centerline of a converging channel for capillary number $Ca = 0.05$, 0.1, 0.15, and 0.2. (a) Capsule velocity U_x. (b) Additional pressure drop ΔP^+ owing to the capsule presence. (c) Scaled surface area.

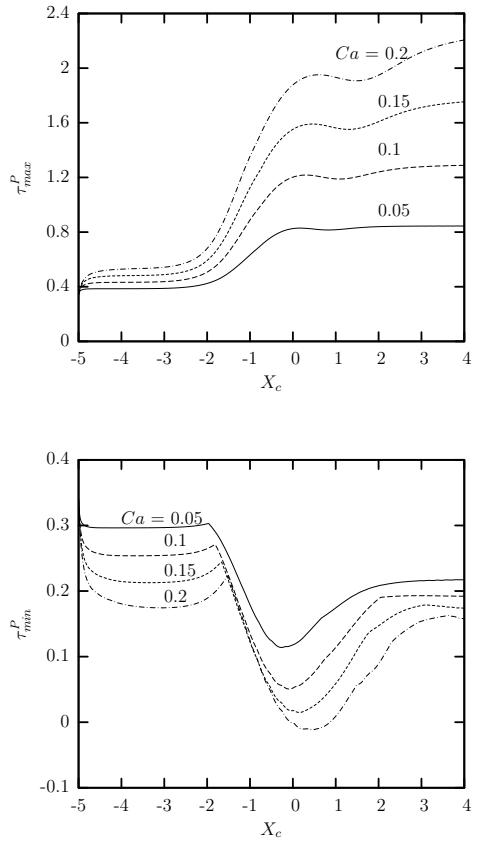

Figure 5.10: Principal tensions among the spectral discretization points on the membrane as a function of capsule centroid X_c for a Skalak capsule with $C = 1$, capsule size $a = 1.0$ and $\lambda = 1$ moving along the centerline of a converging channel for capillary number $Ca = 0.05$, 0.1, 0.15, and 0.2. (a) Maximum principal tension τ^P_{max}. (b) Minimum principal tension τ^P_{min}.

5.4 Effects of Viscosity Ratio

In this section we investigate the effects of viscosity ratio on the capsule deformation and flow dynamics in a converging microchannel. We consider a Skalak capsule with $C = 1$, prestress $\alpha_p = 5\%$, capillary number $Ca = 0.1$ and size $a = 1.0$. We examine the capsule motion and deformation for three different viscosity ratios $\lambda = 0.01$, 1.0 and 10.

Figure 5.11 shows the evolution of the capsule dimensions as the capsule moves along the converging channel for several viscosity ratios. As shown in the figure, for the smaller viscosity ratios $\lambda = 0.01$ and 1.0 there is no effect of the increase in viscosity ratio on the capsule deformation. But for the largest viscosity ratio $\lambda = 10$, we see a significant difference in the capsule behavior. As seen in figure 5.11(a), for this viscosity ratio the length of the smaller channel required to reach equilibrium is higher. In the vicinity of the converging region the capsule deformation decreases with increasing viscosity ratio. The evolution of capsule width for varying viscosity ratio is shown in figure 5.11(b). Here we also see that, as the viscosity ratio increases, the capsule deformation decreases in the vicinity of the converging region. But the steady-state value for all cases under consideration is the same as expected since at steady state in a straight channel there is no flow inside the capsule.

Figure 5.12 shows the evolution of capsules physical properties for a Skalak capsule with $C = 1$, capsule size $a = 1.0$ and capillary number $Ca = 0.1$ moving along the centerline of a converging channel for viscosity ratio $\lambda = 0.01$, 1.0 and 10. We see in figure 5.12(a) that there is only a very slight variation in the capsule

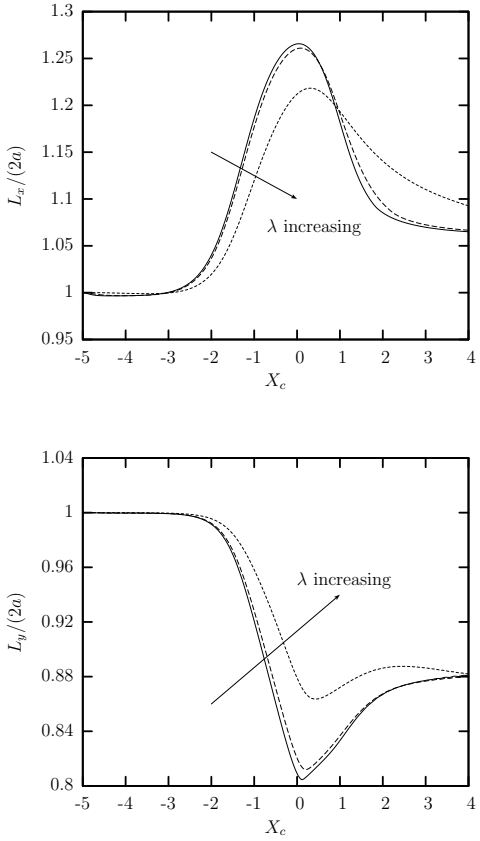

Figure 5.11: Capsule dimensions as a function of capsule centroid X_c for a Skalak capsule with $C = 1$, capsule size $a = 1.0$ and capillary number $Ca = 0.1$ moving along the centerline of a converging channel for viscosity ratios $\lambda = 0.01$, 1.0 and 10. (a) Capsule length $L_x/(2a)$. (b) Capsule width $L_y/(2a)$.

velocity with varying viscosity ratio. Figure 5.12(b) shows the excess pressure drop for varying viscosity ratios. We see that the value of the excess pressure drop increases with increasing viscosity ratio. The scaled surface area decreases with increasing viscosity ratio as seen in the figure 5.12(c).

Figure 5.13 shows the evolution of the principal tension as the capsule moves along a converging channel. We see that for large viscosity ratios, there is a significant effect on the capsule properties as it moves along the converging channel. The maximum principal tension τ^p_{max} is lower while the minimum principal tension τ^p_{min} is higher for the high-viscosity ratio capsules in the vicinity of the converging channel.

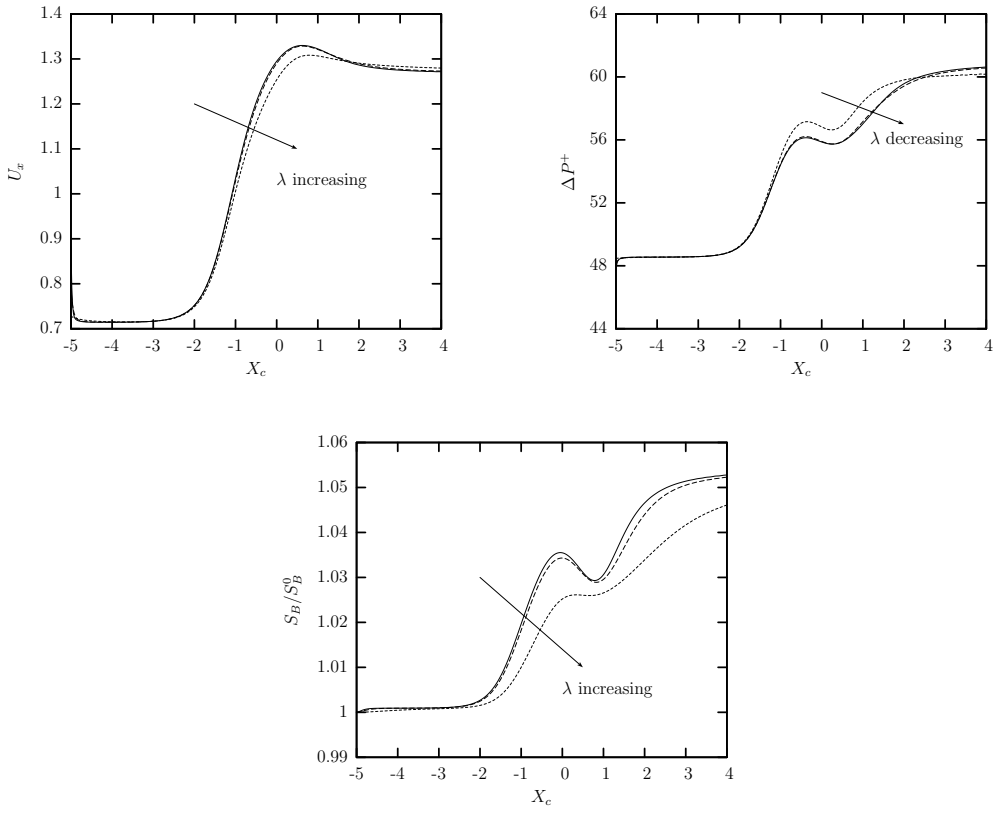

Figure 5.12: Capsule properties as a function of capsule centroid X_c for a Skalak capsule with $C = 1$, capsule size $a = 1.0$ and capillary number $Ca = 0.1$ moving along the centerline of a converging channel for viscosity ratios $\lambda = 0.01$, 1.0 and 10. (a) Capsule velocity U_x. (b) Additional pressure drop ΔP^+ owing to the capsule presence. (c) Scaled surface area.

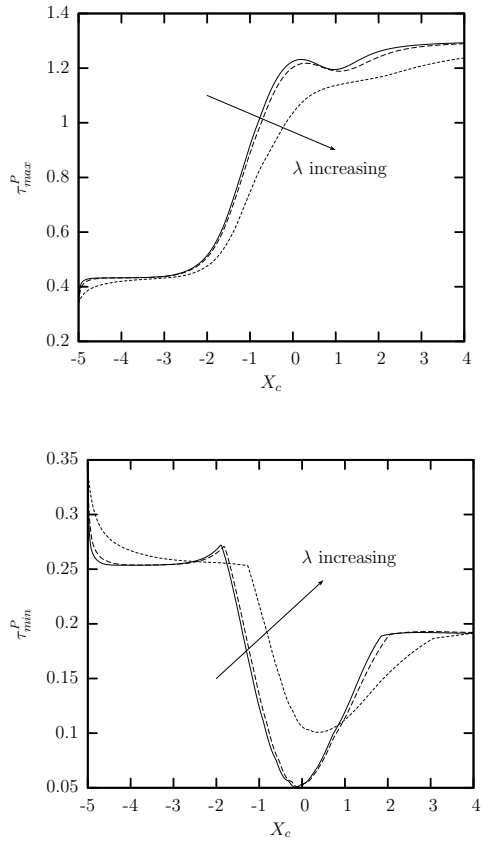

Figure 5.13: Principal tensions among the spectral discretization points on the membrane as a function of capsule centroid X_c for a Skalak capsule with $C = 1$, capsule size $a = 1.0$ and capillary number $Ca = 0.1$ moving along the centerline of a converging channel for viscosity ratios $\lambda = 0.01$, 1.0 and 10. (a) Maximum principal tension τ^P_{max}. (b) Minimum principal tension τ^P_{min}.

Chapter 6

Hemodynamic Forces on Vascular Endothelial Cells and Leukocytes in Blood Microvessels

In this chapter, we investigate the hemodynamic forces on vascular endothelial cells and leukocytes in microvessels. Previously, Wang and Dimitrakopoulos [64] studied the hemodynamic forces on endothelial cells and leukocytes adhering to the surface of blood vessels. Here, we study the effects of a leukocyte moving along the blood vessel on the hemodynamic forces on the endothelial cells. We also examine the hemodynamic forces experienced by the leukocyte as it moves along the microvessel. The hemodynamic forces on the endothelial cells play a significant role in determining the function of these cells.

6.1 Introduction

Low-Reynolds-number flow past particles in cylindrical channels can be representative of many physical situations encountered in biological systems and engineering like the motion of leukocytes in blood vessels, transport of particles in

pipes, membrane filtration, microfluidics, etc. Hence the hydrodynamic forces on particles in cylindrical channels have been investigated extensively both analytically and numerically. Brenner and Happel [71] studied the motion of a sphere in a cylindrical tube using the method of reflections and calculated the drag experienced by the sphere. Higdon and Muldowney [78] evaluated the resistance functions for low-Reynolds-number flow past spherical particles, droplets and bubbles in cylindrical domains using the spectral boundary element method. Quddus, Moussa and Bhattacharjee [84] used the arbitrary Lagrangian-Eulerian(ALE) kinematics to describe the motion of a rigid sphere in a cylindrical channel. Most of these studies were carried out under the assumption of smooth channel which may not be true in the real world, particularly at micro scales. For example, the blood vessels are not smooth cylinders but are bumpy channels due to the presence of the endothelial cells. Adherent leukocytes also result in bumps on the vessel wall. Similarly surface roughness which can be neglected in macroscopic systems becomes significant factor in microfluidic systems and alter the hydrodynamic forces on various system bodies. Thus it is important to take into account the surface roughness while studying systems in the micro-scale.

This study investigates the effects of a bump on a cylinder surface on the hydrodynamic forces on the particle flowing through the cylinder. We also examine the effects of the moving particle on the forces exerted on the bump. The motivation for this study was to investigate the hemodynamic forces on a leukocyte flowing though blood vessels or adhering to the vessel wall and on the endothelial cells.

6.1.1 Review of Previous Work

Leukocytes or white blood cells play a key role in the inflammation process. Blood contains about one leukocyte for every 100 red blood cells. Leukocytes travel through the blood vessels and at the site of infection attaches themselves to the walls. The hemodynamic forces are supposed to play a crucial role in the leukocyte margination process which precedes the adhesion of leukocyte to the endothelial cell. Endothelial cells which line the blood vessels play a critical role in regulating vascular functions. Endothelial cells sense changes in physiological conditions through humoral factors as well as hemodynamic forces [89]. Shear stress acting on the endothelial cell stimulates the release of vasoactive substances and changes gene expression, cell metabolism and cell morphology [89]. The fluid forces on endothelial cells and leukocytes have been the subject of numerous investigations because of its significant role in the physiological processes. A number of authors have investigated the leukocyte flow in blood vessels. King *et al.* [80] characterized how the adherent leukocytes and suspended erythrocytes alter the streamlines of blood flow in post-capillary venules both experimentally and numerically. They observed a reduction in shear stress experienced by endothelium in the presence of adherent leukocyte. A number of studies have investigated leukocytes adhering to the microvessel wall [74, 75, 86, 87]. Sugihara-Seki and Schmid-Schönbein [88] determined the shear stress on a single leukocyte membrane for both adherent and freely suspended leukocytes. Chapman and Cokelet [73] calculated the flow resistance and drag forces due to multiple adherent leukocytes in post-capillary vessel and they

found that the drag force increased when the leukocytes are on the opposite sides of vessel wall. Kim and Sarelius [79] showed experimentally that the leukocyte rolling increased as a function of wall shear rate. The fluid forces on endothelial cells have been speculated to be responsible for stimulation of cellular responses essential for endothelial cell function [77, 85]. Wang and Dimitrakopoulos [64] studied the hemodynamic forces on endothelial cells and leukocytes attached to the inner surface of a blood vessel and investigated the relative importance of the normal and shear component of the force. Here we extend this study, by studying the impact of a suspended leukocyte on the hemodynamic forces on the endothelial cells and adhering or rolling leukocyte.

In this chapter, we investigate the changes in hemodynamic force and its components (i.e. shear stress and normal force) on the endothelial cell and leukocyte because of mutual interactions. First, we study the hemodynamic forces on endothelial cell and adherent or rolling leukocyte in the presence of a suspended leukocyte. Second, we study the forces acting on the suspended sphere. Our motive in this is to investigate the impact of a adherent leukocyte or rolling leukocyte on the suspended leukocyte. Another physical situation that can be explained using our results is the effects of constriction on the forces acting on a suspended particle. We have used previously developed [81, 76] spectral boundary element method.

6.2 Problem Description

We consider a three-dimensional cell attached to the inner surface of a vessel and a leukocyte above it at the center of the vessel. The center of the cell and the leukocyte are on the same vertical line. The vessel is modeled as a cylindrical tube with radius R and half length L. The leukocyte is modeled as a solid sphere lying on the axis of the cylinder above the cell of radius R_s. The attached cell is modeled as a spherical cap with radius $\tilde{a}$. The cell model represents endothelial cell when the spreading angles are low and it represents leukocyte when the spreading angles are very large or the cell is less spread. Three-dimensional views of the problem geometry are shown in figure 6.1. The computations were performed with a discretization employing $N_E = 44$ elements. The surface of the cell is divided into a total of five elements as shown in figure 6.1. In the immediate vicinity of the cell, the vessel surface is divided into two rows with eight elements each. The vessel surface above the cell is discretized into two spectral elements. The remaining vessel surface is divided into three rows with two elements in each row. The vessel's inlet and outlet are discretized into 5 elements each, as shown in figure 6.1(c). The solid sphere is discretized into 6 spectral elements by cube projection. In this study we mostly utilized $N_B = 11$ -13 basis points i.e. a total number of spectral points for the entire geometry N = $N_E N_B^2$ = 5324-7436. The problem studied admits only one symmetry plane i.e. $y = 0$. Thus the memory requirements are reduced by a factor of 2^2, the computational time for the system matrices by a factor of 2 and the solution time via direct solvers of the linear systems by a factor of 2^3.

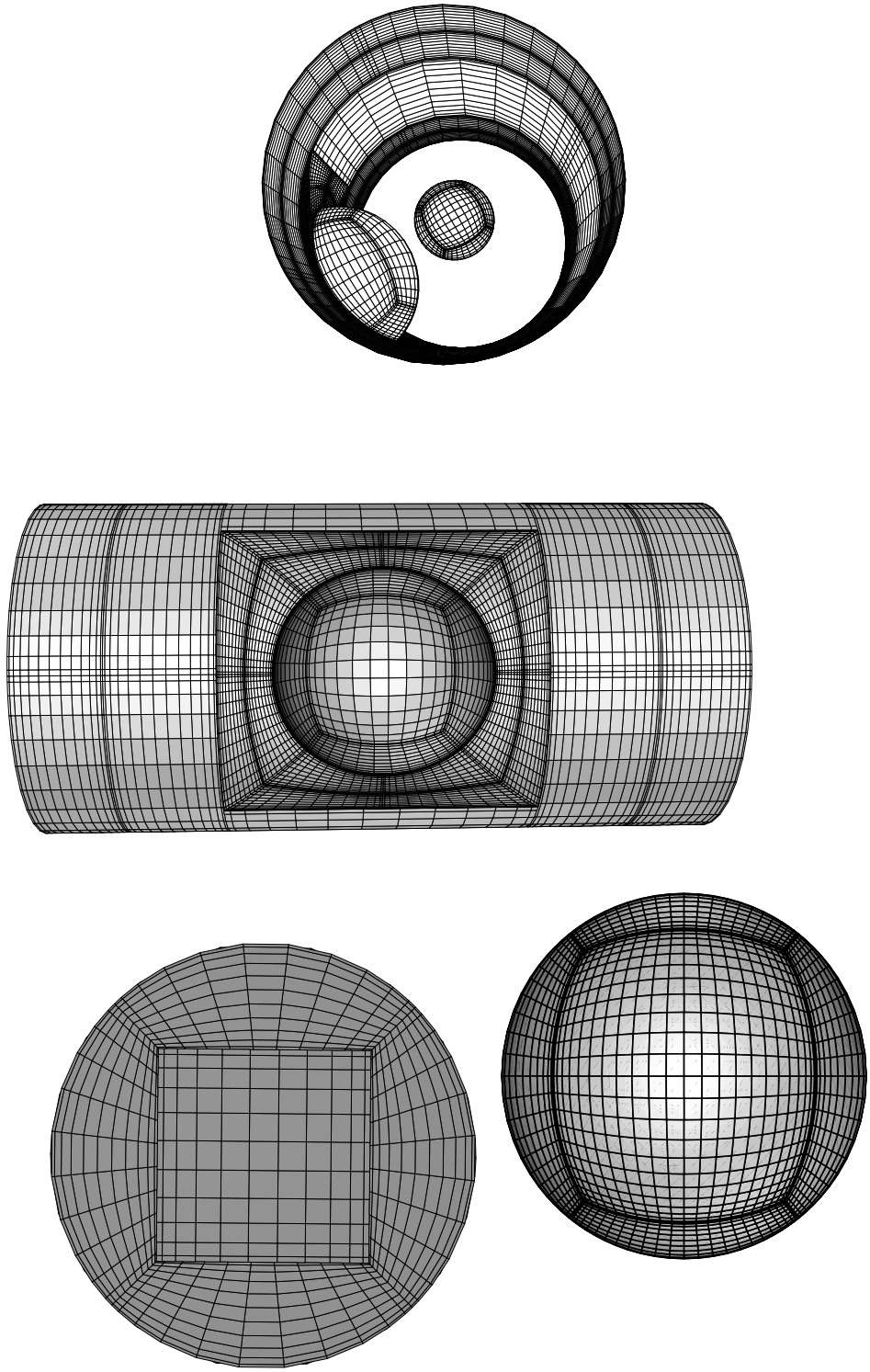

Figure 6.1: Spectral boundary element discretization of system surface: (a) solid surface of the vessel, (b) top view, (c) inlet or outlet fluid surface and (d) solid sphere.

The local shear stress magnitude τ and normal force f_n on the cell surface and its vicinity may be defined by

$$\tau = \sqrt{(f_x^L)^2 + (f_y^L)^2} \quad and \quad f_n = f_z^L \tag{1}$$

respectively. The total force F_x on the cell is given by

$$F_x = \int_{S_c} f_x \mathrm{d}S \tag{2}$$

where S_c is the cell's surface area. In the above equations, $\boldsymbol{f}$ is the force vector defined at the global Cartesian coordinate system. Its corresponding vector defined at a local Cartesian coordinate system (x^L, y^L, z^L) is denoted as $\boldsymbol{f^L} = (f_x^L, f_y^L, f_z^L)$. The linearity of Stokes equation permits the expression of force in terms of resistance functions defined by

$$F_x = 6\pi\mu a R_x u_x \quad and \quad F_z = 6\pi\mu a R_z u_z \tag{3}$$

There is no force in the y-direction because of symmetry. The resistance coefficients are dimensionless quantities and are functions of particle size and position only. We have expressed our results in terms of the resistance coefficients.

6.3 Hemodynamic Forces on Adherent/Rolling Leukocytes or Endothelial Cells

Figure 6.2 shows the force and its components acting on the cell in the presence of a freely suspended sphere in the x-direction. The force is plotted in terms of the resistance function. The figure shows that as the cell size increases the total force

on the cell initially shows an increasing trend but after a particular value it drops off. Similar trend is observed for the shear component but the normal component of the force shows a steady increase. This behavior was observed over the whole range of angles studied. For the lower angles the cell is representative of endothelial cells while for higher angles, the cell represents leukocytes. The presence of the suspended sphere results in blocking of the flow and thus the forces on the cell increases. But as the gap between the cell and the sphere decreases the decreasing flow results in significant lowering of the forces in the x direction. It can be seen in figure 6.2 that for a given $\tilde{a}/R$ the force increases with increasing spreading angle. Greater the spreading angle, less spread is the cell and hence there will be greater blocking of the flow resulting in higher forces.

Figure 6.3 shows the forces in the z-direction. The trend is different from the previous figure. Here we see that the increase in the cell size results in a sharp increase in the forces and its components as the size of the cell increases. Comparing the magnitude of forces in x and z-direction shows that the force in x-direction is negligible compared to the force in the z direction. The presence of the sphere results in a significant increase in the z-direction forces. This sharp increase in the force can be attributed to the decreasing gap between the sphere and the cell which approaches the lubrication regime as the cell size increases.

In order to see how the forces are changing in the presence of the sphere, we plotted the forces and its components in the presence of spheres of different size. In figure 6.4 we plot the total, normal and shear force in the x-direction on a cell with spreading angle 60^o as a function of the cell size and in the presence of

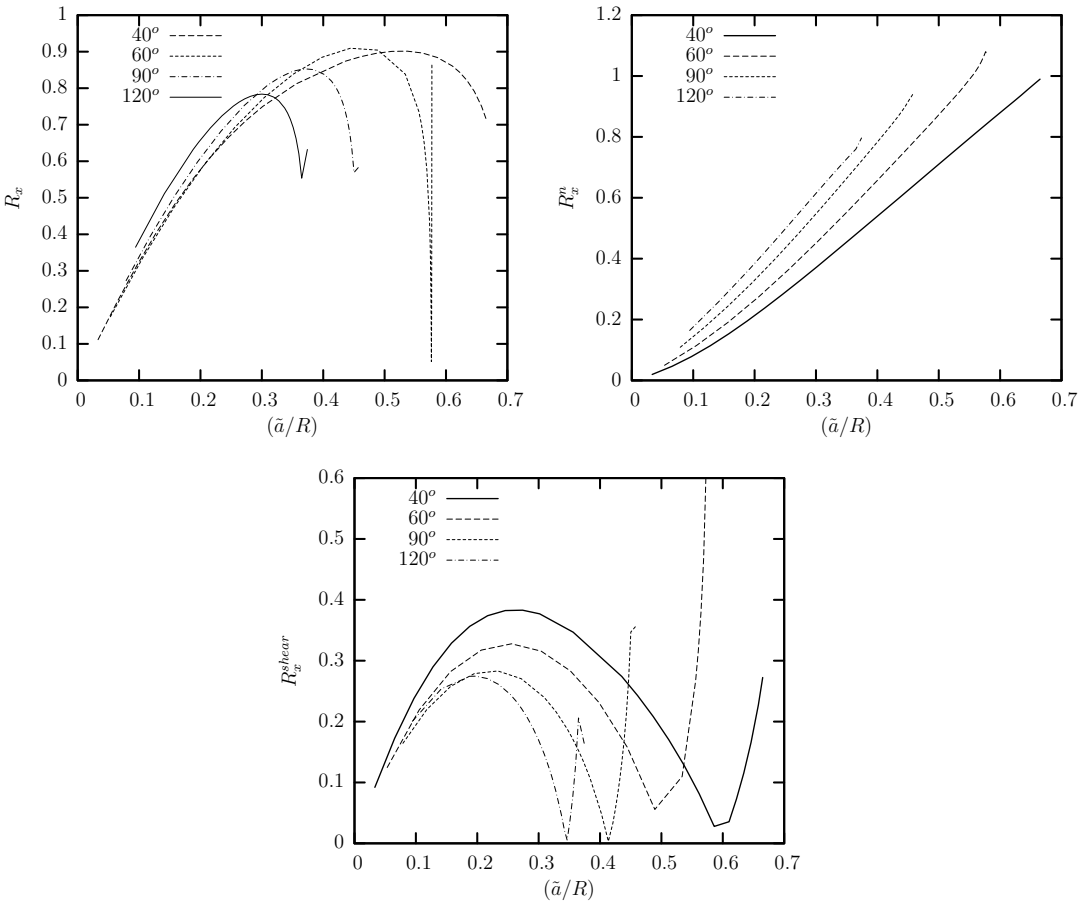

Figure 6.2: Resistance function for the cell in x-direction as a function of the cell size $\tilde{a}/R$. The spreading angles is $\theta_0 = 40^o, 60^o, 90^o$ and 120^o. Resistance function for the (a) Total force R_x, (b) Normal force R_x^n, and (c) Shear force R_x^{shear}.

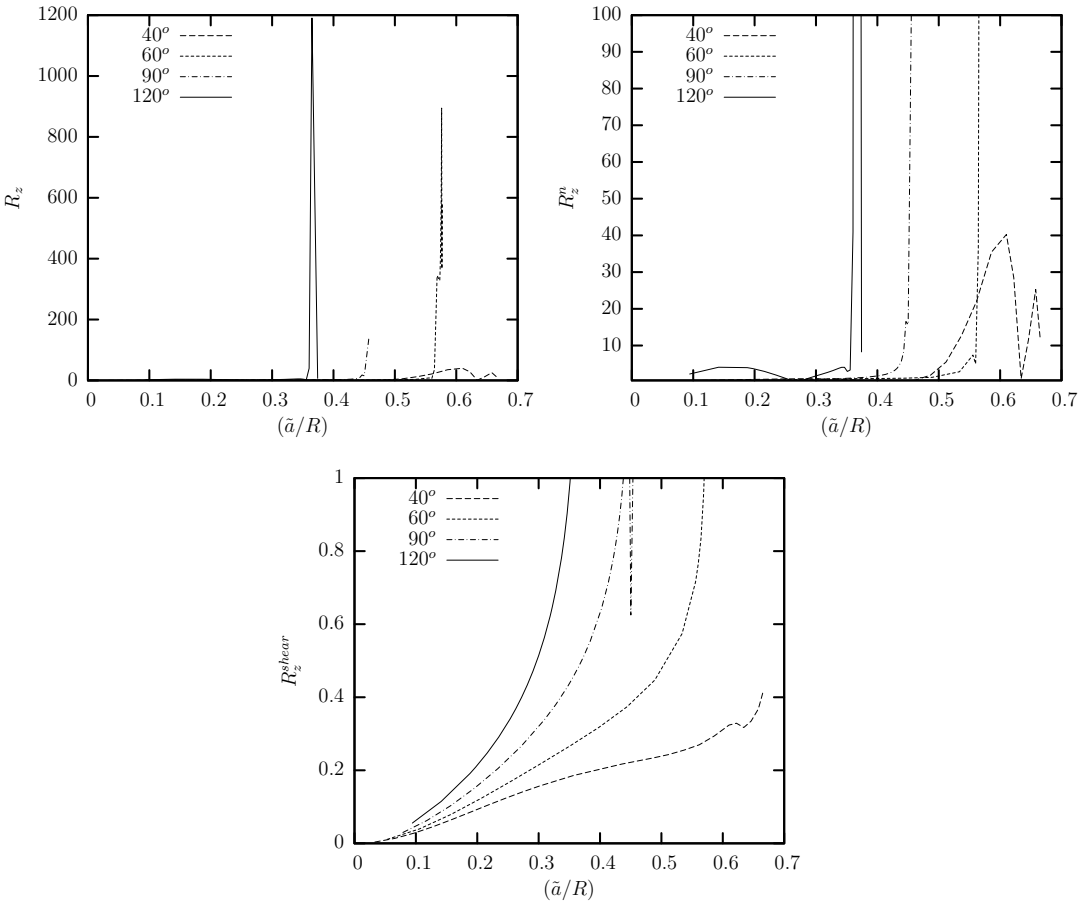

Figure 6.3: Resistance function for the cell in z-direction as a function of the cell size $\tilde{a}/R$. The spreading angles is $\theta_0 = 40^o, 60^o, 90^o$ and 120^o. Resistance function for the (a) Total force R_x, (b) Normal force R_x^n, and (c) Shear force R_x^{shear}.

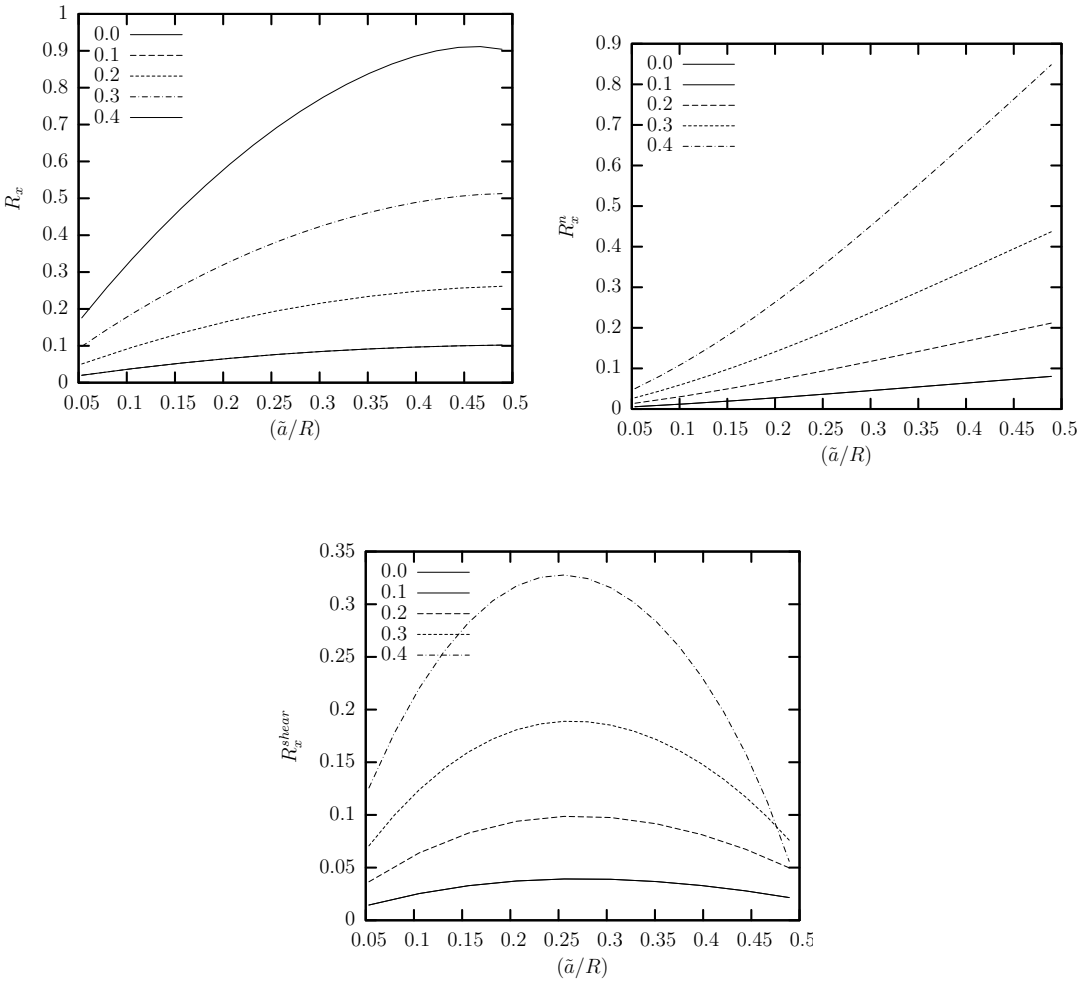

Figure 6.4: Resistance function for the cell in x-direction as a function of the cell size $\tilde{a}/R$. The spreading angles is $\theta_0 = 60^o$. The size of the sphere is $R_s = 0.0$, 0.1, 0.2. 0.3 and 0.4. Resistance function for the (a) Total force R_x, (b) Normal force R_x^n, and (c) Shear force R_x^{shear}.

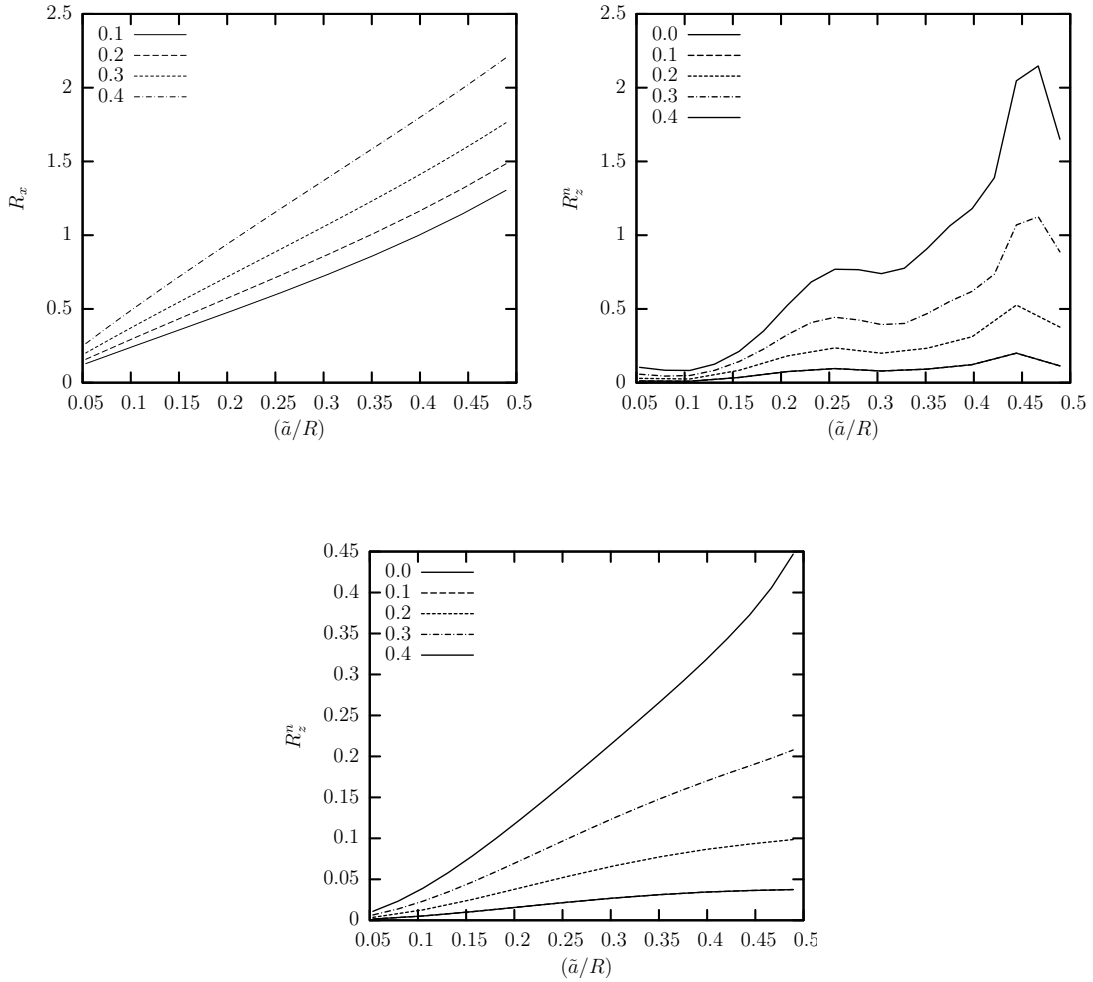

Figure 6.5: Resistance function for the cell in z-direction as a function of the cell size $\tilde{a}/R$. The spreading angles is $\theta_0 = 60^o$. The size of the sphere is $R_s = 0.0$, 0.1, 0.2. 0.3 and 0.4. Resistance function for the (a) Total force R_x, (b) Normal force R_x^n, and (c) Shear force R_x^{shear}.

spheres of different radii. For very small radius the presence of sphere is seen to have negligible effect. But as the radius of the sphere increases the the force increases significantly. In the presence of a sphere of radius 0.4 which is representative of leukocyte the force increases sharply with increasing cell size. As seen in figure 6.4(a) for smaller cells the total force in the presence of leukocyte increases by a factor of 2 which increases to almost 9 for the largest cell studied. The increase in shear force is also more pronounced for larger cells. Thus the magnitude of total force on leukocytes adhering to vessel walls will be significantly affected by suspended leukocytes. The normal force also shows similar behavior as shown in figure 6.4(b). The shear force however drops off as the cell size increases beyond a particular value. Thus the presence of a suspended leukocyte affects the shear force on moderately sized cells much more significantly than large cells or very small cells. Comparing with previous results of Wang and Dimitrakopoulos [64] we can see that the presence of leukocyte results in a significant effect on the force change with increasing cell size and spreading. In the absence of leukocytes as shown in figures 15, 20 and 23 of Wang and Dimitrakopoulos [64] we see that the total force as well as the shear and normal components increase with increasing cell size and spreading angle. But the presence of suspended leukocyte changes this trend. As seen in figure 6.2 the total force and shear force increases initially as the cell size increases but at a threshold size this trend reverses. The presence of suspended leukocyte may be a stimuli for endothelial cell functions related to leukocyte adhesion. Previous study done by Wang and Dimitrakopoulos [64] had shown that at larger cell sizes the normal force component also becomes significant. In the presence of leukocyte because of the

decreasing trend of shear force for larger cell the normal force will become much more significant. Caputo and King [72] observed an optimum shear rate of $100s^{-1}$ for rolling of leukocyte on endothelial cell.

Forces in the z-direction are plotted in figure 6.5. The forces show a steady increase with increasing cell size in the z-direction. Both normal and shear components show an increasing trend unlike x-direction. Clearly the presence of a sphere results in significant changes in the forces over the cell.

6.4 Hemodynamic Forces on Freely Suspended Leukocytes

In this section the forces on a sphere which is representative of a suspended leukocyte in the presence of an adherent cell on the cylinder wall is investigated. Our motive in this was to see how the presence of a cell changes the forces on the leukocytes. In microcirculation this cell can be another adherent leukocyte or the endothelial cell. Artoli and Saldanha [70] have previously shown that shear stress distribution on the leukocyte increases as it comes closer to the the endothelial cell. Also how the forces on leukocyte changes in the presence of adherent leukocyte may shed some light on the mechanism of leukocyte margination and attachment to the vessel walls.

In the presence of the cell there is symmetry only in the y direction. The resistance functions for the sphere in x direction are plotted in figure 6.6 as a function of $\tilde{a}/R$ for various θ. For the same $\tilde{a}/R$ as θ increases the resistance function shows a gradual increase. This increase can be attributed to the higher blocking resulting

at higher angles. Also for each angle after a threshold value of $\tilde{a}/R$ the resistance function increases sharply. The narrowing of the gap between the bump and the sphere may be the cause of this sudden jump. As the gap decreases and reaches lubrication regime the forces increase significantly. The resistance function for the normal and shear also show similar trend. But there is a sharper increase in the shear force with increasing cell size. The resistance functions for the sphere in z direction are plotted in figure 6.7 as a function of $\tilde{a}/R$. The forces are almost constant at smaller cell sizes. Hence small cells do not affect the forces on the suspended leukocyte. For a cell with spreading angle of 60^o for cell size $\tilde{a}/R = 0.2$ we can see that the force on the suspended leukocyte increases. Both normal and shear force also show similar trend. We observe in figure 6.7 that as the spreading angle increases the size of cell which affects the forces on leukocytes decreases.

Figure 6.8 shows the variation in resistance function as the sphere radii changes in the x-direction. As shown in figure 6.8 the increase in the radius of sphere results in increase in the resistance function and this increase is constant over the studied range of $\tilde{a}/R$. The forces in the z-direction are plotted in figure 6.9.

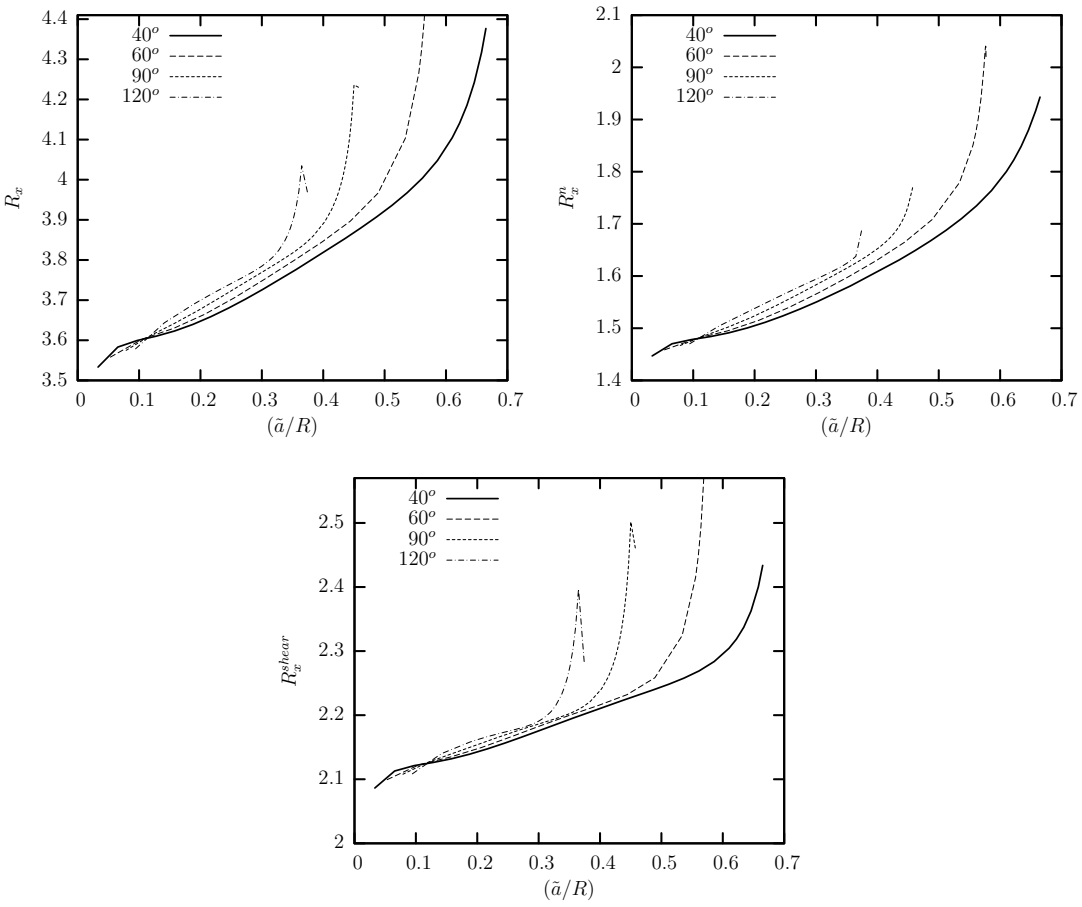

Figure 6.6: Resistance function for the sphere in x-direction as a function of the cell size $\tilde{a}/R$. The spreading angles is $\theta_0 = 40^o, 60^o, 90^o$ and 120^o. Resistance function for the (a) Total force R_x, (b) Normal force R_x^n, and (c) Shear force R_x^{shear}.

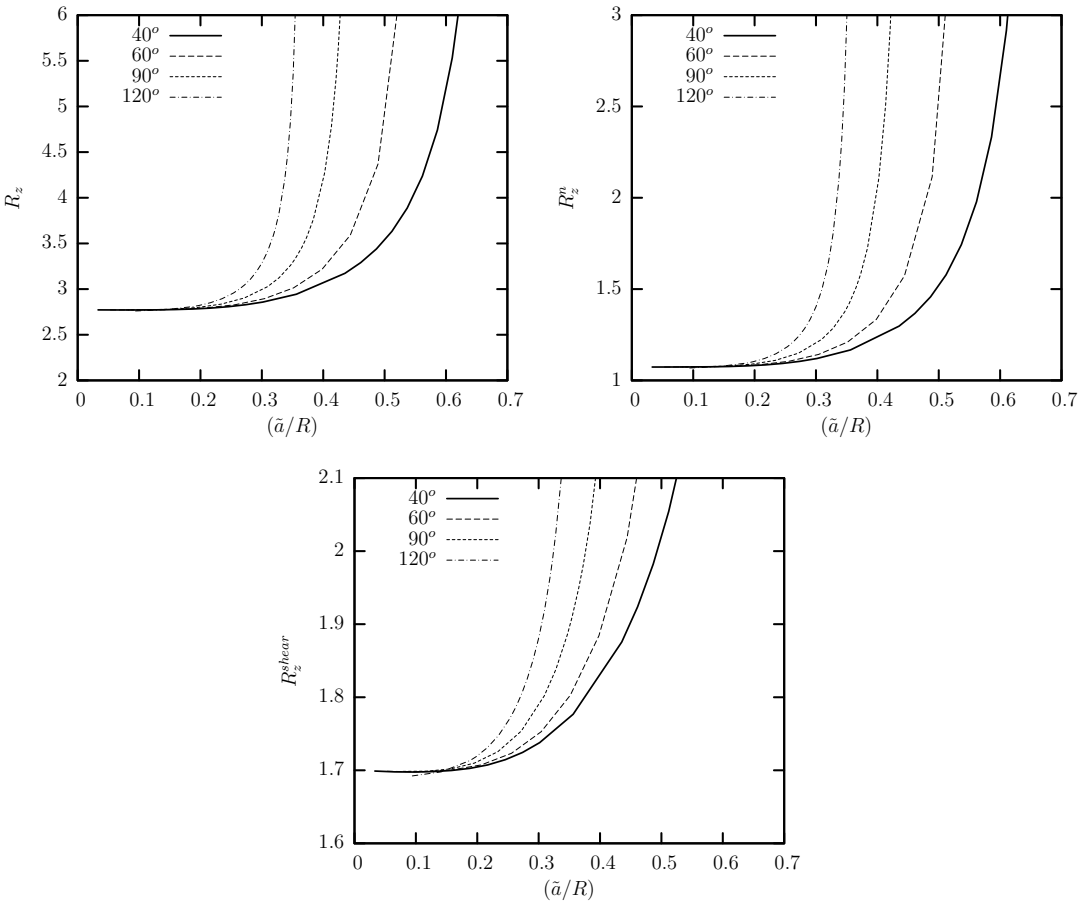

Figure 6.7: Resistance function for the sphere in z-direction as a function of the cell size $\tilde{a}/R$. The spreading angles is $\theta_0 = 40^o, 60^o, 90^o$ and 120^o. Resistance function for the (a) Total force R_x, (b) Normal force R_x^n, and (c) Shear force R_x^{shear}.

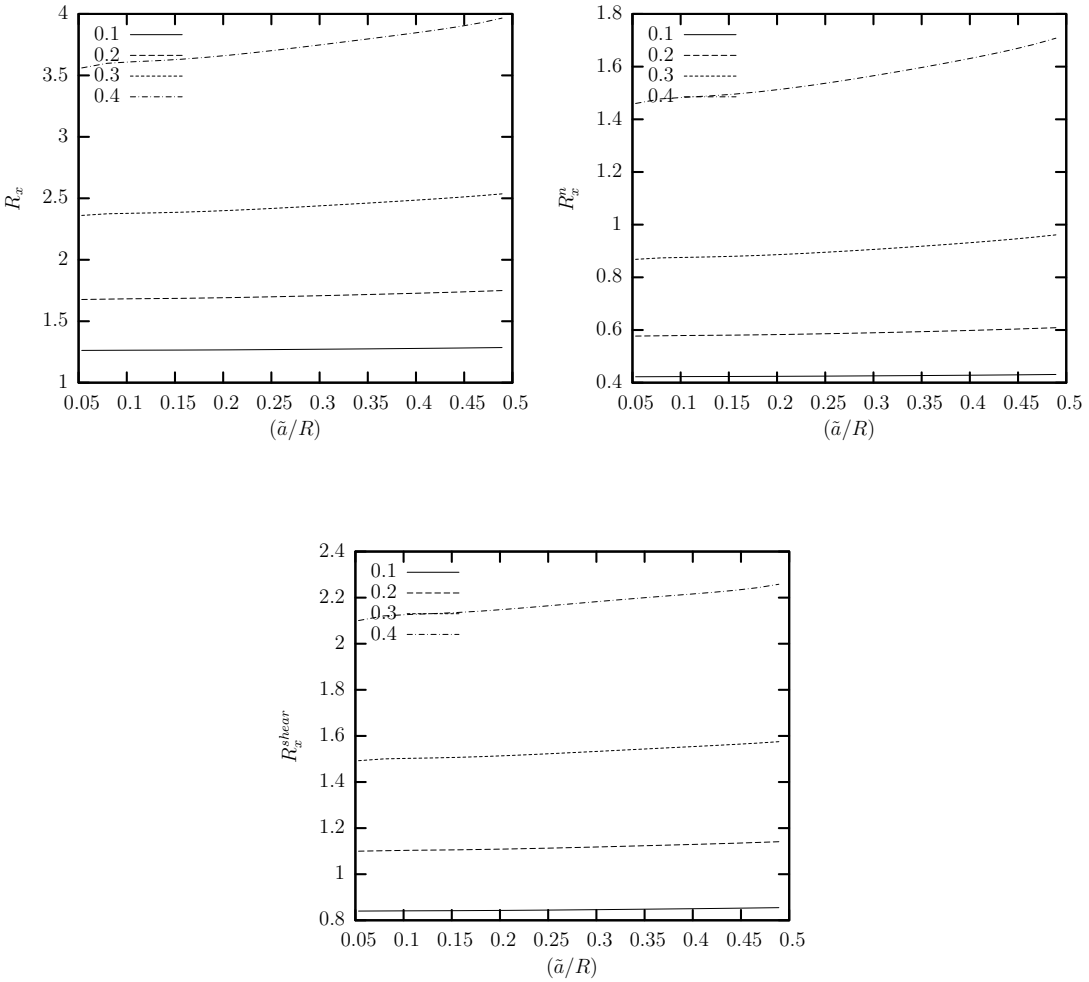

Figure 6.8: Resistance function for the sphere in x-direction as a function of the cell size $\tilde{a}/R$. The spreading angles is $\theta_0 = 60^o$. The size of the sphere is $R_s = 0.0$, 0.1, 0.2. 0.3 and 0.4. Resistance function for the (a) Total force R_x, (b) Normal force R_x^n, and (c) Shear force R_x^{shear}.

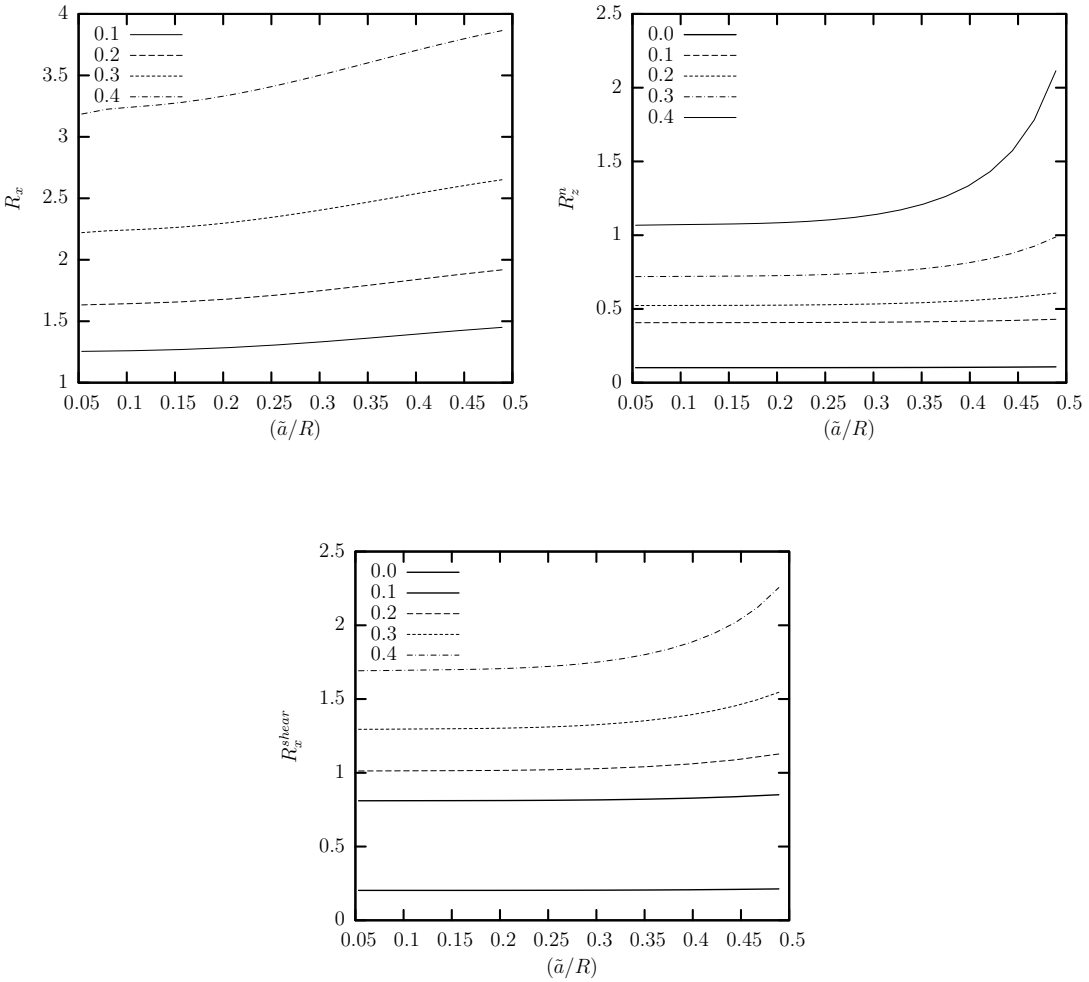

Figure 6.9: Resistance function for the sphere in z-direction as a function of the cell size $\tilde{a}/R$. The spreading angles is $\theta_0 = 60^o$. The size of the sphere is $R_s = 0.0$, 0.1, 0.2. 0.3 and 0.4. Resistance function for the (a) Total force R_x, (b) Normal force R_x^n, and (c) Shear force R_x^{shear}.

Chapter 7

Conclusions

In this thesis, we have investigated the motion and deformation of elastic capsules in microfluidics channels by extending the Membrane Spectral Boundary Element method developed by Dodson and Dimitrakopoulos [16] for free-suspended flows.

For a capsule moving along the centerline of a cylindrical channel, our computational model successfully and accurately reproduced the parachute shape observed in earlier experimental and computational studies.

For large capsules in a square channel, our investigation reveals that the steady-state capsule shape is non-axisymmetric. The capsule assumes a shape similar to the channel's cross-section, i.e. a square shape with rounded edges. Buckling of the capsule's upstream end resulting in a negative edge curvature is observed at higher capillary numbers and for large capsule sizes. For the largest capsules studied, we also observe the development of dimples at the capsule's lateral surface. A comparative study of capsule motion and deformation in cylindrical and square channels shows that the capsule deformation in a cylindrical channel is similar to that in a square channel at a larger capillary number. Our investigations have revealed that the capsule assumes a parachute shape at moderate flow rates.

In a rectangular channel, we observed a three-dimensional (i.e. non-axisymmetric) deformation of the capsule. For large capsules at high flow rates, a three-dimensional dimple formation at the upstream end was observed at steady state. The dimple formation results in a negative edge curvature.

We also investigated the evolution of capsule properties as the capsule moves along a converging channel. In the converging region, a fluctuation in the geometric and physical properties of the capsule was observed. We also noticed that with increasing capillary number the capsule deformation in the converging region increases but the capsule velocity and excess pressure drop remains unaffected. Effects of the fluids' viscosity ratio was observed only at very high viscosity ratios.

In addition, we have also investigated the hemodynamic forces on endothelial cells and leukocytes in blood capillaries. Our study on hemodynamic forces demonstrates that the forces on endothelial cells increase in the presence of leukocytes in close vicinity. Both normal and shear forces show considerable increase. We have also investigated the forces on moving leukocytes in the presence of adherent leukocytes. With increasing cell size, the magnitude of the force increases till a threshold value of the cell size and then decreases.

Bibliography

[1] M. Abkarian, M. Faivre and H. A. Stone, High-speed microfluidic differential manometer for cellular scale hydrodynamics. *Proc. Natl. Acad. Sci.* **103**, 147–159 (2006).

[2] M. Abkarian, M. Faivre, R. Horton, K. Smistrup, C. A. Best-Popescu and H. A. Stone, Cellular-scale hydrodynamics. *Biomed. Mater.* **3**, 034011(1-13) (2006).

[3] M. Antia, T. Herricks and P.K. Rathod, Microfluidic modeling of cell-cell interactions in malaria pathogenesis. *PLoS Pathog* **3**, 0939–0948 (2007).

[4] P. Bagchi, Mesoscale simulation of blood flow in small vessels. *Biophys. J.* **92**, 966–986 (2007).

[5] J. O. Barber, J. P. Alberding, J. M. Restrepo and T. W. Secomb, Simulated two dimensional red blood cell motion, deformation and partitioning in microvessel bifurcations. *Annals of Biomed. Eng.* **36**, 1690–1698 (2008).

[6] M. Carin, D. Barthès-Biesel, F. Edwards-Lévy, C. Postel, and D. C. Andrei, Compression of biocompatible liquid-filled HSA-alginate capsules: determination of the membrane mechanical properties. *Biotech. Bioeng.* **82**, 207–212 (2003).

[7] M. Chabert and J. Vlovy, Microfluidic high-throughput encapsulation and hydrodynamic self sorting of single cells. *Proc. Natl. Acad. Sci.* **105**, 3191–3196 (2008).

[8] B. Chung, P. C. Johnson and A. S. Popel, Application of Chimera grid to modeling cell motion and aggregation in a narrow tube. *Int. J. of Numerical Meth. in Fluids* **53** , 105–128 (2007).

[9] A. L. Cordeiro, M. Coelho, G. B. Sukhorukov, F. Dubreuil and H. Mohwald, Effect of shear stress on adhering polyelectrolyte capsules. *J. Colloid Interface Sci.* **280**, 68–75 (2004).

[10] H. A. Cranston, C. W. Boylan, G. L. Carroll, S. P. Sutera, J. R. Williamson, I. Y. Gluzman and D. J. Krogstad, Plasmodium falciparum maturation abolishes physiologic red cell deformability. *Science* **223**, 400–403 (1984).

[11] D. Dendukuri, T. A. Hatton and P. S. Doyle Synthesis and self-assembly of amphiphilic polymeric microparticles. *Langmuir* **23**, 4669–4674 (2007).

[12] P. Dimitrakopoulos, Interfacial dynamics in Stokes flow via a three-dimensional fully-implicit interfacial spectral boundary element algorithm. *J. Comput. Phys.*, **225**, 408–426 (2007).

[13] S. K. Doddi and P. Bagchi, Lateral migration of a capsule in a plane Poiseuille flow in a channel. *Int. J. Multiphase Flow* **34**, 966–986 (2008).

[14] S. K. Doddi and P. Bagchi, Three-dimensional computational modeling of multiple deformable cells flowing in microvessels. *Phys. Rev. E* **79**, 046318 (2009).

[15] W. R. Dodson III and P. Dimitrakopoulos, Spindles, cusps and bifurcations for capsules in stokes flow. *Phy. Rev. Lett.* **101**, 208102(1-4) (2008).

[16] W. R. Dodson III and P. Dimitrakopoulos, Dynamics of strain-hardening and strain-softening capsules in strong planar extensional flows via an interfacial spectral boundary element algorithm for elastic membranes. *J. Fluid Mech.*, **641**, 263–296 (2009).

[17] W. R. Dodson III and P. Dimitrakopoulos, Tank-treading of erythrocytes in strong shear flows via a non-stiff cytoskeleton-based continuum computational modeling. *Biophys. J.*, **to appear** (2010).

[18] M. Faivre, M. Abkarian, K. Bickraj and H. A. Stone, Geometrical focusing of cells in a microfluidic device: An approach to separate blood plasma. *Biorheology* **43**, 147–159 (2006).

[19] A. Fery and R. Weinkamer, Mechanical properties of micro- and nanocapsules: Single-capsule measurements. *Polymer* **48**, 7221–7235 (2007).

[20] L. K. Fiddes, E. W. K. Young, E. Kumacheva and A. R. Wheeler, Flow of microgel capsules through topographically patterned microchannels. *Lab on a chip* **7**, 863–867 (2007).

[21] J. B. Freund, Leukocyte margination in model microvessel. *Phys. Fluids* **19**, 023301(1-13) (2007).

[22] A. J. Griggs, A. Z. Zinchenko, and R. H. Davis, Low-Reynolds number motion of a deformable drop between two parallel plane walls. *Intl. J. Multiphase Flow* **33**, 182–206 (2007).

[23] S. R. Hodges, O. E. Jensen and J. M. Rallison, The motion of a viscous drop through a cylindrical tube. *J. Fluid Mech.* **501**, 279–301 (2004).

[24] M. Husmann, H. Rehage, E. Dhenin, and D. Barthès-Biesel, Deformation and bursting of nonspherical polysiloxane microcapsules in a spinning-drop apparatus. *J. Colloid Interface Sci.* **282**, 109–119 (2005).

[25] D. K. Hwang, D. Dendukuri and P. S. Doyle, Microfluidic-based synthesis of non-spherical magnetic hydrogel microparticles. *Lab Chip* **8**, 1640–1647 (2008).

[26] T. Hyakutake, T. Matsumoto and S. Yanase, Lattice Boltzmann simulation of blood cell behavior at microvascular bifurcations. *Mathematics and Computers in Simulation* **72**, 134–140 (2006).

[27] N. Korin, A. Bransky, and U. Dinnar, Theoretical model and experimental study of red blood cell (RBC) deformation in microchannels. *J. Biomech.* **40**, 2088–2095 (2007).

[28] E. Lac, D. Barthès-Biesel, N. A. Pelekasis, and J. Tsamopoulos, Spherical capsules in three-dimensional unbounded Stokes flows: effect of the membrane constitutive law and onset of buckling. *J. Fluid Mech.* **516**, 303–334 (2004).

[29] E. Lac and D. Barthès-Biesel, Deformation of a capsule in simple shear flow: Effect of membrane prestress. *Phys. Fluid* **17**, 072105 (2005).

[30] E. Lac and D. Barthès-Biesel, Pairwise interaction of capsules in simple shear flow: Three-dimensional effects. *Phys. Fluid* **20**, 040801 (2008).

[31] E. Lac and J. D. Sherwood , Motion of a drop along the centerline of a capillary in a pressure-driven flow. *J. Fluid Mech.* **640**, 27–54 (2009).

[32] D. V. Le, J. White, J. Peraire, K. M. Lim and B. C. Khoo, An implicit immersed boundary method for three-dimensional fluid-membrane interactions. *J. Comput. Phys.* **228**, 8427–8445 (2009).

[33] Y. Lefebvre and D. Barthès-Biesel, Motion of a capsule in a cylindrical tube: effect of membrane pre-stress. *J. Fluid Mech.* **589**, 157–181 (2007).

[34] Y. Lefebvre, E. Leclerc, D. Barthès-Biesel, J. Walter and F. Edwards-Lévy , Flow of artificial microcapsules in microfluidic channels: A method for determining the elastic properties of the membrane. *Phys. Fluids* **20**, 123102 (2008).

[35] D. Lensen, K. V. Breukelen, D. M. Vriezema and J. C. M. V. Hest Preparation of biodegradable liquid core PLLA microcapsules and hollow PLLA microcapsules using microfluidics. *Macromol. Bioscience* **10**, 475–480 (2010)

[36] A. Leyrat-Maurin, A. Drochon and D. Barthès-Biesel, Flow of a capsule through a constriction:application to cell filtration. *J. Phys. III France* **3**, 1051–1056 (1993).

[37] A. Leyrat-Maurin and D. Barthès-Biesel, Motion of a deformable capsule through a hyperbolic constriction. *J. Fluid Mech.* **279**, 135–163 (1994).

[38] G. Ma, J. Hua and H. Li, Numerical modeling of the behavior of an elastic capsule in a microchannel flow: The initial motion. *Phys. Rev. E* **79**, 046710 (2009).

[39] M. J. Martinez and K. S. Udell, Axisymmetric creeping motion of drops through circular tubes. *J. Fluid Mech.* **210**, 565–591 (1990).

[40] N. Mohandas and J. A. Chasis, Red blood cell deformability, membrane material properties and shape: regulation by transmembrane, skeletal and cytosolic proteins and lipids. *Sem. Hem.* **30**, 171–192 (1993).

[41] H. Noguchi and G. Gompper, Shape transitions of fluid vesicles and red blood cells in capillary flows. *Proc. Natl. Acad. Sci. USA* **40**, 14159–14164 (2005).

[42] G. Pieper, H. Rehage, and D. Barthès-Biesel, Deformation of a capsule in a spinning drop apparatus. *J. Colloid Interface Sci.* **202**, 293–300 (1998).

[43] I. V. Pivkin and G. E. Karniadakis, Accurate coarse-grained modeling of red blood cells. *Phys. Rev. Letters* **101**, 118105 (2008).

[44] C. Pozrikidis, Finite deformation of liquid capsules enclosed by elastic membranes in simple shear flow. *J. Fluid Mech.* **297**, 123–152 (1995).

[45] C. Pozrikidis (ed.), *Modeling and Simulation of Capsules and Biological Cells.* Chapman and Hall, London (2003).

[46] C. Pozrikidis, Axisymmetric motion of file of red blood cells through capillaries. *Phys. Fluids* **17**, 031503(1-14) (2005).

[47] C. Pozrikidis, Numerical simulation of cell motion in tube flow. *Annals of Biomedical Engineering* **33**, 165–178 (2005).

[48] M. Prevot, A. L. Cordeiro, G. B. Sukhorukov, Y. Lvov, R. S. Besser, and H. Mohwald, Design of a microfluidic system to investigate the mechanical properties of layer by layer fabricated capsules. *Macromol. Mater. Eng.* **288**, 915–919 (2003).

[49] C. Queginer and D. Barthès-Biesel, Axisymmetric motion of capsules through cylindrical channels. *J. Fluid Mech.* **348**, 349-376 (1997).

[50] S. Ramanujan and C. Pozrikidis, Deformation of liquid capsules enclosed by elastic membranes in simple shear flow: large deformations and the effect of fluid viscosities. *J. Fluid Mech.* **361**, 117–143 (1998).

[51] F. Risso, F. Collè-Pailot, and M. Zagzoule, Experimental investigation of a bioartificial capsule flowing in a narrow tube. *J. Fluid Mech.* **547**, 149–173 (2006).

[52] T. W. Secomb, R. Hsu, and A.R. Pries, A model for red blood cell motion in glycocalyx-lined capillaries. *Am. J. Physiol. Heart Circ. Physiol.* **274**, H1016–H1022 (1998).

[53] T. W. Secomb, B. Styp-Rekowska and A. R. Pries, Two-dimensional simulation of red blood cell deformation and lateral migration in microvessels. *Annals of Biomed. Eng.* **35**, 755–765 (2007).

[54] J. P. Shelby, J. White, K. Ganesan, P. K. Rathod, and D. T. Chiu, A microfluidic model for single-cell capillary obstruction by Plasmodium falciparum infected erythrocytes. *Proc. Natl. Acad. Sci. USA* **100** 14618–14622 (2003).

[55] S. Seiffert, J. Thiele, A. R. Abate and D. A. Weitz, Smart microgel capsules from macromolecular precursors. *J. Am. Chem. Soc.* **132**, 6606–6609 (2010).

[56] R. Skalak and P-I. Branemark, Deformation of red blood cells in capillaries. *Science* **164**, 717–719 (1969).

[57] C. Sun, C. Migliorini and L. L. Munn, Red blood cells initiate leukocyte rolling in postcapillary expansions: A Lattice Boltzmann Analysis. *Biophys. J.* **85**, 208–222 (2003).

[58] C. Sun and L. L. Munn, Particulate nature of blood determines macroscopic rheology: A 2-D Lattice Boltzmann Analysis. *Biophys. J.* **88**, 1635–1645 (2005).

[59] S. Teh, R. Lin, L. Hung and A. P. Lee, Droplet microfluidics. *Lab on a chip* **8**, 198–220 (2008).

[60] J. D. Tice, H. Song, A. D. Lyon, and R. F. Ismagilov Formation of droplets and mixing in multiphase microfluidics at low values of the Reynolds and the capillary numbers. *Langmuir* **19**, 9127–9133 (2003).

[61] S. A. Vanapalli, A. G. Banpurkar, D. V. D. Ende, M. H. Duits and F. Mugelev Hydrodynamic resistance of single confined moving drops in rectangular microchannels. *Lab on a Chip* **9**, 982–990 (2009).

[62] Y. Wang and P. Dimitrakopoulos, A three-dimensional spectral boundary element algorithm for interfacial dynamics in Stokes flow. *Phys. Fluids* **18**, 082106(1-16) (2006).

[63] Y. Wang and P. Dimitrakopoulos, Normal force exerted on vascular endothelial cells. *Phys. Rev. Lett.*, **96**, 028106(1-4) (2006).

[64] Y. Wang and P. Dimitrakopoulos, Nature of the hemodynamic forces exerted on vascular endothelial cells or leukocytes adhering to the surface of blood vessels. *Phys. Fluids*, **18**, 087107(1-14) (2006).

[65] C. Yih, *Fluid Mechanics*. West River Press, Michigan (1979).

[66] H. Zhao, A. H. G. Isfahani, L. N. Olson, and J. B. Freund, A spectral boundary integral method for flowing blood cells. *J. Comp. Phys.* **229**, 3726–3744 (2010).

[67] G. Zhu, A. Alexeev, E. Kumacheva, and A. C. Balazs, Modeling the interactions between compliant microcapsules and pillars in microchannels. *J. Chem. Phys.* **127**, 915–919 (2007).

[68] G. Zhu, A. Alexeev, and A. C. Balazs, Designing constricted microchannels to selectively entrap soft particles. *Macromolecules* **40**, 5176–5181 (2007).

[69] J. Zhang, P. C. Johnson and A. S. Popel, An immersed boundary lattice Boltzmann approach to simulate deformable liquid capsules and its application to microscopic blood flows. *Phys. Biol.* **4**, 285–295 (2007).

[70] A. M. Artoli, A. Sequeira, A. S. Silva-Herdade and C. Saldanha, Leukocyte rolling and recruitment by endothelial cells: Hemorheological experiments and numerical simulations. *J. of Biomechanics* **40** 3493–3502 (2007).

[71] H. Brenner and J. Happel, Slow viscous flow past a sphere in a cylindrical tube. *J. Fluid Mech.* **4** 195–213 (1957).

[72] K. E. Caputo, D. Lee and M. R. King, Adhesive dynamics simulations of the shear threshold effect for leukocytes. *Biophysical J.* **92**, 787–797 (2007).

[73] G. B. Chapman and G. R. Cokelet, Flow resistance and drag forces due to multiple adherent leukocytes in postcapillary vessels. *Biophys. J.* **74**, 3292–3301 (1998).

[74] G. B. Chapman and G. R. Cokelet, Model studies of leukocyte-endothelium-blood interactions. II. Hemodynamic impact of leukocytes adherent to the wall of post-capillary vessels. *Biorheology* **34**, 37–56 (1997).

[75] G. B. Chapman and G. R. Cokelet, Model studies of leukocyte-endothelium-blood interactions. I. The fluid flow drag force on the adherent leukocyte. *Biorheology* **33**, 119-138 (1996).

[76] P. Dimitrakopoulos and J. J. L. Higdon, On the displacement of three-dimensional fluid droplets from solid surface in low-Reynolds-number shear flows. *J. Fluid Mech.* **377**, 189–222 (1998).

[77] J. A. Frangos, T. Y. Huang and C. B. Clark, Steady shear and step changes in shear stimulate endothelium via independent mechanisms - Superposition of transient and sustained nitric oxide production. *Biochem. Biophys. Res. Commun.* **224** 660–665 (1996).

[78] J.J.L. Higdon and G. P. Muldowney, Resistance functions for spherical particles, droplets and bubbles in cylindrical domain. *J. Fluid Mech.* **298** 193–210 (1995).

[79] M. B. Kim and I. H. Sarelius, Regulation of leukocyte recruitment by local wall shear rate and leukocyte delivery. *Microcirculation* **11** (2004).

[80] M. R. King, D. Bansal, M. B. Kim and I. H. sarelius, The effect of hematocrit and leukocyte adherence on flow direction in the microcirculation. *Annals of Biomed. Engg.* **32** (2004).

[81] G. P. Muldowney and J. J. L. Higdon, A spectral boundary element approach to three-dimensional Stokes flow. *J. Fluid Mech.* **298**, 167-192 (1995).

[82] A. S. Popel and P. C. Johnson, Microcirculation and hemorheology. *Ann. Rev. Fluid Mech.*, **37**, 43–69 (2005).

[83] C. Pozrikidis, *Boundary Integral and Singularity Methods for Linearized Viscous Flow.* Cambridge University Press, Cambridge (1992).

[84] N. A. Quddus, W. A. Moussa and S. Bhattacharjee, Motion of a spherical particle in a cylindrical channel using arbitrary Lagrangian-Eulerian method *J. Coll. Interface Sci.* **317** 620–630 (2008).

[85] H. W. Sill, Y. S. Chang, J. R. Artman, J. A. Frangos, T. M. Hollis and J. M. Tarbell, Shear stress increases hydraulic conductivity of cultured endothelial monolayers. *Am. J. Physiol. Heart Circ. Physiol.* **268** H535–H543 (1995).

[86] M. Sugihara-Seki and R. Skalak, Force acting on spheres adhered to a vessel wall. *Biorheology* **34**, 249–260 (1997).

[87] M. Sugihara-Seki, Flow around cells adhered to a microvessel wall. I. Fluid stresses and forces acting on the cells. *Biorheology* **37**, 341-359 (2000).

[88] M. Sugihara-Seki and G. W. Schmid-Schönbein, The fluid shear stress distribution on the membrane of leukocytes in the microcirculation. *J. Biomech. Eng.* **125**, 628–638 (2003).

[89] O. Traub and B. C. Berk, Laminar shear stress: Mechanism by which endothelial cells transduce an athreoprotective force. *Arterioscler. Thromb. Vasc. Biol.* **18** (1998).

Vita

Shugi Kuriakose was born in August 1979, in Kerala, India. She attended Kendriya Vidyalaya INA Colony from May 1993 to April 1997. After graduating from High School, she enrolled at the Kerala University in the TKM College of Engineering. In May of 2001, she graduated and received a Bachelor of Technology degree in Chemical Engineering. Her undergraduate thesis was titled "Thermo-chemical model development for the curing process of phenolic resin based composites". Following graduation, she enrolled for graduate studies at Indian Institute of Technology, Delhi. She conducted research in the field of adsorbent development for arsenic removal. In December 2002, she received a Masters of Technology degree in Process Engineering and Design. Afterwards, she worked as Research Scientist at Indian Space Research Organization. In June 2003, she began working as research engineer at the Indian Oil Corporation. Her duties there included process development for hydro-treating operation for oil refining. She departed IOC in June 2004. Shugi enrolled in the Chemical Engineering Graduate Program at the University of Maryland, College Park, in September 2006. Under the guidance of Professor Panagiotis Dimitrakopoulos, she has conducted research regarding the flow dynamics of capsules in microchannels. She is defending her dissertation for the Doctor of Philosophy degree in November 2010.